Materials for nanostructured organic devices : theoretical and experimental studies of donors and acceptors

Lucas de Lima Citolino

INTERNATIONAL JOINT SUPERVISION OF THESIS

SÃO PAULO STATE UNIVERSITY (UNESP)

Graduate Program in Science and Technology of Materials (POSMAT)

and

UNIVERSITÉ DE PAU ET DES PAYS DE L'ADOUR

Ecole Doctorale Sciences Exactes et leurs Applications

LUCAS VINICIUS DE LIMA CITOLINO

MATERIALS FOR NANOSTRUCTURED ORGANIC DEVICES: THEORETICAL AND EXPERIMENTAL STUDIES OF DONORS AND ACCEPTORS

BRAZILIAN SUPERVISOR: PROF. DR. CLARISSA DE ALMEIDA OLIVATI
FRENCH SUPERVISOR: PROF. DR. DIDIER BÉGUÉ
FRENCH CO-SUPERVISOR: DR. ROGER CLIVE HIORNS

PRESIDENTE PRUDENTE
2022

SUPERVISION CONJOINTE INTERNATIONALE DE LA THESE

UNIVERSIDADE ESTADUAL PAULISTA (UNESP)

Programa de Pós-graduação em Ciência e Tecnologia de Materiais

et

UNIVERSITÉ DE PAU ET DES PAYS DE L'ADOUR (UPPA)

École Doctorale des Sciences Exactes et leurs Applications

LUCAS VINICIUS DE LIMA CITOLINO

MATÉRIAUX POUR DISPOSITIFS ORGANIQUES NANOSTRUCTURÉS : ÉTUDES THÉORIQUES ET EXPÉRIMENTALES DES DONNEURS ET DES ACCEPTEURS

DIRECTEUR BRÉSILIEN: PROF. DR. CLARISSA DE ALMEIDA OLIVATI
DIRECTEUR FRANÇAIS: PROF. DR. DIDIER BÉGUÉ
DIRECTEUR FRANÇAIS: DR. ROGER CLIVE HIORNS

PRESIDENTE PRUDENTE
2022

SUPERVISÃO CONJUNTA INTERNACIONAL DE TESE

UNIVERSIDADE ESTADUAL PAULISTA (UNESP)

Programa de Pós-graduação em Ciência e Tecnologia de Materiais

e

UNIVERSITÉ DE PAU ET DES PAYS DE L'ADOUR (UPPA)

École Doctorale des Sciences Exactes et leurs Applications

LUCAS VINICIUS DE LIMA CITOLINO

MATERIAIS PARA DISPOSITIVOS ORGÂNICOS NANOESTRUTURADOS: ESTUDOS TEÓRICOS E EXPERIMENTAIS DE DOADORES E ACEITADORES

ORIENTADOR NO BRASIL: PROFA. DRA. CLARISSA DE ALMEIDA OLIVATI
ORIENTADOR NA FRANÇA: PROF. DR. DIDIER BÉGUÉ
COORIENTADOR NA FRANÇA: DR. ROGER CLIVE HIORNS

PRESIDENTE PRUDENTE
2022

LUCAS VINICIUS DE LIMA CITOLINO

MATERIALS FOR NANOSTRUCTURED ORGANIC DEVICES: THEORETICAL AND EXPERIMENTAL STUDIES OF DONORS AND ACCEPTORS

A thesis submitted as part of the requirements for the degree of Doctorate of Philosophy at the São Paulo State University (UNESP) – Graduate Program in Science and Technology of Materials – in Science and Technology of Materials and Université de Pau et des Pays de l'Adour (UPPA) – Ecole Doctorale Sciences Exactes et leurs Applications (ED SEA) – in Polymer Chemistry.

Brazilian supervisor: Prof. Dr. Clarissa de Almeida Olivati

French supervisor: Prof. Dr. Didier Bégué

PRESIDENTE PRUDENTE
2022

THÈSE

UNIVERSITE DE PAU ET DES PAYS DE L'ADOUR

École Doctorale Sciences Exactes et leurs Applications

Présentée et soutenue le (date)

par **Lucas Vinicius DE LIMA CITOLINO**

pour obtenir le grade de docteur
de l'Université de Pau et des Pays de l'Adour
Spécialité : Doctorat en Chimie des Polymères

MATÉRIAUX POUR DISPOSITIFS ORGANIQUES NANOSTRUCTURÉS : ÉTUDES THÉORIQUES ET EXPÉRIMENTALES DES DONNEURS ET DES ACCEPTEURS

MEMBRES DU JURY

RAPPORTEURS

• Kathleen Isabelle MOINEAU-CHANE CHING	Directrice de Recherche / Laboratoire de Chimie de Coordination
• Marystela FERREIRA	Professeur / Universidade Federal de São Carlos

EXAMINATEURS

• Christine LARTIGAU-DAGRON	Maître de Conférences - HDR / Université de Pau et des Pays de l'Adour
• Augusto BATAGIN NETO	Professeur / Universidade Estadual Paulista

DIRECTEURS

• Didier BEGUE	Professeur / Université de Pau et des Pays de l'Adour
• Clarissa DE ALMEIDA OLIVATI	Professeur / Universidade Estadual Paulista

ECOLE DOCTORALE :
Sciences Exactes et leurs Applications

LABORATOIRE :
Equipe de Physique et Chimie des Polymères

LUCAS VINICIUS DE LIMA CITOLINO

Citolino, Lucas Vinicius de Lima.

Materials for nanostructured organic devices: theoretical and experimental studies of donors and acceptors / Lucas Vinicius de Lima Citolino, 2022

132 pp. : il.

Supervisor: Clarissa de Almeida Olivati

Thesis (Doctorate degree) – São Paulo State University. School of Sciences, Bauru, 2022

1. DFT. 2. Electron donors. 3. Electron acceptors. 4. Polyfullerenes. I. Universidade Estadual Paulista. Faculdade de Ciências. II. Title.

UNIVERSIDADE ESTADUAL PAULISTA

Câmpus de Bauru

ATA DA DEFESA PÚBLICA DA TESE DE DOUTORADO DE LUCAS VINICIUS DE LIMA CITOLINO, DISCENTE DO PROGRAMA DE PÓS-GRADUAÇÃO EM CIÊNCIA E TECNOLOGIA DE MATERIAIS, DA FACULDADE DE CIÊNCIAS - CÂMPUS DE BAURU.

Aos 07 dias do mês de dezembro do ano de 2022, às 09:00 horas, por meio de Videoconferência, realizou-se a defesa de TESE DE DOUTORADO de LUCAS VINICIUS DE LIMA CITOLINO, intitulada **FABRICAÇÃO E CARACTERIZAÇÃO DE DISPOSITIVOS ORGÂNICOS UTILIZANDO FILMES NANOESTRUTURADOS DE POLÍMEROS CONJUGADOS E FULERENOS**. A Comissão Examinadora foi constituida pelos seguintes membros: Profa. Dra. CLARISSA DE ALMEIDA OLIVATI (Orientador(a) - Participação Presencial) do(a) Departamento de Fisica / UNESP Campus de Presidente Prudente, Prof. Dr. DIDIER BEGUE (Participação Virtual) do(a) Institut des Sciences Analytiques et de Physico-Chimie pour l'Environnement et les Matériaux (Institut IPREM) / Université de Pau et des Pays de l'Adour – Collège STEE/UPPA/França, Profa. Dra. CHRISTINE LARTIGAU-DAGRON (Participação Virtual) do(a) Institut des Sciences Analytiques et de Physico-Chimie pour l'Environnement et les Matériaux (Institut - IPREM) / Université de Pau et des Pays de l'Adour – UPPA/França, Dra. KATHLEEN ISABELLE MOINEAU-CHANE CHING (Participação Virtual) do(a) Laboratoire de Chimie de Coordination, LCC UPR CNRS 8241, Prof. Dr. AUGUSTO BATAGIN NETO (Participação Presencial) do(a) Coordenadoria de Curso de Engenharia de Producao / Instituto de Ciencias e Engenharia de Itapeva Unesp, Profª. Drª. MARYSTELA FERREIRA (Participação Presencial) do(a) Departamento de Físico-Química / Universidade Federal de São Carlos (UFSCar) - Sorocaba. Após a exposição pelo doutorando e arguição pelos membros da Comissão Examinadora que participaram do ato, de forma presencial e/ou virtual, o discente recebeu o conceito final Aprovado. Nada mais havendo, foi lavrada a presente ata, que após lida e aprovada, foi assinada pelo(a) Presidente(a) da Comissão Examinadora.

Profa. Dra. CLARISSA DE ALMEIDA OLIVATI

Prof. Dr. DIDIER BEGUE

UNIVERSIDADE ESTADUAL PAULISTA

Câmpus de Bauru

Profa. Dra. CHRISTINE LARTIGAU-DAGRON
Dra. KATHLEEN ISABELLE MOINEAU-CHANE CHING

Prof. Dr. AUGUSTO BATAGIN NETO

Profª. Drª. MARYSTELA FERREIRA

Prof. Dr. EDSON LAURETO

Dr. ROGER CLIVE HIORNS

Prof. Dr. DEUBER LINCON DA SILVA AGOSTINI

A banca aprovou a mudança do título para:

"Materials for nanostructured organic devices: Theoretical and Experimental studies of donors and acceptors"

In memory of my father, José Luis Citolino,
with love and gratefulness.
I'm sure, he would be very proud.

"We're just two lost souls
Swimming in a fish bowl year after year
Running over the same old ground
What have we found?
The same old fears
Wish you were here."
(Pink Floyd – Wish You Were Here)

ACKNOWLEDGMENTS

My family, my parents José and Evanilda, my siblings João and Ana, and my nephew Rafael, for everything. If I gotten so far it was because of your support and love;

Clarissa, for her friendship, guidance, trust and patience in carrying out this work, besides all the learning since undergraduate scientific project. Thank you for always believing that things would work out;

Mariana and Mafalda, for being so special in my life and for all love and learning;

All my friends, especially Maykel and Gabriel for their friendship, for sharing our achievements and frustrations, and especially for the funny moments;

My friends Lucas and Marina, for all academic support, in life, in the universe and everything else;

My research group LOFF – UNESP, and especially Maria Luisa, Edilene, Vinicius and Jéssyka, my friends inside and outside of the lab making the daily life so pleasant;/

Prof. Dr. Casé, for your friendship, guidance and being an inspiration from the early days of graduation. It's been seeing you over all these years that I'm sure of the career I chose.

Prof. Dr. Neri Alves, Prof. Dr. Aldo Job and Prof. Dr. Carlos Tello, your help and support were fundamental to keep me in the doctorate.

Prof. Dr. Didier Begue and Dr. Roger Hiorns for all help and support in Pau, as well as guiding me in the DFT calculations and for always being optimistic about hard tasks. *Merci!*

Prof. Dr. Christine Lartigau-Dagron, Dr. Kathleen Moineau-Chane Ching, Prof. Dr. Marystela Ferreira, Prof. Dr. Augusto Batagin Neto and Prof. Dr. Henrique de Santana for the valuable advices and corrections in the qualification and defense exam;

All the Brazilian friends that I made when I was in France, who made me feel closer to my home.

The funding agencies CAPES, CNPq, FAPESP and INEO for all the financial support, which was of fundamental importance for the accomplishment of this work;

All those who, directly or indirectly contributed to the development of this PhD research.

“Education isn’t something you can finish.”

Isaac Asimov

“I may not have gone where I intended to go,
but I think I have ended up where I needed to be.”

Douglas Adams

CITOLINO, L. V. L. **Materials for nanostructured organic devices: theoretical and experimental studies of donors and acceptors**. 2022. 132 pp. Thesis (PhD in Science and Technology of Materials) - UNESP and (PhD in Polymer Chemistry) - UPPA, Bauru, 2022.

ABSTRACT

The frontier energy levels of conjugated polymers are critical to their performance in organic electronic devices. In organic solar cells the magnitude of the HOMO and LUMO levels directly affects parameters, such as the short circuit current and the open-circuit voltage, which are very important to achieve high efficiency. Accordingly, density functional theory (DFT) has become useful to model orbital energies of conjugated organic molecules. But, performing DFT calculations on conjugated polymers is challenging due to their size (large number of atoms), besides the problems to predict accurate values for virtual orbitals. In this context, the main aim of this work is set out the general considerations for the use of DFT approaches in organic molecules with large number of atoms, in particular when one has to describe one or more electronic states of more or less strongly correlated electrons. Thereby, a series of DFT calculations were performed, using different basis set and functionals, in singlet and triplet states on a set of promising donor-acceptor pairs to estimate accurate values on molecular orbital energies. In addition, DFT calculations was used to optimise the molecular geometries and determine energies of unpublished polyfullerenes to compare with Langmuir-Schaefer thin films properties. To obtain experimentally the HOMO and LUMO from polyfullerenes thin films, measurements of absorption were performed using Ultraviolet-visible spectroscopy and electrical characterizations were carried out through cyclic voltammetry measurements. In a series of DFT calculations in singlet state, with different functionals and basis set, the B3LYP functional together with 6-311G(d,p) basis set give the best values for HOMO and LUMO. For saving computational resources, 6-31G(d) can be used to provide good values for energy levels from frontier molecular orbitals. For donors, the correlation between the LUMO calculated with experimental results is too poor, while for acceptors, is acceptable. The DFT calculations in triplet states give good correlation for donors, where the LUMO energy is most accurately approximated from the αHOMO energy. In the study of polyfullerene thin films, the π-A isotherms indicated that depending on the solvent, the arrangement of molecules is altered, indicating higher solubility and lower level of aggregation, and vice versa. In UV-Vis and CV measurements the influence of solvent is also evidenced being directly related to the maximum absorption and difference in the position of the absorption peak, and also to shifting of oxidation and reduction peaks. In the junction between DFT calculations and CV and UV-Vis measurements, the DFT/B3LYP/6-31+G(d) method provide LUMO values close to experimental values, thus being an important tool for comparing results, since there is no previous literature from these exact polyfullerenes.

Keywords: DFT, HOMO, LUMO, B3LYP, electron donor, electron acceptor, polyfullerenes.

CITOLINO, L. V. L. **Matériaux pour dispositifs organiques nanostructurés : études théoriques et expérimentales des donneurs et des accepteurs**. 2022. 132 p. Thèse (Docteur en Science et Technologie de Matériaux) - UNESP et (Docteur en Chimie des Polymères) - UPPA, Bauru, 2022.

RÉSUMÉ

Les niveaux d'énergie frontière des polymères conjugués sont essentiels à leur performance dans les dispositifs électroniques organiques. Dans les cellules solaires organiques, l'amplitude des niveaux HOMO et LUMO affecte directement des paramètres, tels que le courant de court-circuit et la tension en circuit ouvert, qui sont très importants pour obtenir un rendement élevé. En conséquence, la théorie de la fonctionnelle de la densité (DFT) est devenue utile pour modéliser les énergies orbitales des molécules organiques conjuguées. Mais, effectuer des calculs DFT sur des polymères conjugués est difficile en raison de leur taille (grand nombre d'atomes), en plus des problèmes de prédiction de valeurs précises pour les orbitales virtuelles. Dans ce contexte, l'objectif principal de ce travail est d'exposer les considérations générales pour l'utilisation des approches DFT dans les molécules organiques à grand nombre d'atomes, en particulier lorsqu'il s'agit de décrire un ou plusieurs états électroniques d'électrons plus ou moins fortement corrélés. Ainsi, une série de calculs DFT ont été effectués, en utilisant différents ensembles de bases et fonctionnelles, dans des états singulet et triplet sur un ensemble de paires donneur-accepteur prometteuses pour estimer des valeurs précises sur les énergies orbitales moléculaires. De plus, des calculs DFT ont été utilisés pour optimiser les géométries et déterminer les énergies de polyfullerènes non publiés à comparer avec les propriétés des couches minces de Langmuir-Schaefer. Pour obtenir expérimentalement l'HOMO et le LUMO à partir de couches minces de polyfullerènes, des mesures d'absorption ont été réalisées par spectroscopie ultraviolet-visible et des caractérisations électriques ont été réalisées par des mesures de voltampérométrie cyclique (VC). Dans une série de calculs DFT en état singulet, avec différentes fonctionnelles et ensemble de base, la fonctionnelle B3LYP associée à l'ensemble de base 6-311G(d,p) donne les meilleures valeurs pour HOMO et LUMO. Pour économiser les ressources de calcul, 6-31G(d) peut être utilisé pour fournir de bonnes valeurs pour les niveaux d'énergie des orbitales moléculaires frontières. Pour les donneurs, la corrélation entre le LUMO calculé avec les résultats expérimentaux est trop faible, alors que pour les accepteurs, elle est acceptable. Les calculs DFT dans les états triplets donnent une bonne corrélation pour les donneurs, où l'énergie LUMO est la plus précisément approximée à partir de l'énergie αHOMO. Dans l'étude des films minces de polyfullerène, les isothermes π-A ont indiqué qu'en fonction du solvant, l'arrangement des molécules est modifié, indiquant une solubilité plus élevée et un niveau d'agrégation plus faible, et vice versa. Dans les mesures UV-Vis et VC, l'influence du solvant est également mise en évidence comme étant directement liée à l'absorption maximale et à la différence de position du pic d'absorption, ainsi qu'au déplacement des pics d'oxydation et de réduction. A la jonction entre les calculs DFT et les mesures UV-Vis et VC, la méthode DFT/B3LYP/6-31+G(d) fournit des valeurs LUMO proches des valeurs expérimentales, étant ainsi un outil important pour comparer les résultats, puisqu'il n'y a pas d'antécédents littérature à partir de ces polyfullerènes exacts.

Mots-clés: DFT, HOMO, LUMO, B3LYP, donneur d'électrons, accepteur d'électrons, polyfullerènes.

CITOLINO, L. V. L. **Materiais para dispositivos orgânicos nanoestruturados: estudos teóricos e experimentais de doadores e aceitadores**. 2022. 132 f. Tese (Doutor em Ciência e Tecnologia de Materiais) - UNESP e (Doutor em Química de Polímeros) - UPPA, Bauru, 2022.

RESUMO

Os níveis de energia de fronteira de polímeros conjugados são importantíssimos para seu desempenho em dispositivos eletrônicos orgânicos. Nas células solares orgânicas, a magnitude dos níveis HOMO e LUMO afeta diretamente parâmetros, como a corrente de curto-circuito e a tensão de circuito aberto, que são essenciais para alcançar alta eficiência. Assim, a teoria do funcional da densidade (DFT) tornou-se útil para modelar energias orbitais de moléculas orgânicas conjugadas. Porém, realizar cálculos DFT em polímeros conjugados é desafiador devido ao seu tamanho (grande número de átomos), além dos problemas para predizer valores precisos de orbitais virtuais. Neste contexto, o principal objetivo deste trabalho é expor as considerações gerais para o uso de abordagens DFT em moléculas orgânicas com grande número de átomos, em particular quando se tem que descrever um ou mais estados eletrônicos de elétrons mais ou menos fortemente correlacionados. Assim, uma série de cálculos de DFT foram realizados, usando diferentes funções de base e funcionais, em estados singleto e tripleto em um conjunto de pares doador-aceptor promissores para estimar valores precisos nas energias dos orbitais moleculares. Além disso, cálculos de DFT foram usados para otimizar geometrias e determinar energias de polifulerenos (materiais inéditos) para comparar com propriedades de filmes finos de Langmuir-Schaefer. Para obter experimentalmente os valores de HOMO e o LUMO a partir dos filmes finos, as medidas de absorção foram realizadas espectroscopia de absorção óptica UV-visível, e as medidas elétricas foram realizadas através da voltametria cíclica (VC). Em uma série de cálculos DFT no estado singleto, com diferentes funções de base e funcionais, o funcional B3LYP junto com a função de base 6-311G(d,p) fornecem os melhores valores para HOMO e LUMO. Para economizar recursos computacionais, a função de base 6-31G(d) pode ser usada para fornecer bons valores para os níveis de energia de orbitais moleculares de fronteira. Para os doadores, a correlação entre o LUMO calculado com os resultados experimentais é baixa, enquanto para os aceitadores, é aceitável. Os cálculos DFT em estados tripletos fornecem boa correlação para doadores, onde a energia LUMO é aproximada com mais precisão da energia do αHOMO. No estudo de filmes finos de polifulereno, as isotermas π-A indicaram que dependendo do solvente, o arranjo das moléculas é alterado, indicando maior solubilidade e menor nível de agregação, e vice-versa. Nas medidas de UV-Vis e VC também foi evidenciada a influência do solvente, estando diretamente relacionada à absorção máxima e diferença na posição do pico de absorção, além dos deslocamentos dos picos de oxidação e redução. Na junção entre cálculos de DFT e medidas de CV e UV-Vis, o método DFT/B3LYP/6-31+G(d) fornece valores de LUMO próximos aos valores experimentais, sendo uma ferramenta importante para comparação de resultados, pois não há estudos desses polifulerenos na literatura.

Palavras-chave: DFT, HOMO, LUMO, B3LYP, doador de elétrons, aceitador de elétrons, polifulerenos.

LIST OF FIGURES

LIST OF TABLES

LIST OF ABBREVIATIONS

Acetonitrile: ACN

Benzodithiophene: BDT

Benzodithiophene-dione: BDD

Born-Oppenheimer: BO

Broken-Symmetry: BS

Bulk Heterojunctions: BHJs

Cadmium Telluride: CdTe

Copper Indium Gallium Selenide: CIGS

Coulomb-Attenuating Method: CAM

Configuration Interaction: C.I.

Cyclic Voltammetry: CV

Density Functional Theory: DFT

Dye Sensitized Solar Cells: DSSCs

Electron Affinities: EA

Generalized Gradient Approximation: GGA

Hartree-Fock: HF

Hamilton-Jacobi Equation: HJE

Highest Occupied Molecular Orbital: HOMO

Hohenberg-Kohn: HK

Independent Electron Pair Approximation: IEPA

Indium Tin Oxide: ITO

Ionization Energies: IE

Ionization Potentials: IP

Kohn-Sham: KS

Kohn-Sham-Roothaan: KSR

Langmuir-Blodgett: LB

Langmuir-Schaefer: LS

Linear Combination of Atomic Orbitals-Molecular Orbitals: LCAO-MO

Local Density Approximation: LDA

Long-Range: LR

Lowest Unoccupied Molecular Orbital: LUMO

Mean Signed Error: MSE

Multiconfigurational Self-Consistent Field: MCSCF

Multijunction Solar Cells: MJSCs

Open-Circuit Voltage: V_{OC}

Organic Solar Cells: OSCs

Polarizable Continuum Model: PCM

Poly[(2,6-(4,8-bis(5-(2-ethylhexyl)thiophen-2-yl)-benzo[1,2-b:4,5-b’]dithiophene))-alt-(5,5-(1’,3’-di-2-thienyl-5’,7’-bis(2-ethylhexyl)benzo[1’,2’-c:4’,5’-c’]dithiophene-4,8-dione)]: PBDB-T

Poly[(2,6-(4,8-bis(5-(2-ethylhexyl-3-fluoro)thiophen-2-yl)-benzo[1,2-b:4,5-b’]dithiophene))-alt-(5,5-(1’,3’-di-2-thienyl-5’,7’-bis(2-ethylhexyl)benzo[1’,2’-c:4’,5’-c’]dithiophene-4,8-dione)]: PM6

Poly[4,8-bis(5-(2-ethylhexyl)thiophen-2-yl)benzo[1,2-b;4,5-b']dithiophene-2,6-diyl-alt-(4-(2-ethylhexyl)-3-fluorothieno[3,4-b]thiophe ne-)-2-carboxylate-2-6-diyl)]: PTB7-Th

Perovskite Solar Cells: PSCs

Photovoltaic: PV

Restricted Hartree-Fock: RHF

Self-Consistent Field: SCF

Silicon: Si

Slater-Type Orbitals: STOs

Short-Range: SR

Tetrabutylammonium Perchlorate: TBAP

Thomas-Fermi: TF

Time Dependent: TD

Time-Dependent Kohn-Sham: TD-KS

Ultraviolet-Visible : UV-Vis

Uniform Electron Gas : UEG

2,2'-((2Z,2'Z)-((12,13-bis(2-ethylhexyl)-3,9-diundecyl-12,13-dihydro-[1,2,5]thia diazolo[3,4-e]thieno[2",3'':4',5']thieno[2',3':4,5]pyrrolo[3,2-g]thieno[2',3':4,5]thieno[3,2-b]indole-2,10-diyl)bis(methanylylidene))bis(5,6-difluoro-3-oxo-2,3-dihydro-1H-indene-2,1-diylidene))dimalononitrile : Y6

3,9-bis(2-methylene-(3-(1,1-dicyanomethylene)-indanone))-5,5,11,11-tetrakis(4-hexylphenyl)-dithieno[2,3-d:2',3'-d']-s-indaceno[1,2-b:5,6-b']dithiophene : ITIC

2-[(2*E*)-2-[[16-[(*E*)-[1-(dicyanomethylidene)-3-oxoinden-2-ylidene]methyl]-3,3,13,13tetrakis(4-hexylphenyl)-7,10,17,20-tetrathiahexacyclo[9.9.0.0^{2,9}.0^{4,8}.0^{12,19}.0^{14,18}] icosa-1(11),2(9),4(8),5,12(19),14(18),15-heptaen-6-yl]methylidene]-3-oxoinden-1-ylidene]propanedinitrile : O6T-4F

SUMMARY

CHAPTER 1

1. Introduction

1.1 Organic solar cells

The population growth and global economic activities result in an increasing expansion in the production, distribution and consumption of energy, which leads to increased efforts in scientific studies to develop alternatives regarding the use of fossil fuels and their impacts on the environment [1, 2]. With more than 80% of the energy coming from fossil fuels, along with its depletion and increased CO_2 emissions caused by its combustion, sustainable energy sources are already in use, such as solar energy and wind energy, to help supply the energy demand [3, 4]. Thus, the development of devices that can convert solar energy constitutes a very important study and a vast potential for application, since solar energy is the only inexhaustible source of energy on Earth [5]. One of the tools for converting solar energy into electrical energy are solar cells or photovoltaic devices [6]. Consequently, studies aimed at improving the efficiency of devices in converting solar energy into electrical energy become essential [6].

The basic principle of operation of a solar cell is the photovoltaic effect that was first observed by the French physicist Alexandre Edmond Becquerel (1820-1891) in 1839 [7, 8]. Becquerel observed the generation of electric current illuminating platinum electrodes, covered with silver bromides or silver chloride, immersed in electrolyte solution [7, 8]. The first solar cell, consisting of a layer of selenium covered by a thin film of gold, was fabricated and studied by Charles Fritts in 1884, but had a very low efficiency [9]. The first solar cell with reasonable efficiency was developed at Bell Laboratories, in 1953, through studies of energy sources and diffusion in the solid state at p-n junction by Pearson, Fuller and Chapin [10]. The solar cell was fabricated using silicon (Si) and achieved an efficiency of around 6% [10]. In the 1960s, with the advancement of technology, the efficiency of a silicon solar cell, with AM1 illumination, was 12% to 13%. The violet cell reached an efficiency of 16% in 1973 [11]. A Si-based solar cell using a non-reflecting light system (black cell), in 1974, showed an efficiency between 18% and 19% [11]. Nowadays, Geisz and coworkers fabricated in the laboratory an inorganic multijunction solar cell (six-junction III–V) reaching an efficiency of 47.1% [12]. The device has six junctions of active layers based on gallium arsenide, a very expensive material in relation to common Si, in addition to a complex and relatively expensive fabrication process due to the much slower vapor deposition processes used [12]. Therefore, efforts continue in the search and development of low-cost solar cells.

The technological evolution of solar cells is usually divided into three categories called as first, second and third generation devices [6]. The first-generation one is based on solar cells fabricated using monocrystalline and polycrystalline Si wafers [6]. The devices in this generation present an efficiency of up to 24% and are well established in the market, however they need a large amount of Si in the wafers, which raises their costs [6]. The second generation one innovates with the fabrication of flexible devices using thin film technology of semiconductor materials such as amorphous Si, cadmium telluride (CdTe), and copper indium gallium selenide (CIGS) [6]. This generation introduces new features such as new fabrication techniques reduced amount of material leading to reduce costs compared to the first generation [6]. The third generation one brings the exploration of new materials and architectures in solar cells, seeking to lower production costs and higher efficiencies [6]. Some examples of such devices are multijunction solar cells (MJSCs), dye sensitized solar cells (DSSCs), quantum dot-sensitized solar cells, organic solar cells (OSCs), and perovskite solar cells (PSCs) [6].

The chart in Figure 1 shows the highest efficiencies for solar cells from 1976 to the present, being divided into 5 categories (multifunctional cells, single junction gallium arsenide cells, crystalline silicon cells, thin film technologies, photovoltaic (PV) emerging), and subdivided into 28 subcategories [13]. The chart is maintained and updated every year by the National Renewable Energy Laboratory which is a national laboratory of the U.S. Department of Energy [14].

Figure 1. The highest efficiencies for solar cells from 1976 to the present.

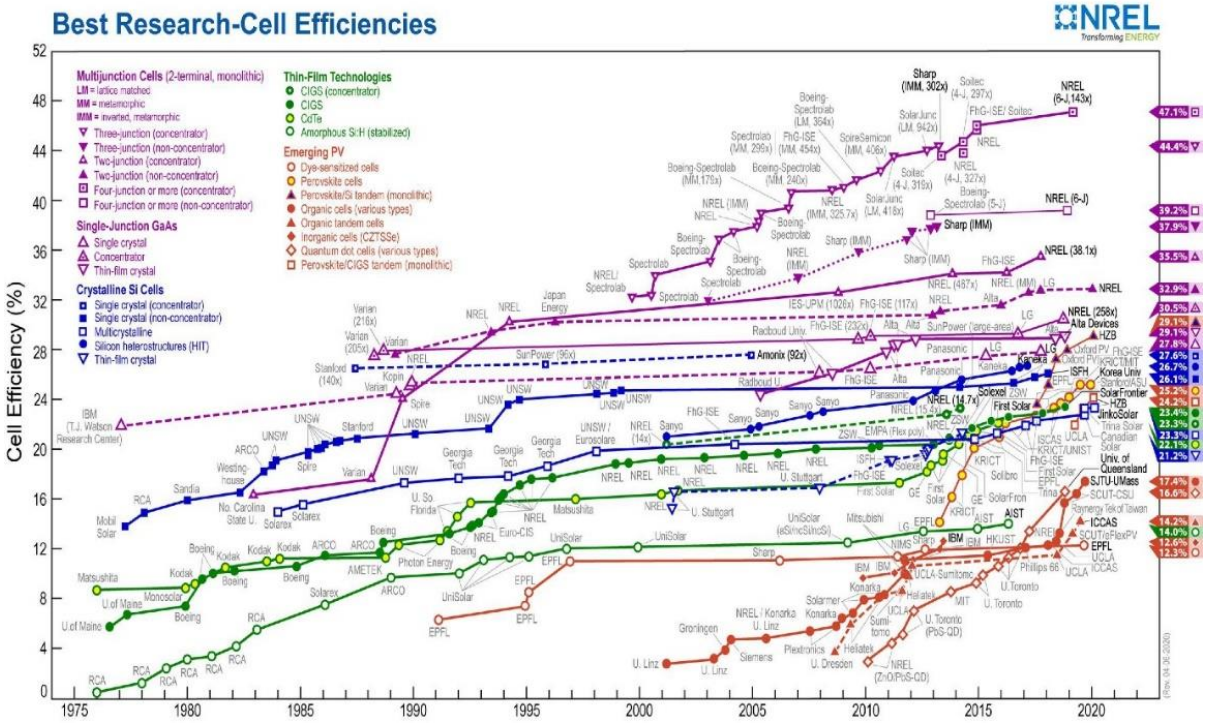

Source: Extracted from [13].

Currently, photovoltaic devices based on inorganic materials, mainly in crystalline Si, lead the world market with higher stability and efficiencies [15]. The multijunction devices present high efficiencies, however they use several expensive inorganic materials, mainly III-V semiconductors, and present a complex architecture, leading to high production costs [16, 17]. In emerging devices, perovskite solar cells show promising efficiencies, but are based on heavy metals, such as lead, making them toxic to the environment [18, 19]. Still in emerging devices, there is a great interest in organic solar cells due to the study and use of low-cost organic materials and simple solution processing method, in addition to the flexibility of the devices and large production volume [20, 21].

Using photoactive heterojunctions, OSCs have been widely studied and highlighting with devices reaching efficiency around 16-18% [22, 23]. The photovoltaic effect in OSCs occurs by means of the electronic structure of the arrangement of carbon and heteroatoms on the molecular level, which leads to different electron donor (p-type) or acceptor (n-type) characteristics for each molecule and the species are locally and globally neutral, most of the time [24]. The desired semiconductor character of these organic materials is assured by the Peierls distortion mechanism, which creates the energy gaps necessary for ultraviolet-visible (UV-Vis) light absorption [24]. Then, under illumination, following a $\pi \rightarrow \pi^*$ transition, neutral

excitons can be formed either in one or both materials (Figure 2) [25, 26]. If one has a large enough energy offset between the lowest unoccupied molecular orbital (LUMO) of the p-type material and the LUMO of the n-type one, the exciton will dissociate via an ultrafast electron transfer into long-lived charged species called polarons (namely, an electron on the n-type molecule and a hole on the p-type one) [25, 26]. The same process can happen when the highest occupied molecular orbital (HOMO) offsets are large enough as well [25, 26]. In order to avoid exciton recombination, the bulk heterojunctions (BHJs), i.e., a blend of an electron donor and an electron acceptor material is the key component in OSCs for improvement of the efficient [27, 28, 29].

Figure 3 shows a typic energy levels configuration of donor and acceptor materials and the charge cascade processes in the device [28]. In this type of heterojunction (Figure 4), small electron donor and acceptor domains are mixed, guaranteeing short distances for diffusion, and leading to efficient dissociation of excitons at the interface of these domains before recombination [27, 28, 29]. The difference in HOMO and LUMO between donor and acceptor layers creates electrostatic forces at the interface [27, 28, 29]. Give an appropriate of materials, such differences generate an electric field that leads to the efficient break-up of excitons into electrons and holes [27, 28, 29]. After exciton splitting, free electrons and holes are transported in the acceptor and donor networks (Figure 2 and 4) [27, 28, 29]. The free electrons are then accepted by the material with lower LUMO level and holes by the material with higher HOMO [27, 28, 29]. The transportation of charge carriers in organic semiconductors mostly takes place by hopping from one localized state to the next, until reaching to their respective electrodes [27, 28, 29].

Figure 2. Explanation of basic operational physics that is unique to OSCs.

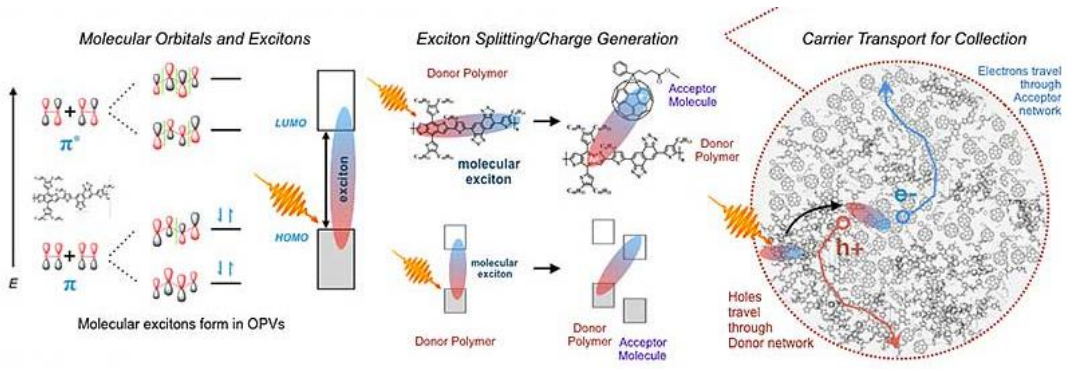

Source: Extracted from [30].

Figure 3. Schematic diagram showing the energy level of the materials and the charge cascade process in a BHJ.

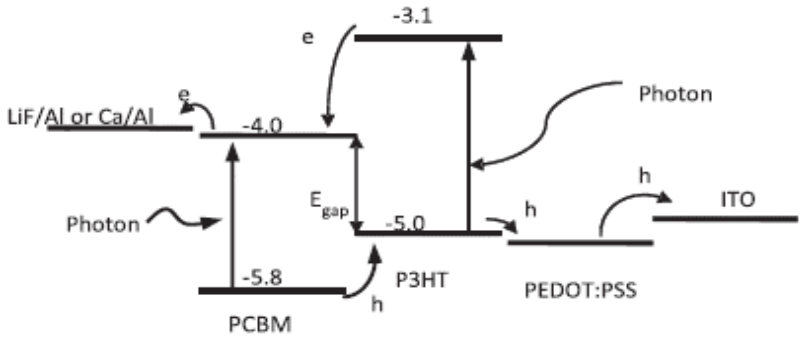

Source: Extracted from [28].

Figure 4. Schematic diagram of the BHJ in 2D and 3D in an OSC.

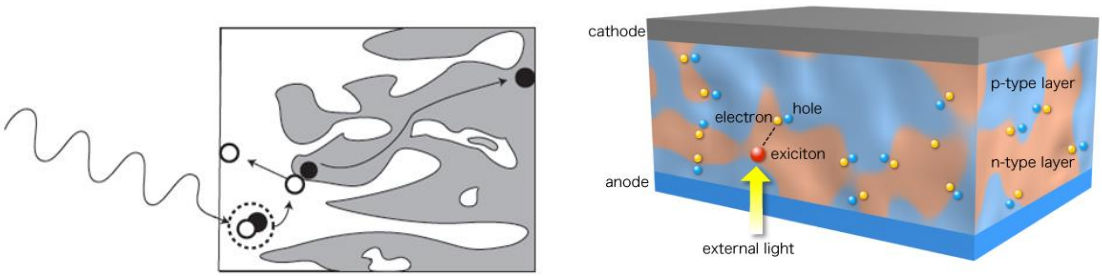

Source: Adapted from [29, 31].

In the past decades, a conjugated polymer and a fullerene derivative have been the most commonly used electron donor and electron acceptor, respectively [32, 33, 34]. Recently, non-fullerene acceptor materials, particularly small molecules and oligomers, have emerged as a promising alternative to replace fullerene derivatives [35, 36, 37]. Compared to fullerenes, these new acceptors are generally synthesized from diversified, low-cost routes based on building block materials with extraordinary chemical, thermal, and photostability [35, 36, 37].

So, the use of electron donating polymers combined with fullerene and non-fullerene electron acceptors in active layers of OSCs has shown significant efficiency in devices [38]. Fu et al. showed that active ternary layers using donor polymers with fullerenes and non-fullerenes acceptors showed higher efficiency than in binary active layers (donor polymers only with non-fullerenes) [39]. The optical absorption of fullerene is complementary to that of polymer and non-fullerene, in addition to bringing higher stability to the device when exposed to the environment [39]. Meng et al. fabricating a device with two layers of BHJs, each combining different electron

donor and acceptor polymers, achieved an efficiency of 17.3% [40]. In the first layer, a mixture of donor and non-fullerene acceptors was used, and in the second layer the donor polymer was mixed with fullerene and non-fullerene acceptor [40]. The final overlap of the absorbances showed that the materials absorbed a large part of the solar spectrum [40]. However, the device required complex and careful fabrication with several layers, including a zinc oxide (ZnO) one to ensure charge transfer between the two layers and the electrodes [40].

In this context, the computational quantum chemistry plays an important role for understanding and designing new organic materials to optimize OSCs performance [41]. Distinct molecular modelling techniques can be chosen considering the type of system under study and the properties that are required to be described [41]. Thereby, several approaches exist to treat either small (a few dozen atoms) or big molecules (several hundred atoms), ranging from electronic structure-based *ab initio* methods to molecular mechanics ones [42]. Such approaches will be discussed in the next section.

1.2 Molecular modelling techniques

As our studies were restricted to methods involving the electronic structure of molecules, the advantages and disadvantages of some widely used methods at this level of structure are presented here.

The study of the electronic structure of molecules requires the knowledge of the solutions of the Schrödinger equation [43]. The impossibility to reach the analytical solutions of this integrodifferential equation has led theoretical chemists to develop a whole strategy and a set of methods allowing to reach and calculate the main observables with a precision that is constantly increasing with the development of the computational capacity [43].

In the Born-Oppenheimer (BO) approximation the basic assumption is that of the independent particle model which proposes to write at order zero an eigenfunction of the adiabatic electronic Hamiltonian (stationary state) as a product of functions depending on only one electronic variable (spin-orbits) [43]. This hypothesis completed the necessity to antisymmetrize the simple product of spin-orbitals, and on the other hand, the adoption of the model of the double occupation of space functions, is at the basis of the self-consistent field (SCF) model whose objective is the determination of molecular orbitals [43].

In particular, the Restricted Hartree-Fock (RHF) method allows to account for multi-electron interactions by a model that stipulates that each electron is in an average field of the others (independent-particle model) always in the hypothesis of the double occupation of the

molecular orbitals [44]. From these approximations it results an error on the evaluation of the electronic energy which, while being weak (a few percent of the total electronic energy), has disastrous consequences on the calculation of quantities such as orbital energies, binding energy, etc [44]. Unlike the RHF solution which corresponds, as we have just recalled, to the description of a Slater determinant made up of N/2 doubly occupied orbitals (the other orbitals being empty), the exact solution that we are trying to describe by taking into account the correlation is in fact made up of an infinite number of configurations that can be thought of as excitations with respect to the N-electron RHF determinant in an infinitely large base. This comes out of the fact that only the occupied orbitals are used in the energy minimization process of the N electron system. For a more appropriate description one should also consider the other (virtual) states also occupied. And, of course, it is impossible to work in a complete or infinite basis.

Various methods are then proposed by theoretical chemists to evaluate as accurately as possible this correlation. Three types of approaches are used: 1) the methods aiming at solving variably the Schrodinger equation in the eigenstates by using a basis of Slater determinants or configurations. These are Configuration Interaction (C.I.) type approaches [45]; 2) perturbation methods requiring the definition of a minimal basis and a partition of the Hamiltonian operator adapted to ensure the convergence of the perturbation series in a Rayleigh-Schrodinger type approach [46]; 3) Pairwise methods which consist in evaluating the correlation energy of pairs of electrons assumed without interactions (Independent Electron Pair Approximation - IEPA) or in interaction (Coupled Pair Theory) [47, 48].

On the contrary, in the Multiconfigurational Self-Consistent Field (MCSCF) methods, the objective is to optimize with the use of a variational method both the monoelectronic functions used and the multiconfigurational development of the eigenfunction of the electronic Hamiltonian [49, 50, 51]. Among the numerous developments proposed, the Complete Active Space Self-Consistent Field (CASSCF) approaches lead to the development of the multiconfigurational wave function on the totality of the configurations generated by the set of all possible excitations in a restricted space of occupied and virtual molecular orbitals (active space) [52].

However, the dimensional aspect of the systems selected by the experimenters in the OSCs processes (without mentioning the effects of the environment, the solvent, etc, which are generally neglected and considerably increase the dimension of the system to be modelled)

constrain the researchers in the use of fast approaches, although more approximated, but able of treating electronic correlation like the Density Functional Theory (DFT) [53].

Within the DFT approach which is actually the most known one, defining LUMO (or whichever other orbital) is not a problem often overlooked by modelers [54]. This is due to the fact that DFT is not a wave function method and, hence, it does not lead to explicit orbitals, but to Kohn-Sham (KS) ones [54, 55]. These KS orbitals have been, for a long time, viewed as an auxiliary concept, not necessarily meaningful and just a way to build the total density [54, 55]. This is so based on the fact that, in the process of construction of these orbitals, an approximative exchange-correlation potential has to be used, and it may keep reality away of their definition [54, 55]. A complete and extensive discussion on the evolution of this concept is done by Stowasser and Hoffmann, but we can jump to the general conclusion achieved by Baerends et al., who argue that these orbitals are very suitable for qualitative, chemical applications [55, 56]. That is why care must be taken if one wants absolute LUMO energy values when designing new molecules [57]. Furthermore, identifying the open-circuit voltage (V_{OC}) via the LUMO energies relies on a one-electron picture (orbital relaxation is not considered) and on the validity of the Koopmans' theorem [58].

In the same time, the calculation of the LUMO energies, can be done experimentally by electrochemical methods, as cyclic voltammetry (CV), and the values so-obtained do not considering approximations to the energies of this orbital as well. The usual procedure consists of measuring the onset reduction potential of the molecule to calculate LUMO energy and correlate it with the electron affinity of a standard molecule, assuming the validity of Koopmans' theorem [59].

McCormick et al. reported in their very useful work on conjugated polymers that the use of DFT methods could be justified in the OSCs context [60]. We believe that the approach proposed by McCormick is even the better compromise disponible available today between theoretical DFT LUMO estimation and experimental CV LUMO energy measurement. In order to situate the limits avoided by McCormick and collaborators by the use of DFT in the OSCs context it is necessary look at to the strengths and weaknesses of each of the computational techniques disponible for the modeler.

Post-DFT treatments appropriate to describe open shell states exist and allow to solve all or part of the problems above mentioned. Let us first mention the Broken-Symmetry (BS) approach which is certainly one of the approaches that allows the study of higher dimensional systems and which is among the most used to "estimate" the energy of multi-configuration

states in KS-DFT [61, 62, 63, 64]. Indeed, its implementation does not require any additional methodological input to what is commonly found in a standard quantum chemistry program. The principle is to approximate the "multi-deterministic" state by a single Slater determinant, which allows the use of KS-DFT [61, 62, 63, 64]. This determinant, which is not an eigenvector of the S^2 operator, is said to be broken symmetry [61, 62, 63, 64]. The only way to obtain such a determinant is to use the unrestricted formalism [61, 62, 63, 64]. This formalism allows the space parts of the α and β orbitals to be different, unlike the restricted formalism [61, 62, 63, 64]. Nevertheless, this formalism suffers from the spin contamination problem which limits the accuracy of such an approach compared to the multi-determinant approaches cited above [61, 62, 63, 64]. The Yamaguchi method is the most widely used the BS approach at present [65, 66, 67, 68]. The simplest of the open layer states consists of two electrons located in two orbitals leading to the description of a singlet state, called open shell system, and a triplet state. The Yamaguchi method is based on the approximation that the unique determinant BS sought is a pure linear combination between the singlet state and the triplet state and that the spin polarization introduced by the unrestricted formalism is negligible in the triplet state [65, 66, 67, 68]. Thus, the BS determinant can be expressed very easily and cheaply [65, 66, 67, 68]. Another advantage of these approaches is that it is commonly accepted that for the most classical functionals in the molecular domain (hybrid-Generalized Gradient Approximation (GGA) such as B3LYP, PBE0, etc), the BS approach with the Yamaguchi formula represents more or less correctly the open shell system state and at lower computational cost [65, 66, 67, 68].

However, this should not make us forget the main limitation of this approach. One may wonder what is the meaning of using the mean value of the S^2 operator in DFT. Indeed, this value is most often computed as in wave function theory on the determinant KS by a 2-body operator. This determinant is that of a fictitious system without interaction and this average value should normally be calculated on the wave function of the real system. Experience shows that the BS method is efficient when the difference between the average value obtained for the KS determinant and the real system is small, which is unfortunately not the case in the systems we have studied.

A last alternative to the BS methods exists, and it is the Spin-Flip approaches [69]. Shao, Head-Gordon and Krylov have proposed an approach to calculate the low spin and open layer states using Time Dependent (TD)-DFT [69]. In a very general way, the principle is to compute the $m_s = 1$ state of the triplet (unrestricted formalism) and to make a time dependent perturbation

with a spin flip. We thus obtain all the mono-excitations with a spin change [69]. The goal is to obtain in fine the states characterized by the determinants $m_s = 0$ allowing to describe correctly the low spin state [69].

So it is finally in this state of mind and aware of the advantages, disadvantages and limitations of each approach that we conclude that the most efficient approach at present to describe both singlet excited states and the orbital parameters of the molecules involved throughout the excitation process in the OSCs domain is the one based on the joint description of the singlet ground state and its first triplet excited state at the KS-DFT level in the spirit of the spin-flip method as very efficiently shown by McCormick from 2013.

As we have just recalled, the use of post-DFT treatments allows to more or less accurately access to energy magnitudes of the HOMO, LUMO and excited triplet and singlet states parameters of organic molecules involved in OSCs parameters as short circuit current and open-circuit voltage and linked with power conversion efficiency. But the interest in producing these models does not stop there.

Last reason to study triplet states concern the role of charge recombination to triplet excitons in organic solar cells [70, 71, 72]. In particular, for Gillett and collaborators the organic solar cells have low open-circuit voltages because of their short optical bandgaps, owing to non-radiative recombination [73]. In particular, authors showed that in most organic solar cells that use non-fullerene acceptors, the majority of charge recombination under open-circuit conditions proceeds via the formation of non-emissive non-fullerene acceptors triplet excitons via the way of the first excited singlet state S_1. These non-radiative loss pathways must be identified and suppressed. Once again, the modelling can be a very useful tool in this domain but only if the methods used are able to accurately describe open shell systems like T_1 and S_1 (which refers the reader to the considerations mentioned above).

1.3 Objectives

The main objective of this work is set out the general considerations for the use of DFT approaches in particular when one has to describe one or more electronic states of more or less strongly correlated electrons. To estimate accurate values on molecular orbital energies a series of DFT calculations were performed in singlet and triplet states on a set of promising donor-acceptor pairs in OSCs. In addition, to study polyfullerenes and compare theoretical and experimental values, DFT was used to geometry optimizations and determine HOMO and

LUMO energy levels (monomers) with Langmuir-Schaefer thin films properties obtained experimentally.

CHAPTER 2

2. Methodology

2.1. The Schrodinger equation

In 1926, through the publication of a series of papers called "Quantization as an Eigenvalue Problem" (*Quantisierung als Eigenwert problem*), Schrodinger presents the problem of determining the orbital energies of the electron in an atom as an eigenvalue problem. [74]. In these series of papers, Schrodinger proposed a new equation combining wave matter descriptions with the Hamilton–Jacobi equation (HJE) in the time-independent form [74]. This new equation we now know as the Schrödinger equation and is identical to the matrix equation suggested by Heisenberg [75, 76].

The HJE is an extremely powerful and sophisticated method for solving the equations of motion in analytical mechanics [77]. The method is based on the search for a canonical transformation that is capable of making the transformed Hamiltonian identically zero [77]. HJE is particularly important as it is the only mathematical formulation of mechanics in which the motion of a particle can be represented as a wave, and for this reason, HJE is considered the closest approximation of classical mechanics to quantum mechanics [77, 78]. The complete and time-dependent HJE is given by:

$$\frac{\partial S}{\partial t} = -H(q_i, p_i, t) = -H\left(q_i, \frac{\partial S}{\partial q_i}, t\right) \tag{2.1}$$

where L is the Lagrangian of the system. The Lagrangian is the kinetic energy minus the potential energy of the system. The S is a generating function that depends on spatial coordinates (q_i), momenta (p_i) and time (t) [77, 79]. The generating function $S(q_i, t)$ is central to analytical mechanics, and while everything that can be known about the system can be derived from it, it is defined by [77, 79]:

$$S = \int_{t_1}^{t_2} L(q_i, p_i, t)dt \tag{2.2}$$

From $S(q_i, t)$ it is possible to obtain the canonical moments of system as [77,79]:

$$p_i = \frac{\partial S}{\partial q_i} \tag{2.3}$$

and the Hamiltonian as [77, 79]:

$$H = -\frac{\partial S}{\partial t} \tag{2.4}$$

In case of conservative systems, the Hamiltonian is the total energy E (sum of kinetic and potential energies), which is constant [77, 79]. Thus, applying the Equation 2.4 to the hydrogen atom, and considering $\partial S/\partial t = -E$, the Equation 2.1 becomes [77, 78, 79]

$$H\left(q, \frac{\partial S}{\partial q}\right) = E \tag{2.5}$$

which is also called the time-independent HJE or the energy conservation equation [77, 78, 79]. Applying a logarithmic function Ψ spatial which is the logical equivalent of S in Equation 2.5 [78, 79]

$$S = i\hbar ln(\Psi) \tag{2.6}$$

being Ψ defined by [78, 79]:

$$\Psi = \exp(-\frac{iS}{\hbar}) \tag{2.7}$$

Since Equation 2.7 is considered to be the amplitude of matter waves, the finitude and definition of can be assumed by a normalization condition [77, 78, 79]:

$$\int |\Psi|^2 dV = 1 \tag{2.8}$$

This Ψ is called a wavefunction [78, 79]. Substituting Equation 2.6 in Equation 2.1, using this wavefunction, into the time-dependent and time-independent HJEs in Equations 2.1 and 2.5 gives [78, 79]:

$$\hat{H}\Psi = i\hbar \frac{\partial \Psi}{\partial t} \tag{2.9}$$

and

$$\hat{H}\Psi = E\Psi \tag{2.10}$$

respectively. Equations 2.9 and 2.10 are called the time-dependent and time-independent Schrödinger equations, respectively, and the Hamiltonian is replaced by the Hamiltonian operator acting on spatial functions [78, 79]. Because of its definition in terms of the principal function S, Ψ also has no physical meaning and cannot be measured, but contain all system information [78, 79]. Considering a one-dimensional and time-independent system of particles, the Hamiltonian operator is [78, 79]:

$$\widehat{H} = \sum_i \frac{p_i^2}{2m_i} + V = \sum_i \frac{1}{2m_i}\left(\frac{\partial S}{\partial q_i}\right)^2 + V = -\sum_i \frac{\hbar^2}{2m_i}\frac{1}{|\Psi|^2}\left(\frac{\partial \Psi}{\partial q_i}\right)^2 + V = E \qquad (2.11)$$

For energy conservation, it is obtained [78,79]:

$$-\sum_i \frac{\hbar^2}{2m_i}\left(\frac{\partial \Psi}{\partial q_i}\right)^2 + (V - E)|\Psi|^2 = 0 \qquad (2.12)$$

Using the variational method, the stationary condition is obtained under the normalization condition [78,79]:

$$-\sum_i \frac{\hbar^2}{2m_i}\left(\frac{\partial^2 \Psi}{\partial q_i^2}\right) + (V - E)\Psi = 0 \qquad (2.13)$$

For a multidimensional system:

$$-\sum_i \frac{\hbar^2}{2m_i}\nabla_i^2\Psi + (V - E)\Psi = 0 \qquad (2.14)$$

here the moment p_i is transformed into the moment operator $p_i = -i\hbar\nabla_i$, which produces discrete energy levels under the boundary condition of the potential V to make the wave functions finite [78, 79]. The discrete energy values and the corresponding wave functions are called eigenvalues and eigenfunctions, respectively [78, 79].

Since the Schrödinger equation was developed, various realistic and idealistic interpretations of the wavefunction has been vigorously discussed [78]. Schrödinger originally regarded the wavefunction as a description of real physical wave, where the physical existence of a matter consists only of waves [78, 80]. As this interpretation has many serious problems, other interpretations soon emerged. Born proposed the probabilistic interpretation of the wave function, becoming the mainstream interpretation of the wavefunction today [78, 80]. According to Born, what has direct physical meaning been not spatial-temporal wave functions,

which may even be imaginary functions [81]. The physical meaning is in the magnitude $|\Psi(\vec{r},t)|^2$ [81]. The squared modulus of the wave function gives the probability density probability of finding the particle at point x, at time t:

$$\rho(x,y,z,t) = \frac{dP(\vec{r},t)}{dV} = |\Psi(\vec{r},t)|^2 = \Psi^*(\vec{r},t)\Psi(\vec{r},t) \tag{2.15}$$

where $dP(\vec{r},t)$ is the probability that a single particle is at position $\vec{r}$, inside the volume $dV = dxdydz$ (in Cartesian coordinates), in the time t, per unit of dV. This interpretation is considered idealist (orthodox position) and only focuses attention on the existence probability in discussions on the wave-particle relation, where the observations not only disturb what is to be measured, they produce it, and the particle assume a definite position [78, 80]. Eventually, the Copenhagen school, led by Bohr, Heisenberg and Pauli, advocated Born's probabilistic interpretation [82]. Some alternative realistic interpretations of the wave function have been proposed and widely studied, as for example, the Schrödinger's cat and Everett's many-worlds interpretation [83, 84].

2.2 The many-body Schrodinger equation

The physical properties of matter at the atomic level are described using the formalism of quantum mechanics [80]. In the case of optoelectronic properties, for example, the wave functions of electrons are fundamental to describe the frontier energy levels in molecular orbitals [85]. Thus, a multielectron atom systems are considered as a many-body problem [86]. Thus, the interactions of a system with N electrons and M nuclei, with coordinates $\{\vec{r}_i\} = (\vec{r}_1, \vec{r}_2, \dots, \vec{r}_N)$ and $\{\vec{R}_\alpha\} = (R_1, R_2, \dots, \vec{R}_M)$, respectively, can be described by the non-relativistic Hamiltonian operator [87]:

$$\hat{H} = \hat{T}_n + \hat{T}_e + \hat{V}_{nn} + \hat{V}_{ne} + \hat{V}_{ee} \tag{2.16}$$

The terms $\hat{T}_n$ and $\hat{T}_e$ represent the kinetic energy of nuclei and electrons, respectively, given by:

$$\hat{T}_n = \sum_{\alpha<1}^{M} -\frac{1}{2M_M}\nabla^2_{\vec{R}_\alpha}, \quad \hat{T}_e = \sum_{i=1}^{N} -\frac{1}{2}\nabla^2_{\vec{r}_i} \tag{2.17}$$

where, M_M is the mass of the M-th nucleus. Atomic units are a convenient system of units commonly used in electronic property calculations, so, $m_e = \hbar = e = 1$, where m_e and e are

the electron's mass and charge, respectively; furthermore, it is also $4\pi\varepsilon_0 = 1$. The Coulomb interactions between nucleus-nucleus ($\hat{V}_{nn}$), nucleus-electron ($\hat{V}_{ne}$) and electron-electron ($\hat{V}_{ee}$) are given by:

$$\hat{V}_{nn} = \frac{1}{2}\sum_{\substack{\alpha=1 \\ \alpha\neq\beta}}^{M}\sum_{\beta=1}^{M}\frac{Z_\alpha Z_\beta}{\left|\vec{R}_\alpha - \vec{R}_\beta\right|}, \hat{V}_{ne} = \sum_{\alpha=1}^{M}\sum_{i=1}^{N} -\frac{Z_\alpha}{\left|\vec{R}_\alpha - \vec{r}_i\right|}, \hat{V}_{ee} = \frac{1}{2}\sum_{\substack{i=1 \\ j\neq 1}}^{N}\sum_{j=1}^{N}\frac{1}{\left|\vec{r}_i - \vec{r}_j\right|} \quad (2.18)$$

with Z_α and Z_β the atomic number of nuclei, $\vec{R}_\alpha$ and $\vec{r}_i$ the positions of nuclei and electrons, respectively. In the interaction of the system, neglecting the nuclear motions is one of the most important approaches, as it makes possible the decoupling of the nuclear and electronic parts in the time-independent Schrödinger equation with the application of the Hamiltonian (Equation 2.16) [88]. As the atomic nucleus is heavier than the electron ($m_p/m_e \approx 1836$), it is considered that electrons move much faster than nuclei, so in the absence of nuclei movement there is no exchange of thermal energy with the external environment [88]. This approximation is adiabatic and known as the BO approximation [88]. With electronic movement being considered instantaneous in relation to nuclear movement, decoupling is given by:

$$\psi\left(\{\vec{r}_i\},\{\vec{R}_\alpha\}\right) = \psi_n(\{\vec{R}_\alpha\})\psi_e(\{\vec{r}_i\},\{\vec{R}'_\alpha\}) \quad (2.19)$$

where $\vec{R}'_\alpha$ indicates the parametric dependence of the wavefunction on the position of the nuclei. After decoupling and applying only the wavefunction of the electronic part to the Schrödinger equation, a new Hamiltonian is written:

$$\hat{H}_e = \hat{T}_e + \hat{V}_{ne}\left(\{\vec{r}_i\},\{\vec{R}'_\alpha\}\right) + \hat{V}_{ee}(\{\vec{r}_i\}) \quad (2.20)$$

With the BO approximation, the interaction term of the nuclei $\hat{V}_{nn}$, which can be considered constant, is omitted from the Equation 2.20 [88]. In addition, once electrons have a much higher velocity than the nucleus, the nucleus is considered fixed and generates an effective potential under which the electrons move. Thus, there is a new time-independent Schrodinger equation for the electronic part to be solved:

$$\hat{H}_e\psi_e(\{\vec{r}_i\},\{\vec{R}'_\alpha\}) = E_e\psi_e(\{\vec{r}_i\},\{\vec{R}'_\alpha\}) \quad (2.21)$$

Although the Schrödinger equation for the electronic part (Equation 2.21) is simpler, its analytical solution is not yet possible (quantum many-body problem), except for extremely simple systems such as the hydrogen atom and hydrogen-like atoms [80]. The numerical

solution is hardly viable due to the large number of variables, with three spatial coordinates per electron, in addition to the spin [87]. Thus, over the years, new quantum methods have been proposed to reduce the cost of this type of calculation and obtain information from N-electron atom systems [89].

2.3 The Hartree-Fock method

In 1928, in order to simplify the solution to the Schrodinger equation for N-electron atoms, Hartree proposed a solution method using BO approximation and assuming that each electron interacts only with the average potential of the other electrons [90]. As this approximation assumed independent electrons, the Hamiltonian operator is divided into terms for the different electrons and the wave function $\psi(\vec{r}_1, \vec{r}_2, \dots, \vec{r}_i)$ is represented as the product of different electronic wave functions $\phi_i(\vec{r}_i)$ [90]:

$$\psi(\vec{r}_1, \vec{r}_2, \dots, \vec{r}_i) = \phi_1(\vec{r}_1)\phi_2(\vec{r}_2) \dots \phi_i(\vec{r}_i) \tag{2.22}$$

With the variational method, which minimizes the energy value of each electron, the Schrödinger equation for obtaining the set of wave functions of an electron ϕ_i is represented as

$$\hat{H}(\vec{r}_i)\phi_i(\vec{r}_i) = \varepsilon_i\phi_i(\vec{r}_i) \tag{2.23}$$

Since the eigenvalue of the Equation 2.23, ε_i, is interpreted as an eigenenergy for the movement to the i-th electron, the total wave function can be obtained by solving the eigenequation for each electron. Thus, in Hartree method, the total self-energy is the sum of the self-energy corresponding to different electronic movements,

$$\hat{H}\psi = (\varepsilon_1 + \varepsilon_2 + \cdots + \varepsilon_i)\phi_1\phi_2\phi_i = \varepsilon\psi \tag{2.24}$$

However, the Hartree method does not consider that the wave function of electronic motion must be antisymmetric [89]. Since electrons are indistinguishable, and to satisfy the Pauli exclusion principle, the fermion particles must be represented by antisymmetric functions in terms of changing coordinates [91]. This is because the wave functions must be zero for the case where the same electron, with the same spin, occupies the same orbital. As a result, electrons always have antisymmetric wave functions [92, 93]. The new electron-electron interaction resulting from antisymmetrization is called the exchange interaction [89]. Thus, the antisymmetric wave function can be written as a determinant, as proposed, independently, by Heisenberg and Dirac [92, 93].

In 1929, Slater introduced the normalized determinant that guaranteed the antisymmetry of a many-electrons wave function [94]. In the Slater determinant, each row represents an electron and each column an spin-orbital. So, for the case of two or more electrons, the antisymmetric wavefunction is written by

$$\psi(r_1, r_2, \dots, r_N) = \frac{1}{\sqrt{N!}} \begin{vmatrix} \phi_1(r_1) & \phi_1(r_2) & \dots & \phi_1(r_N) \\ \phi_2(r_1) & \phi_2(r_2) & \cdots & \phi_2(r_N) \\ \vdots & \vdots & \ddots & \vdots \\ \phi_N(r_1) & \phi_N(r_2) & \dots & \phi_N(r_N) \end{vmatrix} \tag{2.25}$$

and its determinant is

$$\psi(r_1, r_2, \dots, r_N) = \frac{1}{\sqrt{N!}} det|\phi_1(r_1)\phi_2(r_2) \dots \phi_N(r_N)| \tag{2.26}$$

Then, in 1930, Fock applied the Slater determinant to the Hartree method and proposed the Hartree-Fock (HF) method [95]. Thus, the HF method is based on the HF equation (Equation 2.27) in which the total antisymmetric wave function is the combination of wave functions of each electron individually, and uses an operator that acts on each individual wave function, and with that, we obtain individual energies for each electron or orbital. This operator is called the closed shell Fock operator and is given by Equation 2.28.

$$\hat{F}\phi_i = \epsilon_i \phi_i \tag{2.27}$$

$$\hat{F} = \hat{h} + \sum_{j}^{n=N/2} (2\hat{J}_j - \hat{K}_j) \tag{2.28}$$

From the variational principle, in the Equation 2.28, $\hat{J}_j$ and $\hat{K}_j$ are called the Coulomb operator and the exchange operator, respectively, which are defined as

$$\hat{J}_j(r_1)\phi_i(r_1) = \int d^3r_2 \, \phi_j^*(r_2)\phi_j(r_2)\frac{1}{r_{12}}\phi_i(r_1) \tag{2.29}$$

$$\hat{K}_j(r_1)\phi_i(r_1) = \int d^3r_2 \, \phi_j^*(r_2)\phi_i(r_2)\frac{1}{r_{12}}\phi_j(r_1) \tag{2.30}$$

When the Coulomb operator acts on the wave function it generates the Coulomb integral [89]. The Coulomb integral is the potential energy of electrostatic repulsion between two electrons in the same orbital [89]. Coulomb interactions are described as classical mechanical

interactions between electrically charged particles [89]. When the exchange operator acts on the wave function, the exchange integral is generated, where the electron is in an orbital on one side of the operator and a different orbital on the other side [89]. Unlike Coulomb interaction, exchange interactions are purely quantum interactions, have no classical analogue and are related to the antisymmetry of the wave function [89]. Due to these interactions, the total electronic energies are reduced, stabilizing the electronic states. A significant proportion of the exchange interactions are absorbed by the self-interactions of the electrons themselves [89]. Consequently, these self-exchange interactions remove the Coulomb potential of an electron [89]. The exchange interactions increase orbital overlap to produce attractions between orbitals [89]. As a result, these attractions lead to the delocalization of electron distribution, which causes the far-reaching nature of exchange interactions [89].

Then, using the HF equation in closed shell systems, the orbital energy ϵ_i is represented as

$$\epsilon_i = \int d^3r_1\, \phi_i^*(r_1)\hat{F}\phi_i(r_1) = h_{ii} + \sum_{j}^{n=N/2} (2J_{ij} - K_{ij}) \tag{2.31}$$

where $J_{ij}(r_1) = \int d^3r_1 d^3r_2\, \phi_i^*(r_1)\phi_j^*(r_2)\frac{1}{r_{12}}\phi_i(r_1)\phi_j(r_2)$ and is called as Coulomb integral; it represents the electrostatic (i.e. Coulombic) repulsion between an electron in ϕ_i and one in ϕ_j (ψii for repulsion between electrons in the same spatial orbital). K_{ij} is called as exchange integral, that arises from Slater determinant expansion terms that differ only in exchange of electrons, and is defined by $K_{ij}(r_1) = \int d^3r_1 d^3r_2\, \phi_i^*(r_1)\phi_j^*(r_2)\frac{1}{r_{12}}\phi_j(r_1)\phi_i(r_2)$. For this orbital energy, the total electronic energy is written as

$$E = 2\sum_{i}^{n} h_{ii} + \sum_{i,j}^{n}(2J_{ij} - K_{ij}) = \sum_{i}^{n}(\epsilon_i + h_i) \tag{2.32}$$

2.3.1 Basis sets

The HF equations can be solved numerically for atoms, but this method has been shown to be computationally inadequate for polyatomic molecules. Then, in 1951, Roothaan proposed a method, known as the Roothaan method, to solve the computational difficulty of implementing the HF method for molecular calculations [96]. In this method, Roothaan solved this problem by suggesting linear combinations of atomic orbitals through the HF equations,

with the functions used to represent molecular orbitals being written in terms of functions that represent atomic orbitals, thus forming the Hartree-Fock-Roothaan method [96]. The linear combination of atomic orbitals-molecular orbitals (LCAO-MO) approximation was proposed by Lennard-Jones, in 1929 [97]. Subsequently, Roothan's method was initially implemented for computational calculations in HF methods. It is noteworthy that Hall, also in 1951, independently suggested this method, which is also called the Roothaan-Hall method [98].

In LCAO-MO approximation the number of molecular orbitals (molecular eigenfunctions) is equal to the number of atomic orbitals (molecular eigenfunctions) included in the linear expansion. In a sense, n_{AO} atomic orbitals combine to form n_{MO} molecular orbitals, which can be numbered $p = i$ to n_{AO} and which may not all be the same. The expression (linear expansion) for the $\{\phi_i\}$ molecular orbital can be expanded as:

$$\phi_i(r) = C_{1i}\chi_1 + C_{2i}\chi_2 + C_{3i}\chi_3 + \cdots + C_{pi}\chi_p \tag{2.33}$$

or

$$\phi_i(r) = \sum_{p=i}^{n_{AO}} \chi_p(r) C_{pi} \tag{2.34}$$

being n_{AO} is the number of atomic orbitals. The expansion coefficient C_{pi} is called the molecular orbital coefficient and weight the contributions of the atomic orbitals to the molecular orbitals to be adjusted to get the best $\phi_i(r)$. Although $\{\chi_p\}$ is essentially the set of atomic orbitals, it is more efficient and general to use base functions modeling atomic orbitals. Thus, starting from the Hartree-Fock-Roothaan method, an incessant search for finite sets of bases that accurately describe the physical and chemical properties of atomic and molecular systems became intense.

The basic functions chosen are usually real and Slater or Gaussian type. A choice of base functions can be the Slater-type orbitals (STOs) which adequately describe the electronic behavior in regions near and far from the nucleus, and have been extensively used in atomic calculations. However, for molecular calculations, STOs are not desired, since multicentric integrals involving this type of function generate computational difficulties. In fact, the "four-center, two-electron integral problem" was once considered one of the greatest problems in quantum chemistry [85].

On the other hand, multicentric integrals involving Gaussian-type functions are easier to evaluate. Gaussian type basis functions were suggested by Boys, in 1950, and are widely used in quantum chemistry calculations, as they have a specific product rule for them ("Gaussian Product Theorem"), where the product of Gaussian-type functions is given by a

Gaussian-type function centered at a different point, and this dramatically speeds up two-electron integral calculations [99]. Based on this theorem, four-center integrals can be reduced to finite sums of two-center integrals and, in a next step, to finite sums of one-center integrals, and this dramatically speeds up two-electron integral calculations compared to the Slater orbitals, outweighing the extra cost of having more basic functions usually needed in a Gaussian calculus.

However, in the hydrogen atom wave function, the real atomic orbitals are close to the Slater-type function, $exp(-\zeta r)$, thus, as proposed by Boys, the use of the contracted Gaussian-type base function, which is linear combinations of Gaussian-type functions (Equation 2.35), are needed to simulate STOs, as a single Gaussian-type function gives a poor representation of a Slater-type function.

$$\chi_p(r - R_A) = \sum_{\mu} c_{\mu p} exp\left(-\alpha_{\mu p} |r - R_A|^2\right) \tag{2.35}$$

In this equation, the original Gaussian-type functions are called primitive functions to distinguish them from contracted ones. Primitive functions are specified only by the orbital exponent, $\alpha_{\mu p}$, contracted coefficient, $c_{\mu p}$ and coordinate vector of the center of the function, R_A. Primitive functions generally have a standardized form and are represented analogously to spherical harmonic functions to those corresponding to *s*, *p*, *d*, and *f* atomic orbitals as [89]

s function: $exp(-\alpha r^2)$

p function: $(x, y, z)exp(-\alpha r^2)$

d function: $(x^2, y^2, z^2, xy, yz, zx)exp(-\alpha r^2)$

f function: $(x^3, y^3, z^3, x^2y, x^2z, xy^2, y^2z, yz^2, xz^2, xyz)exp(-\alpha r^2)$

For contracted Gaussian base functions, several types of functions have been suggested [100, 101]. The minimal basic functions, e.g., STO-LG contain only primitive functions needed for each atom. The letter L represents the number of primitive Gaussian functions used to represent each Slater-type orbital in the atom.

Since the valence orbitals are responsible for chemical bonds, while the central orbitals hardly participate in bonds, the study of atomic orbitals can be divided into core and valence region. Thus, split valence basis functions use a contracted Gaussian-type function for central

orbitals and multiple contracted functions for valence orbitals. The notation for split valence basis sets, that arise from Pople-type basis functions, is typically X-YZWG [102]. In a minimal or single zeta basis set (SZ), there is one set of basis functions for each subshell occupied in the ground state of the atom. The double, triple, quadruple, quintuple, and hextuple zeta base sets are defined similarly and are in abbreviated forms denoted by DZ, TZ, QZ, 5Z, and 6Z. For example, in base 6-31G, "6-31" indicates the extent of contraction and division, where "6" means the use of contracted base functions from 6 primitive functions for central orbitals and "31" means the use of doubly divided valence basis functions combining contracted basis functions from three primitive functions with one uncontracted basis function for valence orbitals.

To incorporate the anisotropic nature of molecular orbitals originated from chemical bonds, the polarization functions are added to the basic sets, in addition to the divided valence basis. In Pople-type basis functions, the inclusion of polarization functions for heavy atoms is represented by an asterisk "*", such as "6-31G*", or letter d in parentheses (d). While two asterisks "**" or letter p in parentheses (p), indicate that the polarization functions p are also added to light atoms (hydrogen and helium).

Another common addition to basic sets is the addition of diffuse functions to account for loosely bound electrons. Adding diffuse functions is shown by a plus sign "+" in Pople-type basis functions. "6-311+G(d)" augments the sp diffuse functions by mixing s and p orbitals for all atoms except hydrogen atoms, and "6-311++G(2df, 2pd)" adds two diffuse functions d and one f to all atoms, except hydrogen, and two orbital functions p and one d for hydrogen.

In general, the equations of the HF method are solved using the SCF [89]. Basically, the SCF method follows these steps: 1) starts setting the molecular geometry (coordinates of atomic nuclei); 2) choose basis functions; 3) calculate one and two-electron integrals; 4) initial guess coefficients $\{C_i\}$, 5) compute the Fock matrix $\boldsymbol{F}$; 6) calculate Fock matrix; 7) solve Roothan equations for C_i ; 8) if SCF converges, calculate molecular properties or, if no, return to step 5 and continue with the calculation. This method is known as the SCF-HF method. Despite the simplicity of the procedure, it soon became clear that solving this equation is not trivial for usual molecular electronic systems.

2.4 Density Functional Theory

2.4.1 Thomas-Fermi-Dirac method

The solution of the HF equation, using the formalism of wave function manipulation, can be used for the electronic description of a system. Since the wavefunction for a single electron depends on three spatial variables plus one of spin, the solution for systems with a large number of electrons requires a high computational cost, due to the scaling of computational time for this type of solution.

A second totally different approach for calculating the electronic structures of atoms was initially developed by Thomas (1926) and Fermi (1928) treating electron density as a fundamental variable [103, 104]. This approach sought to show that the kinetic energy and potential energy of the electrons could be directly related to the electron density, $n(\vec{r})$, instead of the electron wave function, and thus the number of variables in the system depends only on three spatial coordinates, i.e., it is independent of the number of electrons in the system.

The starting point used by Thomas was that an atom can be approximated to a uniform electron gas model, where in electronic movements in solid crystals, electrons are uniformly distributed in the proportion of two per unit cell of L side and volume L^3 in addition to containing N non-interacting electrons evenly distributed for a grand total of N_e electrons [103]. Thus, the total kinetic energy of electrons is a functional of electron density $n(\vec{r})$ given by

$$T^{TF}[n(\vec{r})] = C_F \int d^3 r n^{5/3}(\vec{r}) \tag{2.36}$$

where $C_F = \frac{3}{10}(3\pi^2)^{2/3}$.

Deriving the same kinetic energy functional obtained by Thomas, Fermi completes the Thomas method, now known as the Thomas-Fermi (TF) method, using a Fermi statistic at the absolute zero point [104]. Thus, the total energy functional in the TF method for one atom is

$$E_{TF}[n(\vec{r})] = T[n(\vec{r})] + V_{ne}[n(\vec{r})] + V_{ee}[n(\vec{r})] \tag{2.37}$$

The TF method proved to be promising, but it did not formulate the terms of exchange (obtained in the HF model) and correlation, thus leading to the impossibility of calculations in real electronic states. Then, in 1930, Dirac proposed the first exchange functional of electron density $n(\vec{r})$, taking the distribution of electrons to be that of a uniform gas in each region where the atom is divided as in the Thomas–Fermi model [105]. Thus, Dirac expresses the

exchange contribution as a local density approximation (LDA) where the term depends on the electron density at one point

$$E_X^{LDA} = -\frac{3}{2}\left(\frac{3}{\pi}\right)^{1/3} \int d^3 r n^{4/3}(\vec{r}) \tag{2.38}$$

The Thomas-Fermi-Dirac (TFD) method cannot establish the uniqueness of the solutions and the existence of density functionals, and cannot reproduce chemical bonds quantitatively or qualitatively. Thus, this method was despised until the mid-1960s, but it is considered a springboard for the modern DFT [89].

2.4.2 Hohenberg-Kohn formalism

In 1964, the concept of the TF method was revived and the total energy was fully proposed (relating classical and quantum interactions) and expressed in terms of electron density by two Hohenberg-Kohn (HK) theorems [106]. From these theorems the ground state properties of a system can be expressed in terms of electron density, thus creating the bases of the DFT, and are presented below.

Theorem 1: For each electron density there is only a single external potential, V_{ne}, associated, i.e., the external potential is a unique functional of the electron density.

Theorem 2: A universal functional for energy $E[n(\vec{r})]$ can be defined in terms of electron density. The ground state density is the global minimum of this functional.

From the first theorem, in an electronic state, the number of electrons N per unit volume in a given state is the electron density

$$N = \int n(\vec{r}) d^3 r \tag{2.39}$$

The first theorem states that the ground state properties of the many-electron system depend only on electron density. Where, knowing the external potential, the terms of the Hamiltonian operator will be fixed as well as the electron density, consequently all observable properties of a quantum system can be determined, just like in the wave function. Among the observable properties is the total electronic energy, which is density dependent, which can be expressed by

$$E[n(\vec{r})] = T_e[n(\vec{r})] + V_{ne}[n(\vec{r})] + V_{ee}[n(\vec{r})] \tag{2.40}$$

where $V_{ee}[n(\vec{r})]$ lists all interactions between electrons.

The kinetic energy and interaction energy of a non-relativistic Coulomb system are described by universal operators, so Hohenberg and Kohn grouped all the functionals from Equation 2.40 that depended directly on the external potential into a single term called the HK functional, being a universal functional because electron density determines $E[n(\vec{r})]$ and $V_{ne}[n(\vec{r})]$. So, the total electronic energy can be rewritten as:

$$E[n(\vec{r})] = V_{ne}[n(\vec{r})] + F_{HK}[n(\vec{r})] \tag{2.41}$$

The second theorem states that the correct ground-state density for a system is one that minimizes the total energy through the functional $E[n(\vec{r})]$. Thus, by the variational principle, when the Hamiltonian is applied to an electronic density, other than that of the ground state, the system energy will always be higher than the ground state energy $E[n(\vec{r})] > E_0[n_0(\vec{r})]$. To find the ground state electron density, the Lagrange multiplier method is used, setting $\delta E[n(\vec{r})] = 0$ with the restriction that the total number of electrons is constant as $n(\vec{r})$ is varied. The variation theorem implies that the variation in electron density subject to restriction corresponds to an extreme, in this case, the minimum point:

$$\delta\left\{E[n(\vec{r})] - \mu\left[\int n(\vec{r})d^3r - N\right]\right\} = 0 \tag{2.42}$$

Equation 2.43 is the fundamental equation of the DFT, being the third part of the equality written as a function of the external potential.

$$\mu = \frac{\delta E[n(\vec{r})]}{\delta n(\vec{r})} = \hat{V}_{ne}(\vec{r}) + \frac{\delta F_{HK}[n(\vec{r})]}{\delta n(\vec{r})} \tag{2.43}$$

2.4.3 Kohn-Sham Formalism

Although the HK theorems are stated as the fundamental theorems of quantum chemistry, based on electron density, they say nothing about how to obtain the ground-state density, of which all observable properties of the system are functional. Then, in 1965, Kohn and Sham were the first to present a method for calculating the electronic structure of systems involving many particles using $E[n(\vec{r})]$ [107]. In this new method, it was considered that for each real system of interacting particles there would be an auxiliary system composed of non-interacting particles under the action of an effective potential capable of maintaining the spatial arrangement of these particles so that its electronic density is identical to that of the real system.

So, the KS method is a variational approach using the electron–electron interaction potential of the density functional to give the ground state energy, molecular orbitals and orbital energies by means of the Lagrange multiplier method.

By the TF model it is possible to calculate the kinetic energy as a function of the electronic density, considering a gas of non-interacting electrons, and knowing the wave function of the system, the determination of the kinetic energy of the system becomes a much simpler process. Given these characteristics, Kohn and Sham proposed a model of union of electronic density with the wave function, where the total energy of the system could be rewritten as:

$$E[n(\vec{r})] = T_0[n(\vec{r})] + V_{ne}[n(\vec{r})] + V_H[n(\vec{r})] + E_{XC}[n(\vec{r})] \tag{2.44}$$

where $T_0[n(\vec{r})]$ represents the kinetic energy of a non-interacting electron gas, having a density equal to that of the real system, and $E_{XC}[n(\vec{r})]$ indicates the exchange and correlation functional of an interacting system with density $n(\vec{r})$. Both the TF and the KS methods use the premise of a non-interacting electron gas, but the determination of kinetic energy differs, because the KS method considers the antisymmetric characteristic of the function. Thus, the wavefunction of the system is described through the representation of a Slater determinant. By the variational principle, both the energy and the electronic density of the ground state of the non-interacting auxiliary system can be obtained through eigenvectors $\phi_i(\vec{r})$ and eigenvalues ϵ_i of the monoelectronic HF equations. Thus, Kohn and Sham proposed to introduce monoelectronic orbitals, called KS orbitals ($\phi_i^{KS}(\vec{r})$), into DFT to effectively describe the kinetic energy term of a non-interacting system. Through these orbitals, the kinetic energy of the system can be calculated by

$$T_0[\rho(\vec{r})] = \sum_i^N \int \phi_i^{*KS}(\vec{r}) \left(\frac{-\nabla^2}{2}\right) \phi_i^{KS}(\vec{r}) d^3r \tag{2.45}$$

Since all $\phi_i^{KS}(\vec{r})$ are electron density functionals, Equation 2.45 is an explicit functional of the orbitals and an implicit one of the electron density, since the electron density unequivocally determines the KS orbitals. Of the other terms in Equation 2.44, the nuclear-electron interaction potential, $V_{ne}[n(\vec{r})]$, is given by

$$V_{ne}[n(\vec{r})] = \int \hat{V}_{ne} n(\vec{r}) d^3r = -\sum_{\alpha=1}^{M} \int \frac{Z_\alpha n(\vec{r})}{\left|\vec{R}_\alpha - \vec{r}\right|} d^3r \tag{2.46}$$

and $V_H[n(\vec{r})]$ is the Hartree potential calculated by

$$V_H[n(\vec{r})] = \frac{1}{2}\int \hat{V}_H n(\vec{r}) d^3r = \iint \frac{n(\vec{r}')n(\vec{r})}{|\vec{r}' - \vec{r}|} d^3r d^3r' \tag{2.47}$$

The Hartree potential is responsible for the classical electrostatic interaction between electrons, and should not be confused with the electron-electron interaction presented in the HK formalism of Equation 2.40, since $V_{ee}[n(\vec{r})]$ considers the contributions of $V_H[n(\vec{r})]$ and non-classical terms. The term $E_{XC}[n(\vec{r})]$ gets the name of exchange-correlation energy, and considers the exchange term, the correlation term, the kinetic energy correction term and the electrons self-interaction correction term.

$$E_{XC}[n(\vec{r})] = (T[n(\vec{r})] - T_0[n(\vec{r})]) + V_C[n(\vec{r})] + V_X[n(\vec{r})] \tag{2.48}$$

It is possible to minimize the energy functional again, to obtain the ground-state electronic density, by means of the Lagrange multipliers, with the link that the electronic density integral over all space is equal to the number of electrons in the system. Mathematically, this idea is represented by

$$\delta\left\{E[n(\vec{r})] - \mu\left[\int n(\vec{r}) d^3r - N\right]\right\} = 0 \tag{2.49}$$

where, μ is the Lagrange multiplier, and have the physical sense of the chemical potential of the system. So, the solution of the Equation. 2.49, leads to the equation called the KS equation

$$\left[-\frac{1}{2}\nabla_r^2 + \hat{V}_{eff}(\vec{r})\right]\phi_i^{KS}(\vec{r}) = \epsilon_i^{KS}\phi_i^{KS}(\vec{r}) \tag{2.50}$$

with $\hat{V}_{eff}(\vec{r})$ being the effective KS potential composed by Hartree potential, the electron-nucleus interaction and the exchange-correlation potential, with the exchange-correlation potential given by the first derivative of the exchange-correlation energy functional with respect to electron density

$$\hat{V}_{XC}(\vec{r}) = \frac{\delta E_{XC}[n(\vec{r})]}{\delta n(\vec{r})} \tag{2.51}$$

The KS equation is also transformed into a matrix equation based on the Roothaan method. Similar to the HF equation, a Kohn-Sham-Roothaan (KSR) equation is written as

$$\boldsymbol{FC_i = \varepsilon SC_i} \tag{2.52}$$

The $\boldsymbol{C_i}$ matrix is the coefficients matrix, whose elements are the weighting factors C_{pi} that determine to what extent each basis function ϕ (roughly, each atomic orbital on an atom) contributes to each MO $\boldsymbol{\phi}$. $\boldsymbol{S}$ matrix is the overlap matrix, whose elements are overlap integrals S_{ij} which are a measure of how well pairs of basis functions (roughly, atomic orbitals) overlap. The diagonal $\boldsymbol{\varepsilon}$ matrix is an energy-levels matrix, whose diagonal elements are MO energy levels $\boldsymbol{\phi}$, corresponding to the MOs ε_i. $\boldsymbol{F}$ is an energy-elements matrix, the Fock matrix, whose elements are

$$F_{pq} = h_{pq} + \sum_{r,s=1}^{n_{basis}} P_{rs}\langle pr|qs\rangle + (V_{XC})_{pq} \tag{2.53}$$

where

$$(V_{XC})_{pq} = \int d^3r \chi_p^*(r) V_{XC} \chi_q(\vec{r}) \tag{2.54}$$

The KS method is solved by the SCF method, since the effective KS potential depends on the electron density, which in turn depends on the KS orbitals. The SCF method is solved for nonlinear equations through the following steps: 1) provide an initial (trial) value for the electron density, $n^{(1)}(\vec{r})$, which allows to obtain the initial effective potential, $V_{eff}^{(1)}(\vec{r})$; 2) solve the KS equation with $n^{(1)}(\vec{r})$ and obtain single electron wave functions $\phi_i^{KS(1)}(\vec{r})$; 3) calculate the electron density based on the wavefunctions of a single electron and 4) From this moment on, a new electron density, $n^{(2)}(\vec{r})$, can be calculated using the new KS orbitals $\phi_i^{KS(2)}(\vec{r})$, and consequently, a new effective potential, $V_{eff}^{(2)}(\vec{r})$, can be determined. This procedure is applied repeatedly until a minimum condition of electronic density difference is found, or another convergence condition adopted is satisfied, such as the variation of the total energy.

Once the ground state electronic density is found, the total electronic energy of the system can be calculated using the eigenvalues of the KS equation, through:

$$E[n(\vec{r})] = \sum_{i=1}^{N} \epsilon_i^{KS} - \frac{1}{2}\iint \frac{n(\vec{r}')n(\vec{r})}{|\vec{r}' - \vec{r}|} d^3r d^3r' - \int \hat{V}_{XC}(\vec{r}) n(\vec{r}) d^3r + E_{XC}[n(\vec{r})] \tag{2.55}$$

The sum being made over all occupied orbitals and all N-KS orbitals obtained by the monoelectronic Schrodinger equation.

2.4.3 Exchange-correlation functional

The exchange-correlation functional is very important in the fundamentals of the KS method, because it is from these specific forms of functions that all observable properties of a quantum system are obtained exactly [89]. Thus, it becomes necessary the existence of an ideal functional, which describes all exchange and correlation interactions, however, this functional is far from being determined [89]. So, this is the only part of the KS method that is based on approximations, in which the known functionals are determined [89]. The physical properties obtained by known functionals depend directly on the class of approximations, which try to minimize errors in the description of exchange-correlation energy, as well as correct the kinetic energy of a non-interacting system and self-interaction [89]. Thus, the more efficient these approximations are, the better results will be obtained through DFT calculations.

2.4.3.1 Density Functional Approximations

The LDA is the simplest functional for exchange-correlation energy, which is based on an uniform electron gas (UEG) model as the basis of its foundation. UEG is a system of electrons with constant density everywhere. Thus, the of exchange-correlation energy can be written as

$$E_{XC}[n(\vec{r})] = \int n(\vec{r})\varepsilon_{XC}^{unif}[n(\vec{r})]d^3r \tag{2.56}$$

where $\varepsilon_{XC}^{unif}[n(\vec{r})]$ is the exchange-correlation energy per electron for an UEG. So, Kohn and Sham proposed, in the original paper on the density functional theory, the first approximations for $\varepsilon_{XC}^{unif}[n(\vec{r})]$ and that the energy density (non-homogeneous) is the energy (exchange plus correlation) by electron of a homogeneous electron gas

$$E_{XC}[n(\vec{r})] = \int n(\vec{r})\varepsilon_{X}^{unif}[n(\vec{r})]d^3r + \int n(\vec{r})\varepsilon_{C}^{unif}[n(\vec{r})]d^3r \tag{2.57}$$

The $\varepsilon_{X}^{unif}[n(\vec{r})]$ can be explicitly written with the exchange term being obtained by substituting the wave function that describes a non-interacting electron gas system in 2.15, resulting in

$$\varepsilon_X^{unif}[n(\vec{r})] = \frac{-3e^2 k_f}{4\pi} \tag{2.58}$$

The problem with this functional is in determining the correct value for the correlation part $\varepsilon_C^{unif}[n(\vec{r})]$, as there is no exact LDA correlation functional. As alternatives, several approximate LDA correlation functionals have been suggested, for example, in quantum chemistry, the Vosko–Wilk–Nusair (VWN) functional is widely used and is calculated based on Monte Carlo quantum methods of a gas of uniform density and in Padè's interpolation [108].

LDA tends to underestimate the exchange energy and overestimate the correlation energy by assuming that the density is the same everywhere [109]. Errors due to the exchange and correlation parts tend to compensate each other to some extent, caused by the fact that for any density the LDA satisfies a number of so-called sum rules [110, 111, 112]. To solve the problem of inhomogeneity in the real electron density of the electron, it is necessary to perform density expansions in terms of the gradient and higher order derivatives [112]. These expansions are called generalized gradient approximations (GGA) which consider not only the density at a position, but also the density gradient around that point [112]. Thus, the GGA functional has a semi-local character and the exchange-correlation energy is written as

$$E_{XC}[n(\vec{r})] = \int f\left[n(\vec{r}), \vec{\nabla} n(\vec{r})\right] d^3r \tag{2.59}$$

where the function f is an "exchange enhancement factor" that modifies the LDA expression according to the density variation in the neighborhoods of a considered point. Thus, several descriptions for the GGA f function have been proposed, among them we can highlight the introduction of the B88 functional proposed by Beck, and then the PW91 functional developed by Perdew and Wang, the first GGA functional used in large scale [113, 114, 115].

$$E_X^{B88}[n] = E_X^{LDA}[n] - \beta \sum_\sigma \int n_\sigma^{4/3} \frac{x_\sigma^2}{(1 + 6\beta x_\sigma sinh^{-1} x_\sigma)} d^3\vec{r} \tag{2.60}$$

where β is the only parameter with value equal to 0.0042.

$$E_C^{PW91}[n, s, t] = E_C^{PW-LDA}[n] + \int d^3r \, \rho H[n, s, t] \tag{2.61}$$

$$H[n,s,t] = \frac{\beta^2}{2\alpha}\ln\left[1+\frac{2\alpha}{\beta}\frac{t^2+At^4}{1+At^2+A^2t^4}\right] + C_{C_0}\left[C_1+\frac{C_2+C_3r_s+C_1r_s^2}{1+C_5r_s+C_6r_s^2+C_7r_s^3}-C_{C_1}\right]\times t^2 exp(-100s^2) \quad (2.62)$$

where coefficient A is

$$A = \frac{2\alpha}{\beta}\left[exp\left(\frac{-2\alpha\bar{E}_c^{PW-LDA}[n]}{\beta^2 n}\right)-1\right]^{-1} \quad (2.63)$$

and the dimensionless parameters s and t are

$$s = \frac{|\nabla n|}{2k_f\rho} \quad (2.64)$$

$$t = \frac{|\nabla n|}{2k_s n} \quad (2.65)$$

where $k_f = (3\pi^2 n)^{1/3}$ and $k_s = \left(4k_f/\pi\right)^{1/2}$. $\bar{E}_c^{PW-LDA}$ it is the integral core of the PW-LDA correlation functional. In the GGA term of this functional, there are 11 fundamental constants in total, which are determined to satisfy various exact exchange and correlation functional conditions, incorporate the inhomogeneity of the system and at the same time maintain the good characteristics of the LDA functional. However, several problems such as over-parameterization and the complicated form of E_{XC}, caused new GGA functionals to be proposed.

The GGA functional developed by Perdew, Burke and Ernzerhof (PBE) was the most efficient presented, as it is a simplification of the PW91 functional, where only the most favorable energetically satisfied conditions of the PW91 are maintained in the PBE, drastically reducing the parameters, from 11 to 2 [116]. The functional is written as

$$E_C^{PBE}[n,\zeta,t] = E_C^{PW-LDA}[n] + \int d^3r\, nH[n,\zeta,t] \quad (2.66)$$

$$H[n,\zeta,t] = \gamma\phi^3\ln\left[1+\frac{\beta}{\gamma}t'^2\left(\frac{1+At'^2}{1+At'^2+A^2t'^4}\right)\right] \quad (2.67)$$

$$A = \frac{\beta}{\gamma}\left[exp\left(-\frac{\bar{E}_c^{PW-LDA}[n]}{\gamma\phi^2 n}\right) - 1\right]^{-1} \quad (2.68)$$

$$\phi = \frac{1}{2}\left[(1+\zeta)^{2/3} + (1-\zeta)^{2/3}\right] \quad (2.69)$$

where $\gamma = (1 - \ln 2)/\pi^2 = 0.031091$, $\beta = 0.066725$ e $\zeta = n_\alpha - n_\beta / n_\alpha + n_\beta$.

2.4.3.2 Hybrid functionals

The hybrid functionals, so called because they contain an additional part of exact exchange energy, were created to improve the description of the physical properties of a system such as bond length, ionization energy, vibrational frequencies, among others [89]. Hybrid functionals connect the HF exchange integral with the GGA exchange functionals at a constant ratio, based on the concepts of adiabatic connection, which causes the KS energies of the independent electron model to bond with those of the fully interactive electron

$$E_X = \int_0^1 d\lambda E_X^\lambda \approx E_X^{GGA} + \lambda(E_X^{HF} - E_X^{GGA}) \quad (2.70)$$

Hybrid functional term should be understood from the ansatz that the exact energy exchange is situated between the GGA energy exchange functional and the HF exchange integral, and not as the combination of the HF exchange integral with exchange functionals [89].

The hybrid functional B3LYP, the first proposed hybrid functional, is the most frequently used functional among in all functionals in quantum chemistry calculations and has reasonable accuracy at affordable computational costs [117, 118]. This functional use three parameters such as the mixing ratios to form the adiabatic connections between a fixed global fraction 20% HF exchange integral, and the LDA exchange functional and between the LYP-GGA correlation functional and the LDA correlation functional, and to match the GGA attenuated term of the B88 exchange functional

$$E_{XC}^{B3LYP} = E_{XC}^{LDA} + a_1(E_X^{HF} - E_X^{LDA}) + a_2\Delta E_X^{B88} + a_3(E_C^{LYP} - E_C^{VWN-LDA}) \quad (2.71)$$

The LYP correlation functional is derived from the Colle-Salvetti energy correlation functional and is a key component of the B3LYP functional, providing very accurate correlation

energies in molecular property calculations [119]. In this functional, five semi-empirical parameters, $a = 0.04918$, $b = 0.7628$, $c = 0.58$, $d = 0.8$ and $q = 2.29$ are contained, without fundamental constant, and is written as

$$E_c^{LYP}[n, \nabla n, \nabla^2 n] = -\int d^3r \frac{a}{1 + dn^{-1/3}} \Big\{ n + bn^{-2/3} \left[C_F n^{5/3} - 2t_W + \frac{1}{9}\left(t_W + \frac{1}{2}\nabla^2 n \right) \right] exp\left(-cn^{-1/3}\right) \Big\} \tag{2.72}$$

where

$$\beta = qp^{1/3} \tag{2.73}$$

$$t_W = \frac{1}{8}\left(\frac{|\nabla\rho|^2}{\rho} - \nabla^2 n \right) \tag{2.74}$$

$$C_f = \frac{3}{10}(3\pi^2)^{2/3} \tag{2.75}$$

As shown, the hybrid functionals contain the HF exchange integral, which is not formulated from the electron density, so it is not strictly correct to use the hybrid functionals within the framework of the KS method, which depends on formulated functionals from the electronic density. However, Levy et al. solved this problem by extending the restricted search formulation to the one using functionals containing the HF exchange integral and suggested the generalized KS method as an extension of the KS method [120, 121].

As exchange energy contributions are generally much higher than the correlation ones, the non-Coulomb part of exchange functionals, typically decreases very quickly in relation to distance, becoming imprecise at large distances, and inappropriate for calculate some properties such as binding energies van der Waals, electronic excitation spectra, optical response properties and orbital energies [122]. Thus, it is necessary to consider several types of corrections in the exchange functionals to improve the description of the physical properties of a quantum system. Then, range-separated hybrid functionals developed a correction in which the exchange interactions are divided into short-range (SR) and long-range (LR) parts, and then a general exchange functional and the HF exchange integral are adopted in the short-range

calculations and long range, respectively. The separation of the SR and LR term is given through the general function

$$\frac{1}{r_{12}} = \frac{1 - \text{erf}(\omega r_{12})}{r_{12}} + \frac{\text{erf}(\omega r_{12})}{r_{12}} \tag{2.76}$$

where $\text{erf}(\omega r_{12})$ is the error function, and the first term refers to the LR and the second to the SR, and the value of ω delimits the interface between the SR and LR terms.

For instance, the CAM-B3LYP functional is a LR corrected functional hybrid that uses the Coulomb-attenuating method (CAM) [123], using

$$\frac{1}{r_{12}} = \frac{1 - [\alpha + \beta \cdot \text{erf}(\omega r_{12})]}{r_{12}} + \frac{\alpha + \beta \cdot \text{erf}(\omega r_{12})}{r_{12}} \tag{2.77}$$

as a replacement for Equation 2.76 to perform the LR correction for the B3LYP hybrid functional. The exchange functional is a mix of exact exchange, i.e., inclusion of the LR HF exchange integral at a constant ratio, and SR DFT exchange, but unlike B3LYP, the exact exchange ratio to DFT varies in different regions of the molecule. The degree of mixing of exact exchange and DFT is controlled by the α and β parameters, whose values used are 0.19 and 0.46 for α and β, respectively. Specifically, the SR part of the exchange interaction is incorporated by modifying the usual exchange functional form

$$E_X^{SR} = -\frac{1}{2}\sum_{\sigma} \int n_\sigma^{4/3} K_\sigma \times \left\{1 - \frac{8}{3} a_\sigma \left[\sqrt{\pi} erf\left(\frac{1}{2a_\sigma}\right) + 2a_\sigma (b_\sigma - c_\sigma)\right]\right\} d^3\vec{r} \tag{2.78}$$

where a_σ, b_σ e c_σ are

$$a_\sigma = \frac{\mu K_\sigma^{1/2}}{6\sqrt{\pi} n_\sigma^{1/3}} \tag{2.79}$$

$$b_\sigma = exp\left(-\frac{1}{4a_\sigma^2}\right) - 1 \tag{2.80}$$

$$c_\sigma = 2a_\sigma^2 b_\sigma + \frac{1}{2} \tag{2.81}$$

The LR part of the exchange interaction is expressed with the HF exchange integral

$$E_X^{LR-HF} = -\frac{1}{2}\sum_{\sigma}\sum_{i}^{occ}\sum_{j}^{occ}\int\int \psi_{i\sigma}^{*}(\vec{r}_1)\psi_{j\sigma}^{*}(\vec{r}_1) \times \frac{\mathrm{erf}(\omega r_{12})}{r_{12}}\psi_{i\sigma}(\vec{r}_2)\psi_{j\sigma}(\vec{r}_2)\, d^3\vec{r}_1 d^3\vec{r}_2 \tag{2.82}$$

where $\psi_{i\sigma}$ is the i-th molecular σ-spin orbital. The correlation functional uses 20% of the VWN LDA parameterization along with 80% of the LYP GGA functional, similarly to the B3LYP functional.

In empirical functionals, LR correction has also been applied and often produces more accurate results for properties, including atomization energies, than the originals in reference set calculations [124, 125]. The first significant advance was made by Becke with the B97 functional, proposing the expansion of $E_{XC}[n(\vec{r})]$ using a power series expansion involving only the local spin density and its first derivative, in addition to a small fraction of the HF exchange [126]. The linear coefficients in the expansions are optimized from a systematic adjustment procedure to a set of reliable experimental data, called the training set. The first LR corrected semi-empirical functional is the ωB97X functional in the form [124],

$$E_{XC}^{\omega B97X} = E_X^{LR-HF} + c_X E_X^{SR-HF} + E_X^{SR-B97} + E_C^{B97} \tag{2.83}$$

where

$$E_X^{SR-HF} = -\frac{1}{2}\sum_{\sigma}\sum_{i}^{occ}\sum_{j}^{occ}\int\int \psi_{i\sigma}^{*}(\vec{r}_1)\psi_{j\sigma}^{*}(\vec{r}_1) \times \frac{\mathrm{erfc}(\omega r_{12})}{r_{12}}\psi_{i\sigma}(\vec{r}_2)\psi_{j\sigma}(\vec{r}_2)\, d^3\vec{r}_1 d^3\vec{r}_2 \tag{2.84}$$

$$E_X^{SR-B97} = \sum_{\sigma}\int e_{x\sigma}^{SR-LSDA}(n_\sigma) g_{x\sigma}(s_\sigma^2) d\vec{r} \tag{2.85}$$

$$E_c^{B97} = \sum_{\sigma} E_{c\sigma\sigma}^{B97} + E_{c\alpha\beta}^{B97} \tag{2.86}$$

where $g_{x\sigma}(s_\sigma^2)$ is a dimensionless inhomogeneity correction factor depending on the dimensionless reduced rotation density gradient $s_\sigma = |\nabla n_\sigma|/n_\sigma^{4/3}$, and the B97 functional is divided into components $E_{c\sigma\sigma}^{B97}$ of the same spin and $E_{c\alpha\beta}^{B97}$ of opposite spin. The equations for

each term can be found in the original articles. The ωB97X functional includes a 16% fraction of SR exact exchange, with the "X" representing the use of SR HF exchange. This functional contains many 17 semi-empirical parameters and produces more accurate results for physical properties. The ωB97X-D functional is a van der Waals correction for the ωB97X functional, in which a parameterized classical dispersion term is combined, and includes 100% LR exact exchange, 22% SR exact exchange, a modified B97 exchange density for SR interaction and a B97 correlation density function [125]

$$E_{XC}^{\omega B97XD} = E_X^{LR-HF} + c_X E_X^{SR-HF} + E_X^{SR-B97} + E_C^{B97} + E_{disp} \tag{2.87}$$

$$E_{disp} = -\sum_{i=1}^{N_{at}-1} \sum_{j=i+1}^{N_{at}} \frac{C_6^{ij}}{R_{ij}^6} f_{damp}(R_{ij}) \tag{2.88}$$

where c_X is a fractional number to be determined, N_{at} is the number of atoms in the system, C_6^{ij} is the dispersion coefficient for the atom pair ij, R_{ij} is an interatomic distance and f_{damp} is the damping function

$$f_{damp}(R_{ij}) = \frac{1}{1 + a(R_{ij}/R_r)^{-12}} \tag{2.89}$$

where, R_r is the sum of the van der Waals radii of a pair of atoms ij, and the only nonlinear parameter a, which controls the strength of the dispersion corrections.

2.4.4 Time-Dependent Kohn–Sham Method

When electrons are under the influence of a generic time-dependent potential, $V_{ext}(\vec{r}, t)$, the electronic Hamiltonian of system, $\widehat{H}_e(\vec{r}, t)$, also becomes time-dependent and describes a variety of physical and chemical situations, including atoms, molecules and solids, in arbitrary time-dependent electric or magnetic fields, scattering experiments, etc [127]. Thus, the time-dependent density functional theory (TD-DFT) extends the basic ideas of the stationary ground state of DFT to the treatment of more general time-dependent excitations or phenomena. TD-DFT can be seen as an alternative formulation of time-dependent quantum mechanics, its basic variable is the electron density of system, $n(\vec{r}, t)$ [127].

2.4.4.1 Runge-Gross theorem

With the HK theorems being the basis of DFT, for the description of periodically time-dependent electronic states, Runge and Gross proposed the Runge-Gross (RG) theorem, as a time-dependent generalization of the HK theorems [128]. The RG theorem establishes a correspondence between the time-dependent densities $n(\vec{r},t)$ and the time-dependent potentials $V_{ext}(\vec{r},t)$ for a given initial state [128].

A given evolution of electron density can be generated by, at most, a potential as a function of time. Thus, if two systems evolve from the same initial state $|\Psi_0\rangle = |\Psi_0(t_0)\rangle$, but submitted to two distinct potentials $V_{ext}(\vec{r},t)$ and $V'_{ext}(\vec{r},t)$, their respective densities, $n(\vec{r},t)$ and $n'(\vec{r},t)$, will be different from each other. Such a statement is valid if we consider that the potentials differ from each other by more than a function of time,

$$V(\vec{r},t) \neq V'(\vec{r},t) + C(t) \tag{2.90}$$

for $t > t_0$. Thus, $V_{ext}(\vec{r},t)$ can be expanded in Taylor series in terms of the initial time t_0, and defining that the transformation $V_{ext}(r,t) \rightarrow n(\vec{r},t)$ corresponds to the resolution of the time-dependent Schrödinger equation [129], so

$$V(\vec{r},t) \overset{1:1}{\underset{\Psi_0 \ ct}{\longleftrightarrow}} n(\vec{r},t) \tag{2.91}$$

If $V(\vec{r},t) \neq V'(\vec{r},t) + C(t)$, then the current densities $\vec{j}$ and $\vec{j}'$, generated by $V(\vec{r},t)$ and $V'(\vec{r},t)$, are also different. The current density $\vec{j}$ can be written as the expected value of the current density operator

$$\vec{j}(\vec{r},t) = \langle \Psi(t)|\hat{j}(\vec{r})|\Psi(t)\rangle \tag{2.92}$$

where the operator $\hat{j}(\vec{r})$ is given by

$$\hat{j}(\vec{r}) = -\frac{1}{2i}\left\{\left[\nabla\hat{\Psi}^*(\vec{r})\right]\hat{\Psi}(\vec{r}) - \hat{\Psi}^*(\vec{r})\left[\nabla\hat{\Psi}(\vec{r})\right]\right\} \tag{2.93}$$

Using the quantum-mechanics equation of motion, which is valid for any operator, $\hat{O}(t)$,

$$i\frac{d}{dt}\langle\Psi(t)|\hat{O}(t)|\Psi(t)\rangle = \left\langle\Psi(t)\left|i\frac{\partial}{\partial t}\hat{O}(t) + \left[\hat{O}(t),\hat{H}(t)\right]\right|\Psi(t)\right\rangle \tag{2.94}$$

to write the equations of motion for the current densities $\vec{j}$ and $\vec{j}'$,

$$i\frac{d}{dt}\hat{\jmath}(\vec{r},t) = \langle\Psi(t)|\left[\hat{\jmath}(\vec{r}),\widehat{H}(t)\right]|\Psi(t)\rangle \tag{2.95}$$

$$i\frac{d}{dt}\hat{\jmath}'(\vec{r},t) = \langle\Psi'(t)|\left[\hat{\jmath}(\vec{r}),\widehat{H}'(t)\right]|\Psi'(t)\rangle \tag{2.96}$$

Since it starts from a fixed state, at t_0 the wave functions, current densities and current densities between systems and prime systems

$$|\Psi(t_0)\rangle \equiv |\Psi'(t_0)\rangle \equiv |\Psi_0\rangle \tag{2.97}$$

$$n(\vec{r},t_0) = n'(\vec{r},t_0) \equiv n_0 \tag{2.98}$$

$$\vec{\jmath}(\vec{r},t_0) = \vec{\jmath}'(\vec{r},t_0) \equiv \overrightarrow{J_0} \tag{2.99}$$

Taking the difference between Equations 2.95 and 2.96, we obtain, when $t = t_0$

$$\frac{d}{dt}[\vec{\jmath}(\vec{r},t) - \vec{\jmath}'(\vec{r},t)]_{t=t_0} = n_0(\vec{r})\nabla[V(\vec{r},t_0) - V'(\vec{r},t_0)] \tag{2.100}$$

As the external potentials are constrained and expandable in Taylor series with respect to the time coordinate around the initial moment t_0, we obtain

$$V(\vec{r},t) = \sum_{k=0}^{\infty} c_k(\vec{r})(t-t_0)^k \tag{2.101}$$

where the coefficients $c_k(\vec{r})$ are given by

$$c_k(\vec{r}) = \frac{1}{k!}\frac{\partial^k}{\partial t^k}V(\vec{r},t)|_{t=t_0} \tag{2.102}$$

In addition, the function $u_k(\vec{r})$ is define

$$u_k(\vec{r}) = \frac{1}{k!}\frac{\partial^k}{\partial t^k}[V(\vec{r},t_0) - V'(\vec{r},t_0)]|_{t=t_0} \tag{2.103}$$

If the difference between the two potentials is more than a purely time-dependent function, at least one of the expansion coefficients in Taylor expansion around t_0 will differ by more than one constant

$$\exists_{k\geq 0}: u_k(\vec{r}) \neq constant \tag{2.104}$$

If the above condition is satisfied from $k = 0$, that is, the two potentials, $V(\vec{r}, t)$ and $V'(\vec{r}, t)$, differ since t_0. This implies that the left-hand derivative in the equation x is nonzero, since $\nabla[V(\vec{r}, t_0) - V'(\vec{r}, t_0)] \neq 0$. The two current densities $\vec{j}$ and $\vec{j}'$, will therefore be different for $t > t_0$. If k is much higher than zero, the equation of motion is applied $k + 1$ times producing the result

$$\frac{d^{k+1}}{dt^{k+1}}\{\vec{j}(\vec{r}, t) - \vec{j}'(\vec{r}, t)\}|_{t=t_0} = n_0(\vec{r})\nabla u_k(\vec{r}) \tag{2.105}$$

The right member of the above equation is nonzero, which again implies that $\vec{j}(\vec{r}, t) \neq \vec{j}'(\vec{r}, t)$ for $t > t_0$. From the continuity equation,

$$\frac{\partial}{\partial t} n(\vec{r}, t) = -\nabla \vec{j}(\vec{r}, t) \tag{2.106}$$

If the above equation is written for the system and prime system and take the difference between them,

$$\frac{\partial}{\partial t}\{n(\vec{r}, t) - n'(\vec{r}, t)\} = -\nabla\{\vec{j}(\vec{r}, t) - \vec{j}'(\vec{r}, t)\} \tag{2.107}$$

With the expression involving the k-th derivative of the external potential. Taking $(k + 1)$ times in the time derivative in the equation above,

$$\frac{d^{k+2}}{dt^{k+2}}\{n(\vec{r}, t) - n'(\vec{r}, t)\}|_{t=t_0} = -\nabla \frac{d^{k+1}}{dt^{k+1}}\{\vec{j}(\vec{r}, t) - \vec{j}'(\vec{r}, t)\}|_{t=t_0} \tag{2.108}$$

substituting the expression y,

$$\frac{d^{k+2}}{dt^{k+2}}\{n(\vec{r}, t) - n'(\vec{r}, t)\}|_{t=t_0} = -\nabla\{n_0(\vec{r})\nabla u_k(\vec{r})\} \tag{2.109}$$

by the restriction of $u_k(\vec{r}) \neq constant$,

$$\nabla\{n_0(\vec{r})\nabla u_k(\vec{r})\} \neq 0 \tag{2.110}$$

therefore, $n(\vec{r}, t) \neq n'(\vec{r}, t)$. Thus, from the proof, the Runge-Gross theorem is then the analogue of the Hohenberg-Kohn theorem for the time-dependent system [128].

2.4.4.2 Time-dependent Kohn-Sham Equations

The formalism developed by KS has been successful in determining the fundamental state properties in DFT. Therefore, trying to generalize them is the first step towards obtaining the desired properties. As mentioned in the previous subsection, the RG theorem broadly restates that any observable can be calculated if the electron density is known. However, is not told how to calculate this quantity, so, similarly to the Section 2.3.2, a generalization of the KS equations is searched to give all the information about the system. In the time-dependent case, the natural extension of the KS equation has the following form

$$\left[-\frac{1}{2}\nabla_{\vec{r}}^2 + \hat{V}_{eff}(\vec{r},t)\right]\phi_i(\vec{r},t) = i\frac{\partial}{\partial t}\phi_i(\vec{r},t) \tag{2.111}$$

where $\hat{V}_{eff}(\vec{r},t)$ is given by

$$\hat{V}_{eff}[r,t;\rho(r,t)] = V_{ext}[r,t] + \int d^3r \frac{\rho(r',t)}{|r-r'|} - \frac{\delta S_{XC}[\rho]}{\delta\rho(r,t)} \tag{2.112}$$

The Equation 2.111 using the effective potential in Equation 2.112 is called the time-dependent Kohn-Sham (TD-KS) equation [128].

In DFT, $V_{XC}[\rho]$ is normally written as a derivative of the exchange-correlation energy, as can be seen in Equation 2.51. This result was obtained via total energy minimization, but in the case of TD-DFT this is no longer true [127]. In time-dependent systems, total energy is not a conserved quantity, so there is no variational principle. However, there is the action, a quantity analogous to energy, defined as

$$S = \int_{t_0}^{t_1} dt\phi(t)\left(i\frac{\partial}{\partial t} - \hat{H}\right)\phi(t) \tag{2.113}$$

and is representable as a density functional, $S[\rho]$, and can be decomposed into

$$S[\rho] = \int_{t_0}^{t_1} dt\phi^*(t)\left[i\frac{\partial}{\partial t} - \left(\hat{T} + \hat{V}_{ee}\right)\right]\phi(t) - \int_{t_0}^{t_1} dt \int_{t_0}^{t_1} d^3r\rho(r,t)V_{ext}(r,t) \tag{2.114}$$

Two properties of $S[\rho]$ are obtained: (i) when performing the functional derivative of the action with respect to $\phi^*(t)$ and equaling it to zero, the time-dependent Schrödinger equation is obtained. Thus, the function $\phi(t)$ that makes the action stationary will be the time-dependent solution of the Schrödinger equation. It should be noted that here there is no

"minimum principle", as in the case of DFT, but rather a "stationary principle". (ii) At the solution point, always have $S[\rho] = 0$.

Van Leeuwen using the Keldish formalism, defined a new action that would circumvent the causal problems contained in the theory. So, with the new action, the potential for exchange and correlation could be found [127]. The form of this potential is as follows

$$\frac{\delta S_{XC}[\rho]}{\delta \rho(r,t)} \approx V_{XC}[\rho](r,t) = \frac{\delta E_{XC}[\rho]}{\delta \rho(r,t)} \tag{2.115}$$

where S_{XC} is the exchange-correlation part of the action integral and is approximated based on the BO approximation.

Applying the TD-KS equation to linear response theory, excitation energies can be calculated and assigned to corresponding transitions [130]. Following the RG theorem, it is assumed that only a weak perturbation, δV_{ext}, is added to the external potential. Under this assumption, it is interpreted that the electron density also undergoes an infinitesimal change, $\delta\rho(r,t)$, in the stationary part, ρ_{stat} [130]. The exchange-correlation potential, V_{XC}, is, therefore, represented as

$$V_{XC}[\rho](r_1,t_1) = V_{XC}^{stat}[\rho](r_1) + \iint dt_2 d^3r_2 f_{XC}[\rho_{stat}]\,(r_1,r_2,t_2-t_1)\delta\rho(r_2,t_2) \tag{2.116}$$

$$f_{XC}[\rho_{stat}](r_1,r_2,t_2-t_1) = \left.\frac{\delta V_{XC}(r_1,t_1)}{\delta\rho(r_2,t_2)}\right|_{\rho=\rho_{stat}} \tag{2.117}$$

The derivative of the exchange-correlation potential in terms of electron density, f_{XC}, is called the exchange correlation-integral kernel. Define the response function of the electron density, χ_{KS}, for the infinitesimal change in KS potential, δV_{KS}, as

$$\delta\rho(r_1,t_1) = \iint dt_2 d^3r_2 \chi_{KS}[\rho_{stat}]\,(r_1,r_2,t_2-t_1)\delta V_{KS}(r_2,t_2) \tag{2.118}$$

In this definition, the response function is given by Green function theory as

$$\begin{aligned}\chi_{KS}(r_1,r_2,\omega) = 2\lim_{\eta\to 0+}\sum_{i}^{n_{occ}}\sum_{a}^{n_{vir}}\Bigg[&\frac{\phi_i^*(r_1)\phi_a(r_1)\phi_i(r_2)\phi_a^*(r_2)}{\omega-(\epsilon_a-\epsilon_i)+i\eta}\\ &-\frac{\phi_i(r_1)\phi_a^*(r_1)\phi_i^*(r_2)\phi_a(r_2)}{\omega-(\epsilon_a-\epsilon_i)+i\eta}\Bigg]\end{aligned} \tag{2.119}$$

Note that this response function is Fourier-transformed $(t \to \omega)$. What is important is that this response function has poles in the excitation energies. Casida proposed that the pole energies of the response function in Equation 2.119, i.e., excitation energies, can be calculated by solving the following simultaneous matrix equations [131]:

$$\sum_{jb\tau}\left[\delta_{\sigma\tau}\delta_{ij}\delta_{ab}(\epsilon_{a\sigma}+\epsilon_{i\sigma}+\omega)+K_{ia,jb}^{\sigma\tau}\right]X_{jb}^{\tau}+K_{ia,jb}^{\sigma\tau}X_{jb}^{\tau}=0 \tag{2.120}$$

and

$$\sum_{jb\tau}\left[\delta_{\sigma\tau}\delta_{ij}\delta_{ab}(\epsilon_{a\sigma}-\epsilon_{i\sigma}+\omega)+K_{ai,bj}^{\sigma\tau}\right]X_{bj}^{\tau}+K_{ai,jb}^{\sigma\tau}X_{jb}^{\tau}=0 \tag{2.121}$$

In these equations, the spins of the orbitals $(\sigma,\tau,\sigma'\neq\sigma)$ are explicitly displayed for purposes of accuracy. The simultaneous matrix equations are also represented for singlet and triplet excitations as follows

$$\Omega\boldsymbol{F}_{ia\sigma}=\omega_{ia}^{2}\boldsymbol{F}_{ia\sigma} \tag{2.122}$$

$$\begin{aligned}\Omega_{ia\sigma,jb\tau}^{singlet}=\;&\delta_{\sigma\tau}\delta_{ij}\delta_{ab}(\epsilon_{a\sigma}-\epsilon_{i\sigma})^{2}\\&+2(\epsilon_{a\sigma}-\epsilon_{i\sigma})^{1/2}\left(K_{ia,jb}^{\sigma\sigma}+K_{ia,jb}^{\sigma\sigma'}\right)\left(\epsilon_{b\tau}-\epsilon_{j\tau}\right)^{1/2}\end{aligned} \tag{2.123}$$

and

$$\begin{aligned}\Omega_{ia\sigma,jb\tau}^{triplet}=\;&\delta_{\sigma\tau}\delta_{ij}\delta_{ab}(\epsilon_{a\tau}-\epsilon_{i\tau})^{2}\\&+2(\epsilon_{a\sigma}-\epsilon_{i\sigma})^{1/2}\left(K_{ia,jb}^{\sigma\sigma}+K_{ia,jb}^{\sigma\sigma'}\right)\left(\epsilon_{b\tau}-\epsilon_{j\tau}\right)^{1/2}\end{aligned} \tag{2.124}$$

where $F_{ia\sigma}$ is the response coefficient matrix given by

$$F_{ia\sigma}=(\epsilon_{a\sigma}-\epsilon_{i\sigma})^{-1/2}(\chi_{ia\sigma}-\chi_{ai\sigma}) \tag{2.125}$$

$$\chi_{ia\sigma}(\omega)=\frac{-1}{\omega+(\epsilon_{a\sigma}-\epsilon_{i\sigma})}\times\int d^{3}r\phi_{i\sigma}^{*}(r)\,\delta\left(2\sum_{j}^{n}\hat{J}_{i}+V_{XC}\right)(r,\omega)\phi_{a\sigma}(r) \tag{2.126}$$

ϵ_i is the i -th orbital energy, and $K_{ia,jb}^{\sigma\tau}$ is provided as

$$K_{ia,jb}^{\sigma\tau} = \langle ib|aj\rangle^{\sigma\tau} + \iint d^3r_1 d^3r_2 \phi_{i\sigma}^*(r_1)\phi_{b\tau}^*(r_2) f_{XC}(r_1, r_2)\phi_{a\sigma}(r_1)\phi_{j\tau}(r_2) \qquad (2.127)$$

2.4.5 Orbital Energy

2.4.5.1 Koopmans' Theorem

Ionization energies (IE) and electron affinities (EA) can be calculated simply as the energy difference between the neutral and the ion [132]. In HF theory, approximate IEs can be obtained by applying Koopmans' theorem which says that the energy required to remove an electron from an orbital is the negative of the orbital energy [132]. Thus, the IE of a molecule is approximately the negative of the energy of its HOMO. The proof assumes that the orbitals of the neutral system and those of the resulting ionized system with an electron removed are the same, and that there is no relaxation of the orbitals of the latter. For orbital ϕ_i, the orbital energy of the HF equation is represented by

$$\epsilon_i = \int d^3r \phi_i^*(\vec{r})\, \hat{F}\phi_i(\vec{r}) = h_i + \sum_j^n \left(2J_{ij} - K_{ij}\right) \qquad (2.128)$$

where h_i, J_{ij} and $K_{ij}$are the one-electron and two-electron integrals, and in this case, the total energy is provided as

$$E_0 = \sum_i^n h_i + \sum_{i<j}^n \left(2J_{ij} - K_{ij}\right) = \sum_i^n \epsilon_i - \sum_{i<j}^n \left(2J_{ij} - K_{ij}\right) \qquad (2.129)$$

Moreover, the energy after removing one electron from orbital ϕ_i derived as

$$IP = E' - E_0 = -h_i - \sum_j^n \left(2J_{ij} - K_{ij}\right) = -\epsilon_i \qquad (2.130)$$

This indicates that the occupied orbital energies are the corresponding negative of the ionization potentials (IP) [132]. The Koopmans' theorem is also established for unoccupied orbitals, being the unoccupied orbital energies are the corresponding negative of the electron affinities [132]. Considering the energy after adding one electron to an unoccupied orbital as

$$E'' = E_0 + h_a + \sum_j^n (2J_{aj} - K_{aj}) \tag{2.131}$$

Therefore, the electron affinity, which is the energy difference from E'' to E_0, is proven to be

$$EA = E_0 - E' = -h_a - \sum_j^n (2J_{aj} - K_{aj}) = -\epsilon_a \tag{2.132}$$

2.4.5.2 Janak's Theorem

In analogy to HF theory, and according to Koopmans' theorem, the variation in the total energy of a molecule in relation to occupancy coincides with the HF eigenvalue of its spin-orbital ϕ_i. Regardless of the detailed form of the exchange-correlation functional, it happens in parallel for the DFT theory due to the Janak's theorem [133]. With Janak's theorem, the possibility of describing the energies of excited states also takes shape according to the DFT formalism. Strictly speaking, DFT theory is applicable to the ground state of a system and a situation in which the occupancy number of one (or some) of the states is modified by an infinitesimal amount, which is not necessarily a ground state. The generalization due to Janak's theorem consists in the introduction of occupation numbers of the $\{n_i\}$ orbitals for each state. The n_i are allowed occupancy numbers with $0 \leq n_i \leq 1$. Fractionally occupied KS orbitals arise naturally in the ground state formalism when the highest occupied level degenerates. By showing the occupancy numbers of the orbitals, the KS equation is written as

$$\left(-\frac{1}{2}\nabla^2 + V_{ext} + 2\sum_i^n \hat{J}_i + V_{XC}\right)\phi_i = \epsilon_i \phi_i \tag{2.133}$$

The functional of total electronic energy E corresponds

$$E = T + E_{ext}[\rho] + J[\rho] + E_{XC}[\rho] \tag{2.134}$$

where T, E_{ext} and J are the kinetic energies, external field and Coulomb interaction, respectively, which are given by

$$T = \sum_i^n \int \phi_i^*(\vec{r}) \left(\frac{-\nabla^2}{2}\right) \phi_i(\vec{r}) d^3r = \sum_i n_i t_i \tag{2.135}$$

$$E_{ext}[\rho] = \int \rho\,(\vec{r}) V_{ext} d^3r \tag{2.136}$$

$$J[\rho] = \frac{1}{2}\int \frac{\rho(\vec{r}_1)\rho(\vec{r}_2)}{r_{12}} d^3r_1 d^3r_2 \tag{2.137}$$

In this case, the electron density, ρ, is represented by

$$\rho = \sum_i^n n_i |\phi_i|^2 \tag{2.138}$$

The variation of electronic energy E in terms of the occupation number is, therefore, given by

$$\frac{\partial E}{\partial n_i} = \frac{\partial T}{\partial n_i} + \frac{\partial (E_{ext} + J + E_{XC})}{\partial n_i} \cdot \frac{\partial \rho}{\partial n_i} \tag{2.139}$$

$$\frac{\partial E}{\partial n_i} = t_i + 2\sum_j^n n_j \frac{\partial t_j}{\partial n_i} + \int \left(2\sum_j^n \hat{J}_j + V_{XC}\right) \cdot \left(|\phi_i|^2 + \sum_j^n n_j + \frac{\partial |\phi_j|^2}{\partial n_i}\right) d^3r \tag{2.140}$$

Since using Equations 2.133 and 2.135,

$$t_i = \epsilon_i - \int \left(2\sum_j^n \hat{J}_j + V_{XC}\right) |\phi_i|^2 d^3r \tag{2.141}$$

is provided, substituting this into Equation 2.140 leads to

$$\frac{\partial E}{\partial n_i} = \epsilon_i + \sum_j^n n_j \left[\frac{\partial t_j}{\partial n_i} + \int \left(2\sum_j^n \hat{J}_j + V_{XC}\right) \frac{\partial |\phi_j|^2}{\partial n_i} d^3r\right] \tag{2.142}$$

By substituting

$$\frac{\partial t_j}{\partial n_i} = \int \frac{\partial \phi_j^*}{\partial n_i} \left(\frac{-\nabla^2}{2}\right) \phi_j d^3r + \int \phi_j^* \left(\frac{-\nabla^2}{2}\right) \frac{\partial \phi_j^*}{\partial n_i} d^3r \tag{2.143}$$

from Equation 2.135 into Equation 2.140, the energy derivative in terms of the occupation number is derived for an arbitrary orbital ϕ_i as

$$\frac{\partial E}{\partial n_i} = \epsilon_i + \sum_j^n n_j \left[\frac{\partial \phi_j^*}{\partial n_i} \left(\frac{-\nabla^2}{2} + 2\sum_j^n \hat{J}_j + V_{XC} \right) \phi_j d^3r + \phi_j^* \left(\frac{-\nabla^2}{2} + 2\sum_j^n \hat{J}_j + V_{XC} \right) \frac{\partial \phi_j}{\partial n_i} d^3r \right] \tag{2.144}$$

$$\frac{\partial E}{\partial n_i} = \epsilon_i + \sum_j^n n_j \, \epsilon_j \left[\int \frac{\partial}{\partial n_i} |\phi_i|^2 d^3r \right] \tag{2.145}$$

$$\frac{\partial E}{\partial n_i} = \epsilon_i + \sum_j^n n_j \, \epsilon_j \left[\frac{\partial}{\partial n_i} \int |\phi_i|^2 d^3r \right] = \epsilon_i \tag{2.146}$$

Therefore, the relationship between the total electronic energy and orbital energy is proven to be

$$\frac{\partial E}{\partial n_i} = \epsilon_i \tag{2.147}$$

This equation indicates that the derivative of the total electronic energy in relation to the occupancy number of an orbital is identical to the orbital energy, this is called Janak's theorem, and from it is observed that only the highest occupied (HO) orbital can be fractionally, and that all orbitals with $\epsilon_i < \epsilon_{HO}$ must have full occupancy [133]. The energy linearity theorem for fractional occupations proves that the total electronic energy varies linearly as a function of its fractional occupation number, that is,

$$E\left(n + \frac{p}{q}\right) = \frac{p}{q} E(n+1) + \frac{q-p}{q} E(n) \tag{2.148}$$

and combined with Janak's theorem, the physical meaning of the orbital energies is obtained [134]. Figure 5 clearly indicates that if the total electron energy meets the energy linearity theorem, it is proved by Janak's theorem that the HOMO and LUMO energies are identical to the corresponding negative of the ionization potential and the electron affinity, respectively [134].

Figure 5. Schematic diagram of total electronic energy as a function of fractional occupation number variation, Δn.

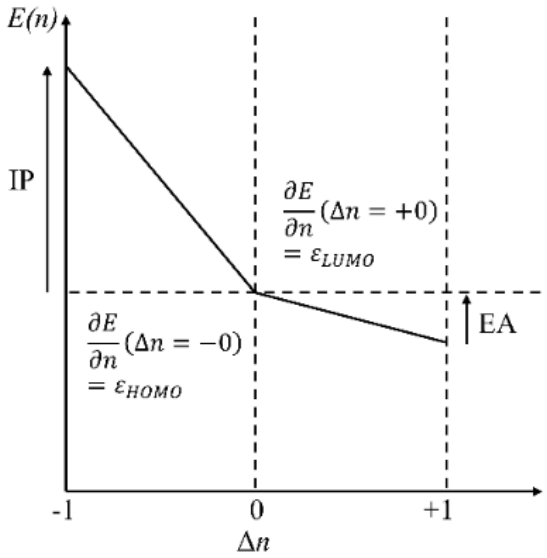

Source: Elaborated by the author.

CHAPTER 3

3. Materials

3.1 Electron donor-acceptor organic polymers

In the last few decades, considerable progress has been made in the development of BHJ in OSCs based on a blend of a p-type organic semiconductor as donor and an n-type organic semiconductor as acceptor. In general, to produce efficient OSCs, one needs donor and acceptor materials with high charge carrier mobility, complementary absorption bands in the Vis-NIR range, and a small energy offset to minimize voltage losses. In this context, seven molecules described in the next sections, with unique or alternating moieties of electron-rich donor and electron-deficient acceptor have been studied in this work, which ones are seen to be promising materials for photovoltaic application.

3.1.1 Electron donor polymers

Low-bandgap polymers with high HOMO energy level are used as electron donor material of OCSs for harvest more sunlight then reaching high efficiency and present the same structure: a donor core (electron-rich unit) and an acceptor core (electron-deficient unit). This structure is also known as donor-acceptor (D-A) structure.

The poly[(2,6-(4,8-bis(5-(2-ethylhexyl)thiophen-2-yl)-benzo[1,2-b:4,5-b']dithiophene)-alt-(5,5-(1',3'-di-2-thienyl-5',7'-bis(2-ethylhexyl)benzo[1',2'-c:4',5'-c']dithiophene-4,8-dione)], named as PBDB-T (Figure 6), was proposed by Qian et al., a non-halogenated donor polymer based on benzodithiophene (BDT) core (donor unit) with two 2-(2-ethylhexyl)thiophene to extending the BDT electron donating capability and solubility, besides a benzodithiophene-dione (BDD) core being an acceptor unit [135]. The BDT, 2-(2-ethylhexyl)thiophene and BDD unit are highlighted in blue, yellow and red, respectively, in Figure 6.

Figure 6. Molecular structure of PBDB-T.

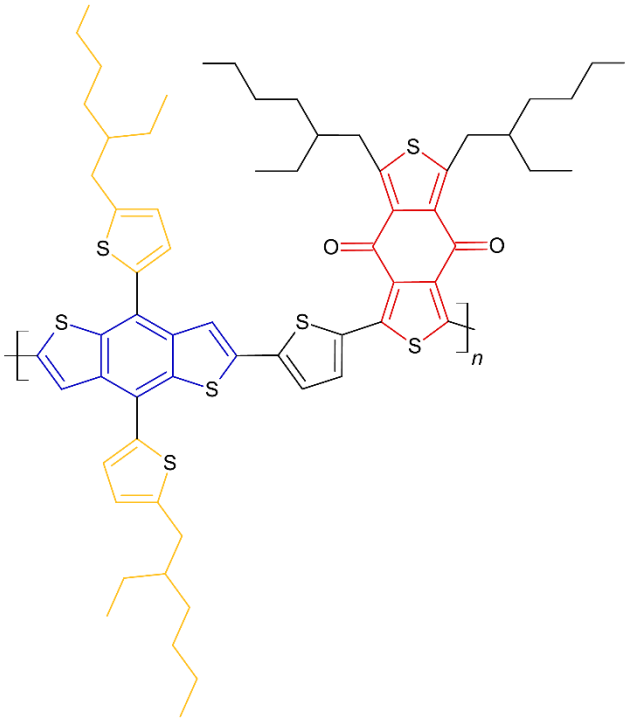

Source: Elaborated by the author.

The poly[(2,6-(4,8-bis(5-(2-ethylhexyl-3-fluoro)thiophen-2-yl)-benzo[1,2-b:4,5-b’]dithiophene))-alt-(5,5-(1’,3’-di-2-thienyl-5’,7’-bis(2-ethylhexyl)benzo[1’,2’-c:4’,5’-c’]dithiophene-4,8-dione)], named as PM6 (Figure 7), was proposed by Zang et al., and shows the same structure of PBDB-T, but use a fluorine-substituted benzodithiophene (BDT-F) core as the donor unit [136]. The BDT-F, 2-(2-ethylhexyl)thiophene and BDD unit are highlighted in blue, yellow and red, respectively, in Figure 7.

Figure 7. Molecular structure of PM6.

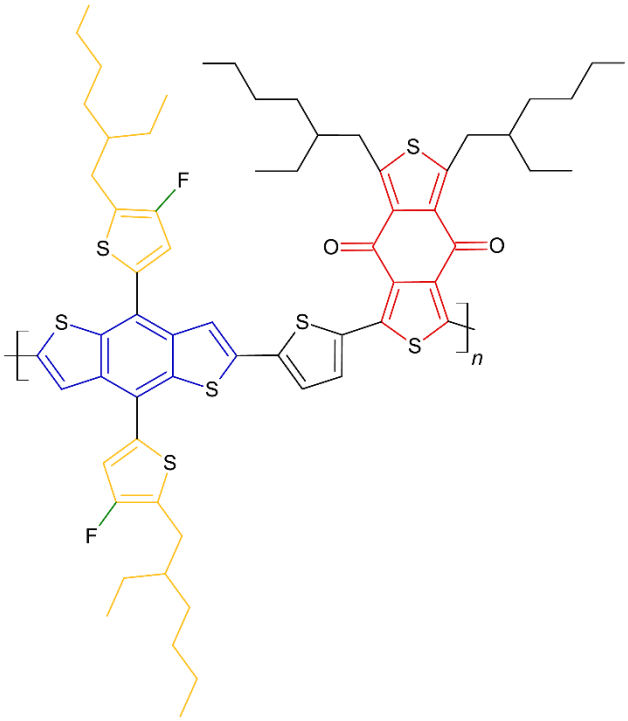

Source: Elaborated by the author.

Following the low-bandgap polymers using the structure donor-acceptor (D-A), Liao et al. proposed a novel PBDB-T-type polymer, poly[4,8-bis(5-(2-ethylhexyl)thiophen-2-yl)benzo[1,2-b;4,5-b']dithiophene-2,6-diyl-alt-(4-(2-ethylhexyl)-3-fluorothieno[3,4-b]thiophene-)-2-carboxylate-2-6-diyl)], named as PTB7-Th (Figure 8), maintaining the BDT core as a donor unit, and as acceptor unit the core is composed by a thieno[3,4-*b*]thipheno (TT) unit with electron-withdrawing fluorine atoms and 2-ethylhexyl carboxylate group (F-TT) [137]. The BDT, 2-(2-ethylhexyl)thiophene and F-TT unit are highlighted in blue, yellow and red, respectively, in Figure 8.

Figure 8. Molecular structure of PTB7-Th.

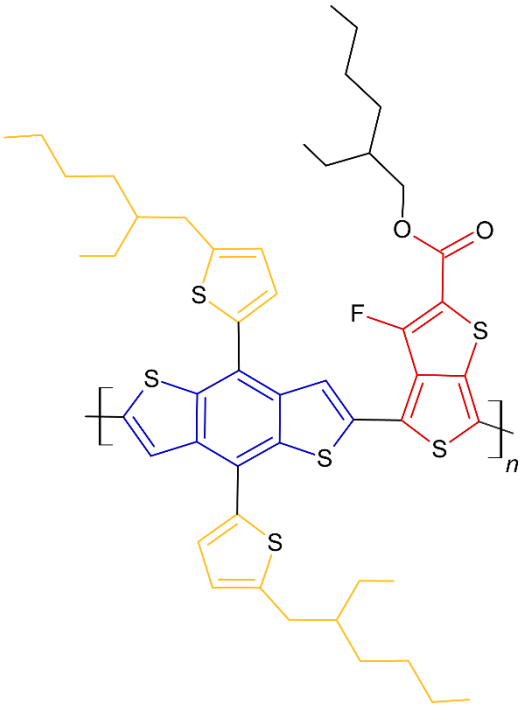

Source: Elaborated by the author.

3.1.2 Electron acceptor polymers

Fullerenes are a family of large all-carbon cage molecules [138]. The most abundant and stable form of fullerene is buckminster fullerene (C_{60}) first discovered in 1985 by Kroto, Heath, O'Brien, Curl and Smalley during experiments on the mechanism of formation of long-chain carbon molecules in interstellar space and circumstellar shells [138]. The low solubility makes fullerenes difficult to handle [34]. It is well-known that this problem can be in part solved by the chemical functionalization of this carbon allotrope [34]. So, fullerenes (Figure 9) and their derivates have been predominately used as electron acceptor of OSCs, because of their isotropic charge transport, high electron mobility and high LUMO energy level [34].

Figure 9. Molecular structure of $PC_{71}BM$.

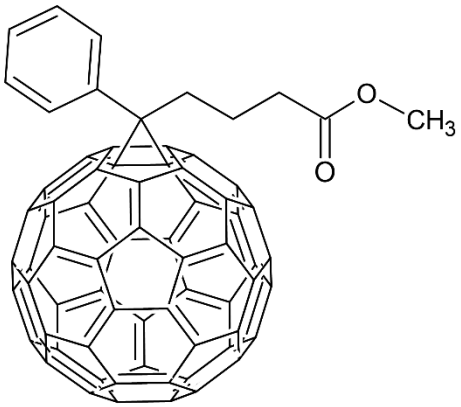

Source: Elaborated by the author.

However, fullerene derivatives have weak absorption in the visible (Vis) and near-infrared (NIR) regions and low solubility due to high symmetry of these molecules, so there are challenges to be overcome to use fullerenes as acceptors [36, 139]. Thereby, in the last 3–4 years, rapid development of low-bandgap non-fullerene acceptors (NFAs) has provided effective ways to improve the performance of OPVs due to their tunable energy levels and strong absorption in the near-infrared region (NIR) [36, 139].

The 2,2'-((2Z,2'Z)-((12,13-bis(2-ethylhexyl)-3,9-diundecyl-12,13-dihydro-[1,2,5]thia diazolo[3,4-e]thieno[2",3'':4',5']thieno[2',3':4,5]pyrrolo[3,2-g]thieno[2',3':4,5]thieno[3,2-b]indole-2,10-diyl)bis(methanylylidene))bis(5,6-difluoro-3-oxo-2,3-dihydro-1H-indene-2,1-diylidene))dimalononitrile, named as Y6 (Figure 10) is small-molecule acceptor, proposed by Cui et al., based on strategy of using a ladder type multi-fused ring with an electron-deficient core as a central unit that showed a narrow bandgap [140]. The central unit is 2, 1, 3-benzothiadiazole (BT), highlighted in blue in the Figure 10, that have sp2-hybridized nitrogen atoms endowing electron-withdrawing character, so creating a charge-deficient region in the middle of the central core [140]. Based on the above considerations, the BT unit was fused with dithienothiophen[3.2-b]-pyrrole, generating a new BT-core-based fused-unit dithienothiophen[3.2-b]-pyrrolobenzothiadiazole, TPBT [140]. The fused TPBT central unit preserves conjugation along the length of the molecule, which allows tuning of the electron affinity. 2-(5,6-Difluoro-3-oxo-2,3-dihydro-1H-inden-1 ylidene)malononitrile (2FIC) units, highlighted in red in the Figure 10, were used as flanking groups to enhance absorption and promote intermolecular interactions and, hence, facilitate charge transport [140]. Moreover, long alkyl side chains were introduced on the terminal of the central unit to increase the solubility [140].

Figure 10. Molecular structure of Y6.

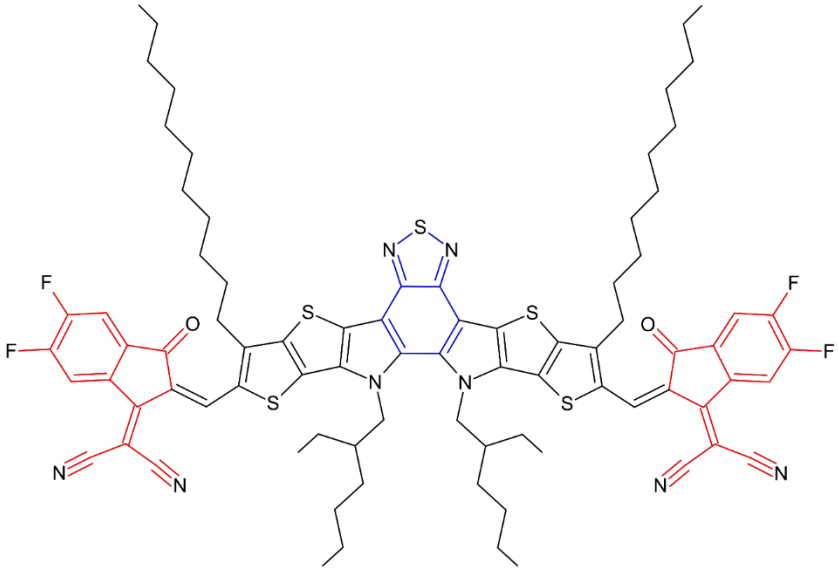

Source: Elaborated by the author.

Following the same structure acceptor-donor-acceptor (A-D-A), the 3,9-bis(2-methylene-(3-(1,1-dicyanomethylene)-indanone))-5,5,11,11-tetrakis(4-hexylphenyl)-dithieno [2,3-d:2’,3’-d’]-s-indaceno[1,2-b:5,6-b’]dithiophene , named as ITIC (Figure 11), was proposed by Lin et al. and based on a bulky seven-ring fused core (indacenodithieno[3,2-b]thiophene, IT), highlighted in blue, end-capped with 2-(3-oxo-2,3-dihydroinden-1-ylidene)malononitrile (INCN) groups, highlighted in red, and with four 4-hexylphenyl groups substituted on it, highlighted in yellow in the Figure 11 [141]. Each INCN has one carbonyl and two cyano groups, and these electron-withdrawing groups can downshift LUMO levels [141]. The push–pull structure in ITIC can induce intramolecular charge transfer and extend absorption [141]. Furthermore, the four rigid 4-hexylphenyl substituents out of the IT main plane can restrict molecular planarity, aggregation, and large phase separation in BHJ blend films [141]. ITIC possesses strong and broad absorption, low LUMO and HOMO energy levels, good electron transport ability, and good miscibility with polymer donors [141].

Figure 11. Molecular structure of ITIC.

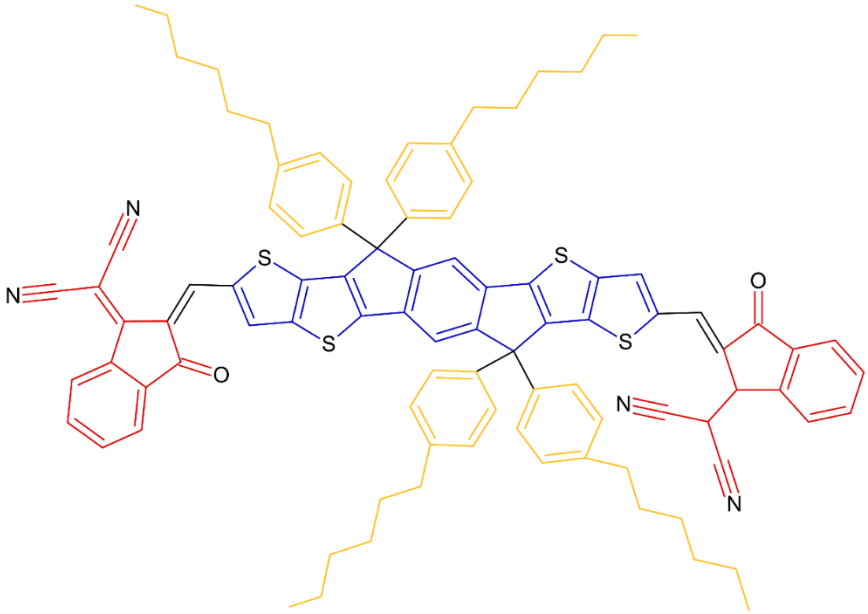

Source: Elaborated by the author.

The 2-[(2*E*)-2-[[16-[(*E*)-[1-(dicyanomethylidene)-3-oxoinden-2-ylidene]methyl]-3,3,13,13-tetrakis(4-hexylphenyl)-7,10,17,20-tetrathiahexacyclo[9.9.0.$0^{2,9}$.$0^{4,8}$.$0^{12,19}$.$0^{14,18}$]icosa-1(11),2(9),4(8),5,12(19),14(18),15-heptaen-6-yl]methylidene]-3-oxoinden-1-ylidene]propane dinitrile, named as O6T-4F, was proposed by Xiao et al. based on donor carbon-oxygen-bridged units, COi8, fused with thienothiophene moieties [142]. COi8, highlighted in blue the Figure 9, possesses higher electron-donating capability due to three electron-richer thienothiophene moieties. Second, a stronger electron-accepting unit, difluoro-substituted IC (DFIC), highlighted in red the Figure 12 was used as the end groups [142]. The enhanced electron-donating capability and electron-accepting capability lead to a very small optical gap (1.26 eV) for O6T-4F, besides the enhanced planarity also renders good charge-transporting property [142].

Figure 12. Molecular structure of O6T-4F.

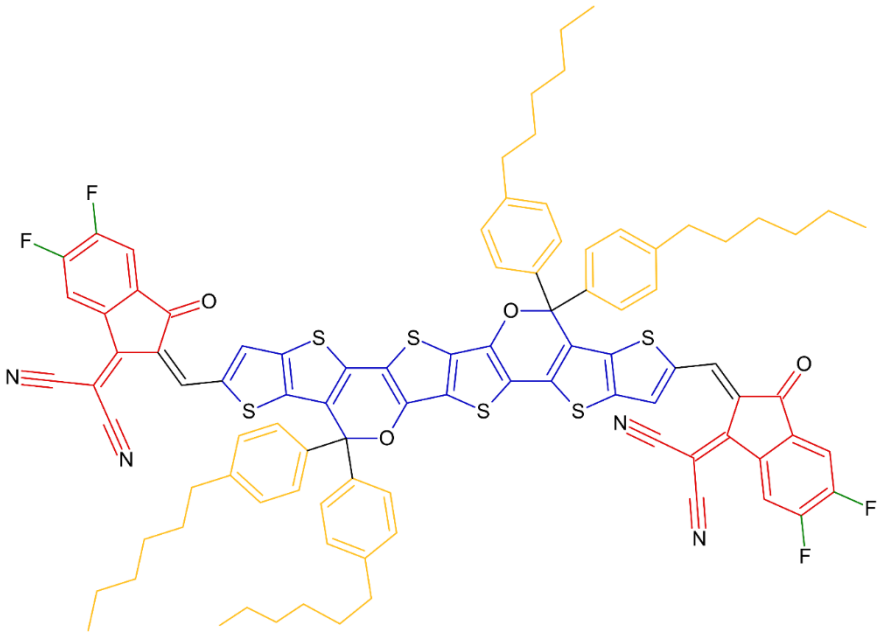

Source: Elaborated by the author.

3.2 Polyfullerenes

The association between the electronic properties of fullerene and the mechanical properties, the stability, as well as the processibility of polymers gives a promising mixture that is interesting in photovoltaic applications [143]. Over the years, polyfullerenes have been proposed in the role of n-type material in all-polymer blends and as electron-selective-layer (ESL) in devices [143]. Here was studied the properties of new classes of soluble main-chain polyfullerenes (Figure 13), HSS-8 (short sidechain) and HSS-16 (long sidechain), synthesized by Dr. Roger Hiorns' group (CNRS-IPREM). All previous information about these polyfullerenes are contained in the work of Santos Silva et al. [143].

Figure 13. Molecular structure of di-bromo monomer.

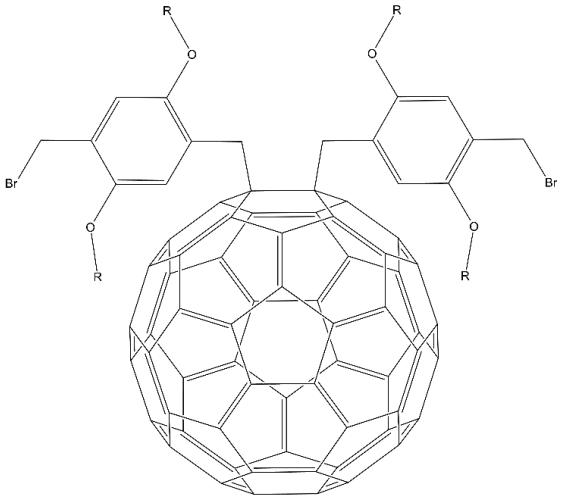

HSS8: R = nC_8H_{17}

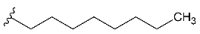

HSS16: R = $nC_{16}H_{33}$

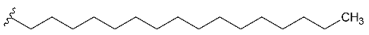

Source: Elaborated by the author.

CHAPTER 4

4.1 Fabrication of thin films and characterization

4.1.1 Langmuir and Langmuir-Schaefer Films

The performance of organic electronic devices based on conjugated polymers, such as in the mobility of charge carriers, is influenced by the orientation of the molecules and the molecular aggregation morphology of the polymer. Within this context, the Langmuir, Langmuir-Blodgett (LB) and Langmuir-Schaefer (LS) techniques stand out, as they provide higher organization at the molecular level and control over the thickness and uniformity of the thin film [144, 145, 146]. Within this context, the polyfullerenes were studied using the Langmuir and LS techniques.

A Langmuir trough (Figure 14) is used to fabricate the thin films, which is basically composed of a teflon trough top (3), which inside is filled with a liquid subphase, two mobile barriers (2), also made of teflon, for symmetrical compression of the film [144, 145, 146]. The trough is also equipped with a surface pressure sensor (4), barrier position detection (1 and 6) and a dipping mechanism (5) used to transfer the film to a solid substrate where it is possible to control the speed of vertical deposition [144, 145, 146].

Figure 14. Langmuir trough

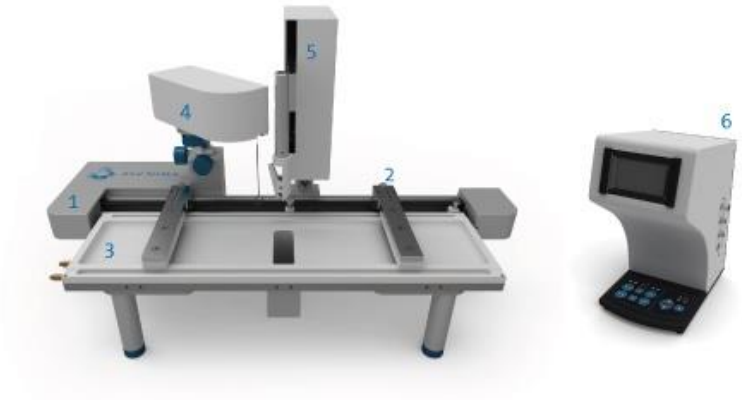

Source: Extracted from [147].

Langmuir films are monomolecular films obtained by spreading a small amount of a material consisting of amphiphilic molecules on a liquid surface [144, 145, 146]. Amphiphilic molecules have both hydrophilic and hydrophobic parts. The hydrophilic part (head) is responsible for spreading while the hydrophobic part (tail) is responsible for the flotation of the

material [144, 145, 146]. The spread material, such as a fatty acid, a polymer or others, is initially dissolved in a volatile solvent, which evaporates after the solution is spread over water [144, 145, 146]. When the monomolecular layer is compressed through mobile barriers, the molecules orient themselves with the hydrophobic parts rising from the surface, generating a highly organized film in the condensed state [144, 145, 146]. Figure 15 represents the organization of a Langmuir film.

Figure 15. Schematic representation of Langmuir principle.

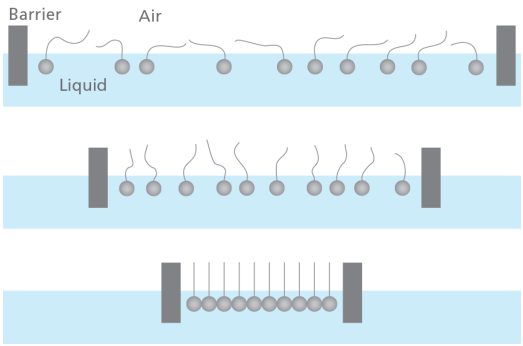

Source: Extracted from [147].

With film compression, the phases of the Langmuir film can be characterized through isotherms of surface pressure versus average molecular area (Figure 16), also known as π-A isotherms [144, 145, 146]. During film compression, it is possible to characterize three distinct phases of the film: gas phase, in which there is no interaction between molecules; liquid phase, in which the molecules begin to interact with each other; and the solid (condensed) phase, with the molecules arranged in a regular arrangement forming a monomolecular thin film [144, 145, 146]. When the film is compressed beyond the solid phase, the molecules can clump together disorderly on top of each other causing the film to collapse, thus losing its monomolecular shape

[144, 145, 146]. In Figure 16, the points G, L_1, L_2 and S represent the gaseous phase, liquid-expanded state, the liquid-condensed state and solid state, respectively.

Figure 16. π-A isotherms of a phospholipid in different phases.

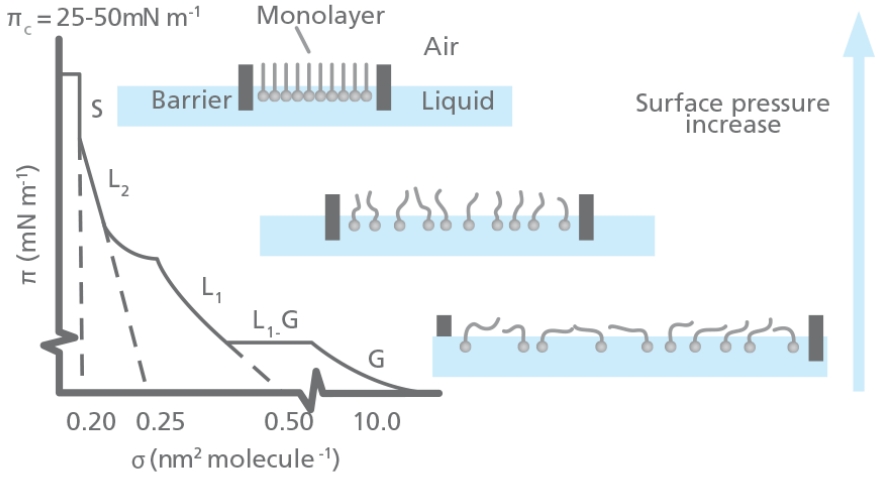

Source: Extracted from [147].

The successive deposition of monolayers of a Langmuir film on the same solid substrate can be performed using the LB and LS techniques (Figure 17). In the LB technique, the film is transferred onto the substrate by immersion and vertical elevation, while in the LS technique, the deposition is carried out by horizontal contact of the substrate with the monolayer [144, 145, 146]. To ensure better deposition, the substrate is slowly brought to the interface with the stabilized Langmuir film [144, 145, 146]. Then, the substrate is also slowly raised, and with this technique, the hydrophobic part of the molecule is in contact with the substrate [144, 145, 146].

Figure 17. LB deposition (to the left) and LS deposition (to the right).

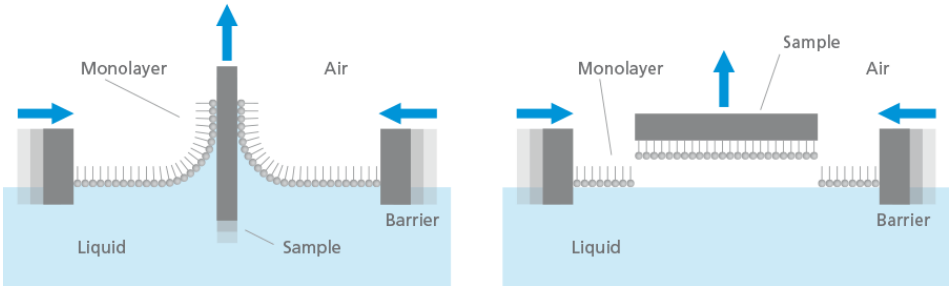

Source: Extracted from [147].

To produce ultrathin films, the LB technique is widely used [144, 145, 146]. However, in the case of some conjugated polymers, the deposition of uniform LB films becomes a problem of great difficulty due to the stiffness of the thin film in the aqueous subphase, which leads to a poor-quality deposition of the film monolayers on solid substrates [144, 145, 146]. An alternative to this problem would be the use of the LS technique, because, in addition to allowing a better transfer, it also allows a faster transfer of the film monolayers to the solid substrate [144, 145, 146].

In this work, the Langmuir and LS films were fabricated using a Langmuir KSV trough model 5000. The first procedure for fabricating the films is to clean the trough and compression barriers, using chloroform to avoid contamination in subphase. Therefore, the liquid subphase is poured over the trough, which in this work was approximately 1350 mL of ultrapure water. The water is obtained from Millipore's water purification system, with a resistivity of 18.2 MΩ. With the end of the previous procedures, the fabrication of the films starts from the process of spreading the solution.

The solutions were made using the materials HSS8 and HSS16, and the solvents were chloroform and xylene. For fabricate the films, the concentration of the solutions for both, HSS8 and HSS16, were 0.2 mg/mL. For a higher quality in the fabricating process, the control parameters are provided in the KSV trough software. The parameters are: volume of the subphase, concentration of the solution, volume to be spread from the solution, molecular mass of the material to be deposited. In concentration used is considered the mass of the respective polyfullerene and the total volume of the solution. Thus, the solutions were spread in the subphase with the aid of a micro syringe, with the total volume spread equal to 750 µL. After spreading, a waiting time of 15 minutes is necessary, so that the chloroform or xylene evaporates, and thus begins the compression of the barriers. Through the pressure isotherm of

the film present in the subphase, a pressure analysis is performed to choose the deposition pressure. In this case, the deposition pressure is equivalent to the point where the film is in the condensed phase with monomolecular thickness. The depositions of the thin film layers on the substrates were carried out at a constant surface pressure equal to 30 mN/m. Symmetrically, the monolayers were compressed by the barriers at a speed of 10 mm/min. For UV absorption were deposited 5 layers onto quartz and for cyclic voltammetry measurements were deposited 30 layers onto ITO.

4.1.2 Optical Characterization in Ultraviolet-Visible (UV-Vis)

One way of optical characterization of thin films is through the measurement of radiation absorption of the sample in the ultraviolet (UV) and visible (Vis) regions of the electromagnetic spectrum, being the regions between 190 and 800 nm where the molecules undergo electronic transitions [148, 149].

The transitions are related to the wavelength (λ) of absorption, while the intensity is dependent on the probability of the transition occurring when the molecular system and the radiation interact [148, 149]. The electrons in a molecule involved in the transitions are non-bonding paired electrons (n electron), such as in N, O, S and halogens, and the electrons in π orbitals, in double or triple bonds [148, 149]. These are the most easily excited electrons and are responsible for most of the electronic spectra in the UV and visible regions [148, 149].

The molecules that contain π electrons or non-bonding electrons can absorb energy in the range of ultraviolet or visible light to excite these electrons to unoccupied anti-bonding orbitals, which correspond to the energy level of the excited state (σ* or π orbitals) [148, 149]. Therefore, the absorption of radiation results in an electronic transition to an anti-bonding orbital. The most common transitions are from π or n orbitals to π* orbitals, and these are represented by $\pi \rightarrow \pi^*$ and $n \rightarrow \pi^*$ transitions [148, 149].

For the UV-Vis characterization of thin films, deposited on ITO substrates, through UV-Vis optical absorption spectroscopy, a VarianCary 100 spectrophotometer was used. The spectrophotometer basically consists of two lamp that produces different wavelengths (deuterium lamp - 200 to 400 nm and tungsten lamp – 400 to 700 nm + NIR), a selector (diffraction grating) that selects the wavelengths, the sample holder and a detector to determine the intensity with which the sample is traversed for the different wavelengths of incident light, providing, per wavelength, the absorption of light. These measurements were taken from the

incidence of light in the range of 200 to 800 nm. The results are presented in the form of unit absorbance.

4.1.3 Cyclic Voltammetry Measurements

Electrochemistry is a powerful tool to probe reactions involving electron transfers [149, 150]. Among electrochemical techniques, CV is a powerful and popular technique commonly employed to investigate the reduction and oxidation processes of molecular species. By the measurement of the electric current as a function of the applied voltage, under proper conditions that promote the polarization of a reference electrode, or a work electrode [149, 150]. CV is a potential-controlled "reversal" electrochemical experiment, whereas a stationary electrode, immersed in a solution without stirring, provides a current as a function of a triangle–shaped excitation potential signal [149, 150]. A linear voltage sweep between two defined values is initially applied. It first goes to the maximum and then returns to the initial value at the same rate [149, 150]. When the applied potential polarizes the electrode surface positively, oxidation occurs, while the opposite direction (negatively polarizes) occurs the reduction of the species present at the electrode interface [149, 150]. The oxidation and reduction currents are limited by mass transport of analyte from the bulk to the diffuse double layer interface [149, 150].

The ‘duck-shaped’ plot generated by cyclic voltammetry is called a cyclic voltammogram [149, 150]. The Figure 18 shows important variables in a cyclic voltammogram as the cathodic peak potential (E_{pc}), the anodic peak potential (E_{pa}), the cathodic peak current (i_{pc}), and the anodic peak current (i_{pa}) [149, 150]. In the i_{pa} current reaches peak maximum (point c) for oxidation at the E_{pa}, and the process for reduction mirrors that for the oxidation, only with an opposite scan direction and an i_{pc} at the E_{pc} (point f) [149, 150].

Figura 18. The ‘duck-shaped’ plot generated by cyclic voltammetry.

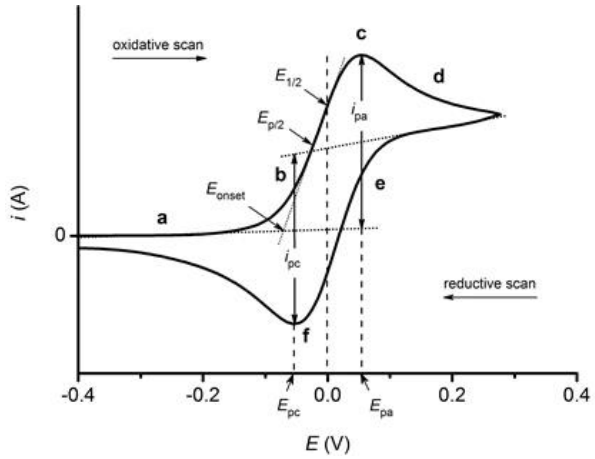

Source: Extracted from [151].

In this work, the CV measurements were carried out using an μAutolab Tipo III potentiostat/galvanostat, in a potential range of –1.0 to 1.5 V with a scan rate of 50 mV/s. This excitation cycle was repeated three times. The supporting electrolyte was a solution of 0.1 mol/L tetrabutylammonium perchlorate (TBAP) in acetonitrile (ACN). The cell was composed of an Ag/AgCl/KCl as the reference electrode, a platinum wire as the counter electrode and cast and LS films over ITO substrates as the working electrode. ITO substrates have geometric surface area equal to 1 cm^2 and sheet resistance between 5 and 15 Ω. The schematic representation setup is shown in Figure 19.

Figure 19. An electrochemical cell setup for CV experiments.

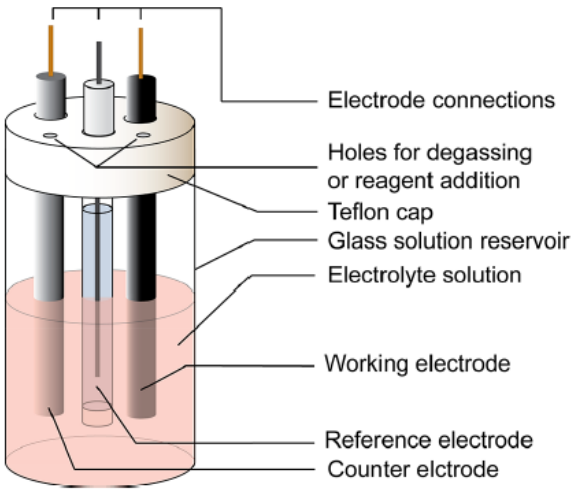

Source: Extracted from [150].

CHAPTER 5

5. Orbital energy modeling for electron donor and acceptor molecules

The energy of the frontier molecular orbitals (HOMO and LUMO) of organic molecules affect a set of distinct OSCs parameters, as short circuit current and open-circuit voltage, linked with power conversion efficiency [[152], [153]]. Originally, the V_{OC} parameter is proportional to the difference between the energy of the HOMO of the p-type material and the LUMO of the n-type one [152, 153]. On the other hand, in order to have a charge transfer (with less energy losses) in place, a threshold value of about 0.2-0.5 eV in energy gap of the p-type LUMO and n-type LUMO should be respected [152, 153]. So, when the LUMO of the n-type is raised to reduce the energy gap between it and the LUMO of the p-type, then the offset energy brought by the junction is reduced and the Voc further improved [152, 153].

Therefore, computational methods are relevant tools to estimate these specific HOMO and LUMO values. In this context, DFT generally predicts the energy levels and molecular geometries in most organic molecules with high accuracy and yields a qualitatively and often also quantitatively correct picture of the electronic structure of molecules [154, 155]. The hybrid functional B3LYP is the most frequently used functional in quantum chemistry calculations and has reasonable accuracy at affordable computational costs [155, 156]. So, B3LYP was used in this work, and all initial calculations were performed using the Gaussian 09 program package with, a relatively small and computationally cheap, 6-31G(d) basis set [157]. The geometry was optimized in the neutral singlet ground state and all computations considered only the isolated monomer in vacuum. The optical parameters of the small molecules were investigated using the TD-DFT. After the DFT calculations, the optimized chemical structure and the values of HOMO and LUMO were obtained.

Figures 20 and 21 present the optimized structures and molecular orbitals for PBDB-T monomer. The values obtained from DFT calculations for the HOMO and LUMO were -5.02 and -2.35 eV, respectively. Using the same basis set, Lu et al. obtained -4.932 and -2.302 eV values for the HOMO and LUMO, respectively. The difference between the results is small and probably due to the calculations carried out by Lu et al. substitute the alkyl branches by ethyl groups to save computing resources [158]. On the experimental side, Qian et al. obtained -5.23 and -3.18 eV for HOMO and LUMO, respectively, by CV measurements [135].

Figure 20. Optimized structure of PBDB-T monomer.

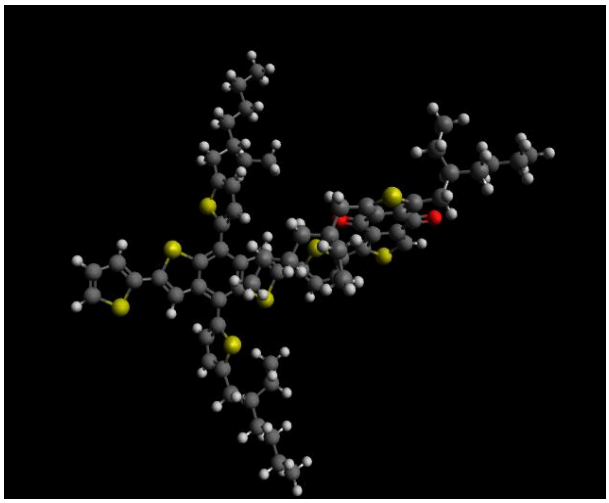

Source: Elaborated by the author.

Figure 21. HOMO (to the left) and LUMO (to the right) orbitals of PBDB-T monomer.

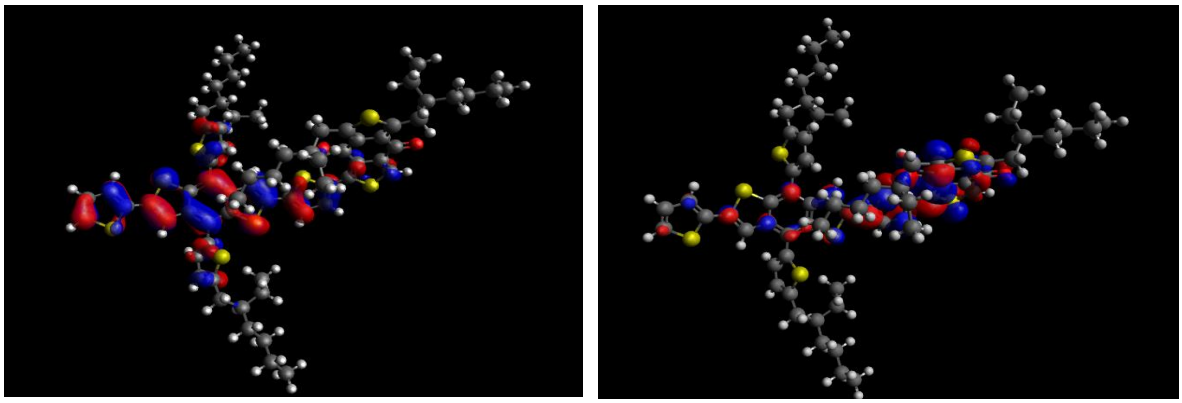

Source: Elaborated by the author.

Figures 22 and 23 present the optimized structure and molecular orbitals for PM6 monomer. The values obtained from DFT calculations for the HOMO and LUMO were -5.12 and -2.46 eV, respectively. Using DFT/6-31G(d,p) basis set, Zhang et al. obtained -5.0 and -2.62 eV values for the HOMO and LUMO, respectively, and using CV measurements obtained -5.45 eV for HOMO and -3.65 eV for LUMO [136]. Zhang et al. carried out calculations on a dimer and added the light atoms (letter p) in the basis set, which is the main reason for the small difference between our results and theirs [136].

Figure 22. Optimized structure of PM6 monomer.

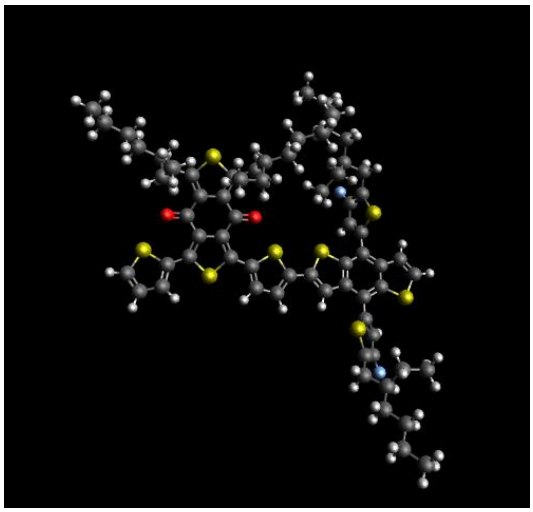

Source: Elaborated by the author.

Figure 23. HOMO (to the left) and LUMO (to the right) orbitals of PM6 monomer.

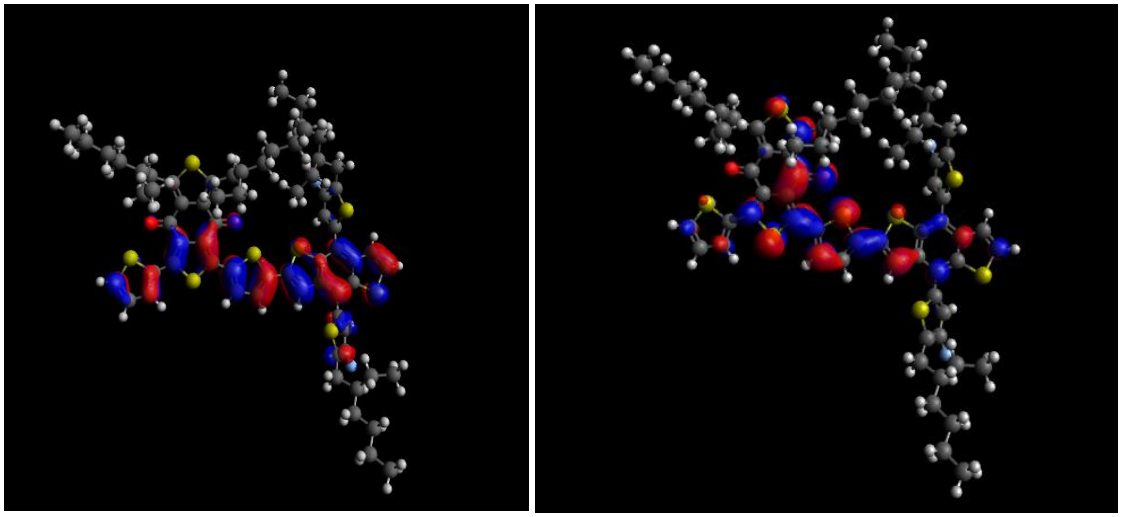

Source: Elaborated by the author.

Figures 24 and 25 present the optimized structure and molecular orbitals for PTB7-Th monomer. For PTB7-Th molecule, the values obtained from DFT calculations for the HOMO and LUMO were -5.12 and -2.27 eV, respectively. In studies carried out by Liao et al. using DFT/6-31G+(d,p) basis set, the values of HOMO and LUMO were -5.13 and -2.23 eV, and by CV measurements were -5.22 eV and -3.64 and, respectively [137]. Our DFT results are slightly different from those reported by Zhang et al., who used a larger basis function by adding diffuse functions (signal +) and the light atoms (letter p).

Figure 24. Optimized structure of PTB7-Th monomer.

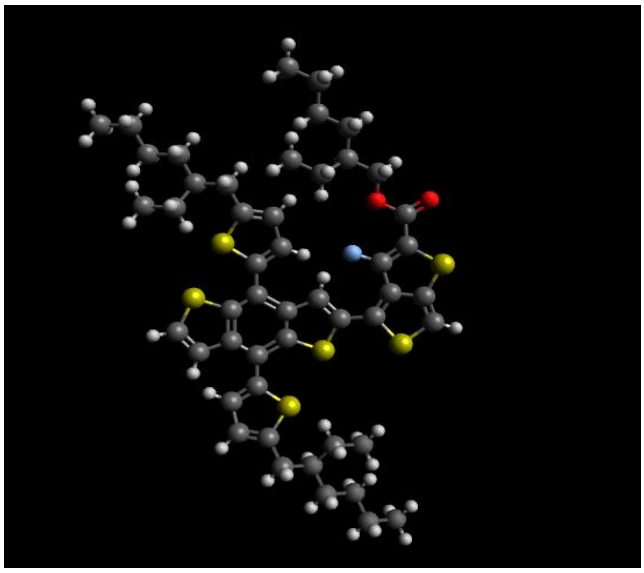

Source: Elaborated by the author.

Figure 25. HOMO (to the left) and LUMO (to the right) orbitals of PTB7-Th monomer.

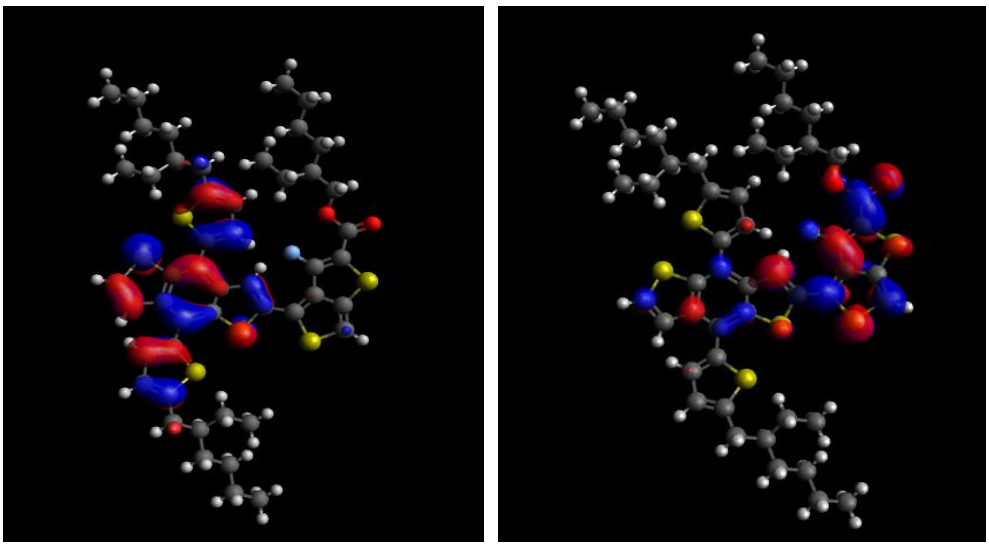

Source: Elaborated by the author.

Figures 26 and 27 present the optimized structure and molecular orbitals for Y6 monomer. The values obtained from DFT calculations for the HOMO and LUMO were -5.55 and -3.51 eV, respectively. In studies carried out by Cui et al. using DFT/6-31G(d,p) basis set, the values of HOMO and LUMO were -5.60 and -3.55 eV, and by CV measurements by Yuan et al. were -5.56 and -3.50 eV, respectively [140, 159]. Even adding the light atoms in the basis set, our results is are slightly different, mainly for the value of LUMO, from those reported by Cui et al.

Figure 26. Optimized structure of Y6 monomer.

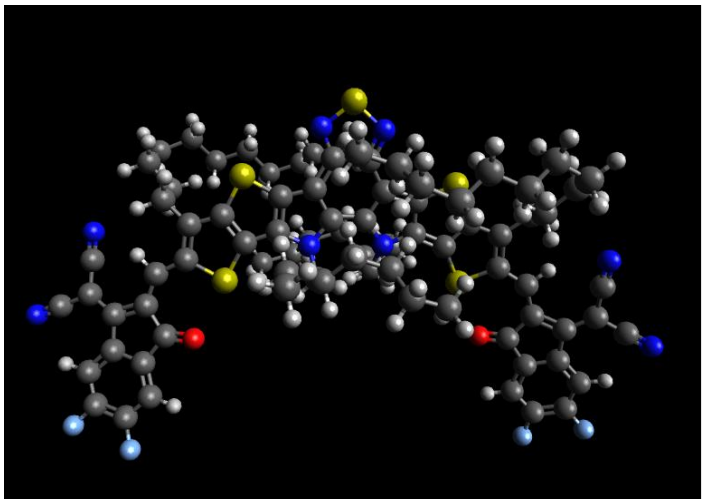

Source: Elaborated by the author.

Figure 27. HOMO (to the left) and LUMO (to the right) orbitals of Y6 monomer.

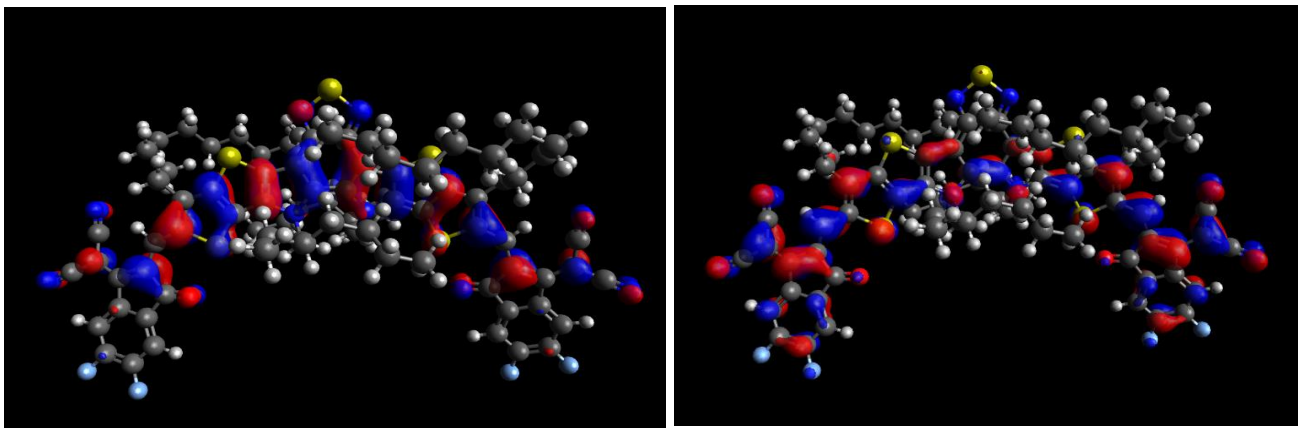

Source: Elaborated by the author.

Figures 28 and 29 present the optimized structure and molecular orbitals for ITIC monomer. The values obtained from DFT calculations for the HOMO and LUMO were -5.46 and -3.35 eV, respectively. The values of HOMO and LUMO, obtained by Lv et al. using DFT/6-31G(d,p) basis set, were -5.49 and -3.37 eV, and by CV measurements, carried out by Lin et al., were -5.48 and -3.83 eV, respectively [141, 160].

Figure 28. Optimized structure of ITIC monomer.

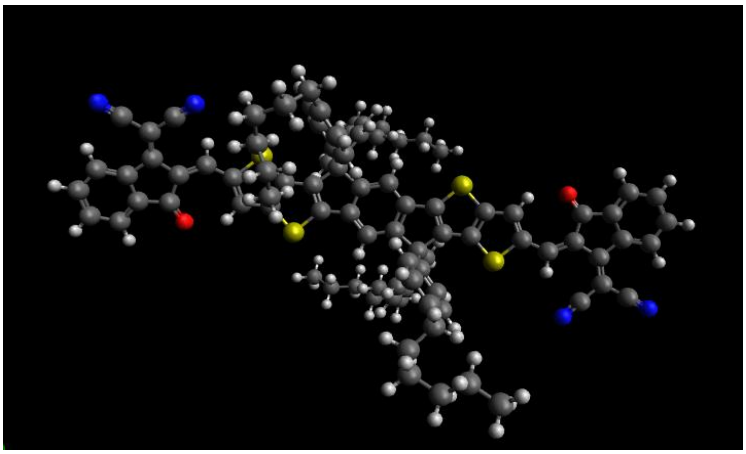

Source: Elaborated by the author.

Figure 29. HOMO (to the right) and LUMO (to the left) orbitals of ITIC monomer.

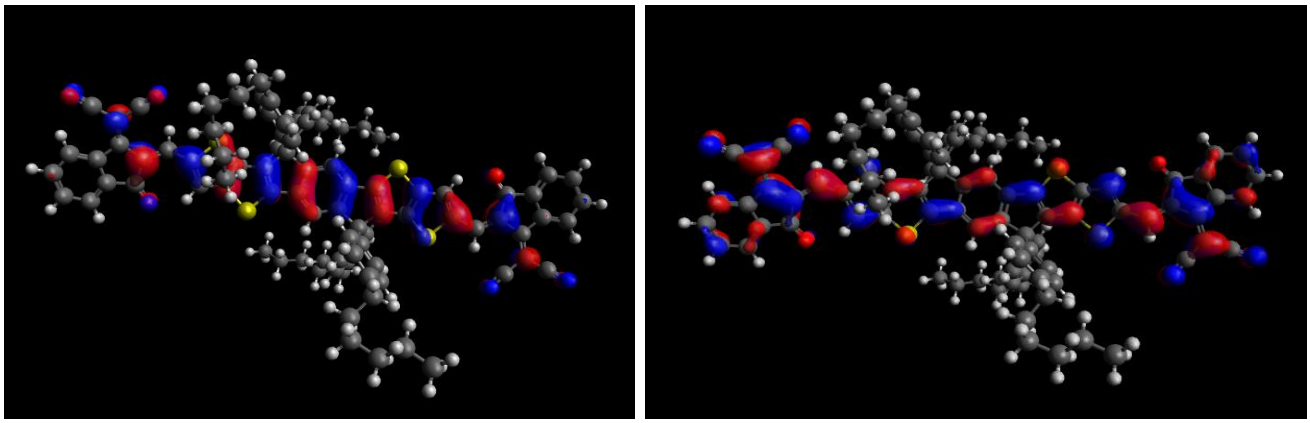

Source: Elaborated by the author.

Figures 30 and 31 present the optimized structure and molecular orbitals for O6T-4F monomer. The values obtained from DFT calculations for the HOMO and LUMO were -5.37 and -3.52 eV, respectively. The values of HOMO and LUMO, obtained by Xiao et al. using CV measurements were -5.50 and -3.88 eV, respectively [142].

Figure 30. Optimized structure of O6T-4F monomer.

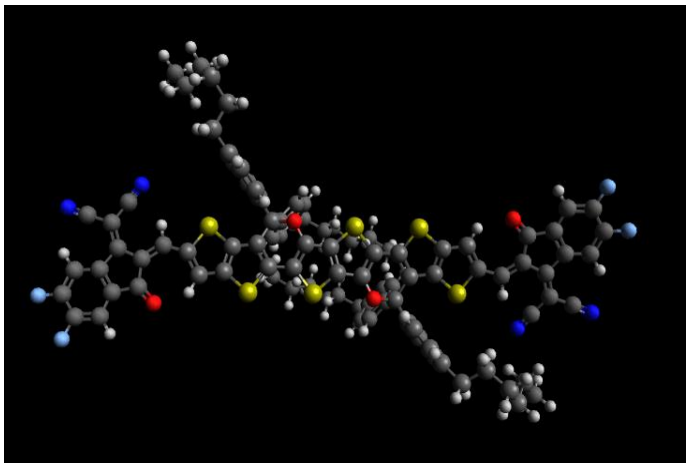

Source: Elaborated by the author.

Figure 31. HOMO (to the right) and LUMO (to the left) orbitals of O6T-4F monomer.

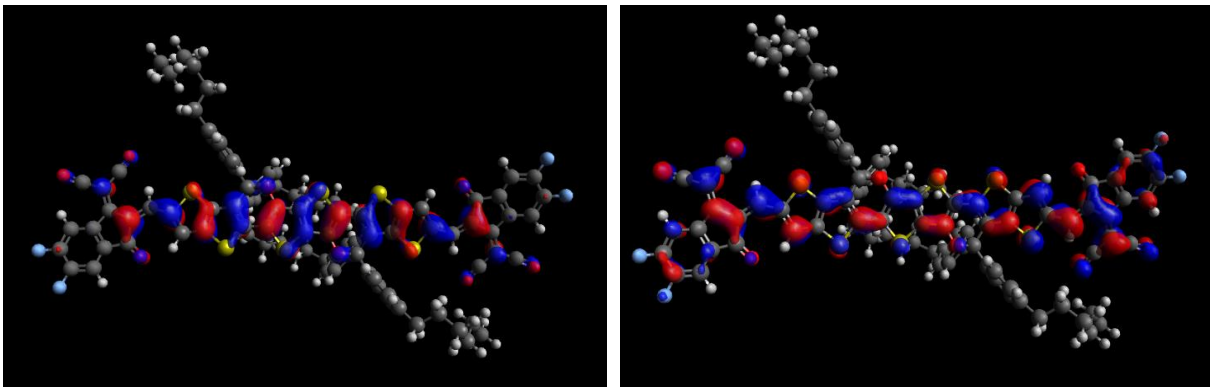

Source: Elaborated by the author.

Figures 32 and 33 present the optimized structure and molecular orbitals for $PC_{71}BM$ monomer. The values obtained from DFT calculations for the HOMO and LUMO were -5.55 and -3.51 eV, respectively. The values of HOMO and LUMO, obtained by Pal et al. using DFT/6-31G+(d,p), were -5.99 and -3.49 eV, respectively, and by CV measurements, obtained by Pan et al., were -5.96 and -3.90 eV, respectively [161, 162].

Figure 32. Optimized structure of $PC_{71}BM$ monomer.

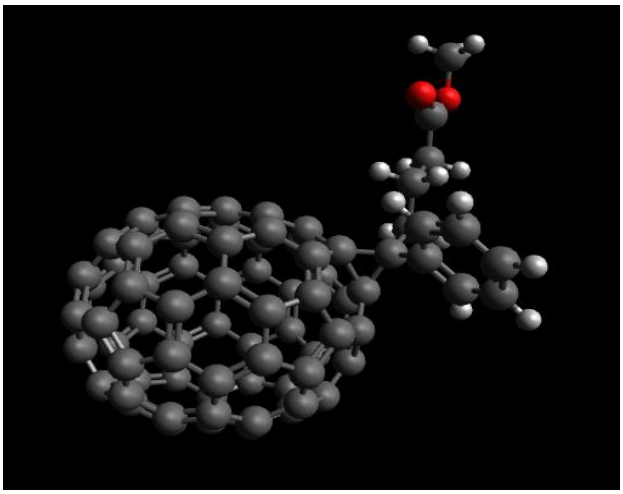

Source: Elaborated by the author.

Figure 33. HOMO (to the right) and LUMO (to the left) orbitals of $PC_{71}BM$ monomer.

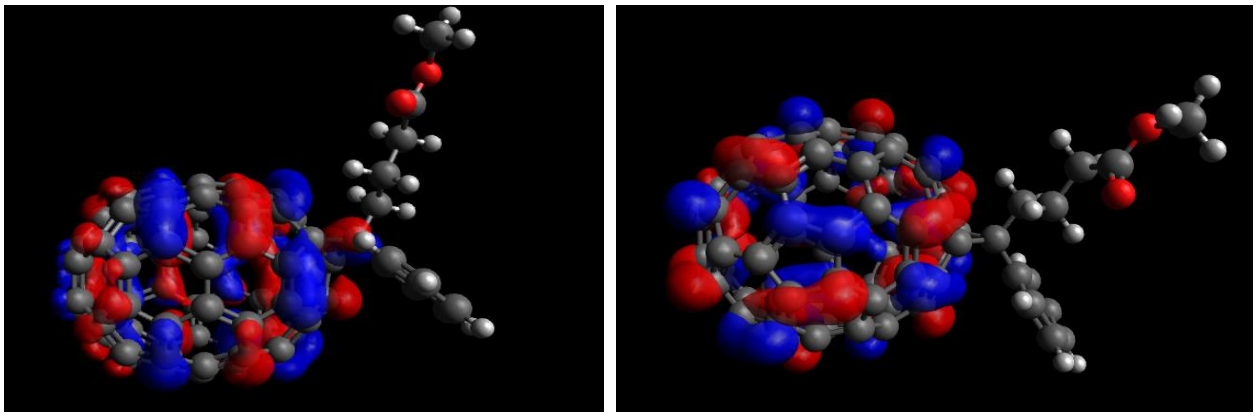

Source: Elaborated by the author.

Table 1 sets up the results from DFT/B3LYP/6-31G(d) for donors and acceptors.

Table 1. HOMO and LUMO values obtained by DFT/B3LYP/6-31G(d) method.

Method	**Molecules**						
DFT/B3LYP/6-31G(d)	PBDB-T	PM6	PTB7-Th	Y6	ITIC	OT6-4F	$PC_{71}BM$
HOMO (eV)	-5.02	-5.12	-5.12	-5.55	-5.46	-5.37	-5.55
LUMO (eV)	-2.35	-2.46	-2.27	-3.51	-3.35	-3.52	-3.51

Source: Elaborated by the author.

Using the mean signed error (MSE) is possible determine how well our theoretical energy values estimated match the experimental energy values from literature. In the donor molecules, the MSE for HOMO energies is equal to -0.213 eV and for LUMO is 1.13 eV. For the acceptors, the MSE for HOMO energies is -0.165 eV and for LUMO is 0.46 eV. Analyzing, for both donor and acceptor molecules, B3LYP gives good correlation to experimental HOMO energies, and for the LUMO, B3LYP gives better estimations than in donors, however the correlation is still poor. This situation is not surprising given all problems that the quantum methods have to calculate virtual orbitals.

An alternative to try better estimate the LUMO values is to perform TD-DFT calculations. Table 2 presents the results from TD-DFT/B3LYP/6-31G(d). In donors, the MSE for LUMO energies is 1.09 eV and for acceptors is 0.46 eV, so, despite the TD-DFT calculations, B3LYP continues giving a poor correlation for LUMO values.

Table 2. HOMO and LUMO values obtained by TD-DFT/B3LYP/6-31G(d) method.

Method	**Molecules**						
TD-DFT/B3LYP/6-31G(d)	PBDB-T	PM6	PTB7-Th	Y6	ITIC	OT6-4F	$PC_{71}BM$
HOMO (eV)	-5.02	-5.12	-5.13	-5.56	-5.46	-5.37	-5.56
LUMO (eV)	-2.35	-2.46	-2.39	-3.50	-3.35	-3.52	-3.50

Source: Elaborated by the author.

In the literature, it is found that the TD-DFT/CAM-B3LYP method can better describe the excited states than B3LYP method [89, 127]. So, a series of calculations was performed by DFT/CAM-B3LYP and TD-DFT/CAM-B3LYP methods using 6-31G(d) basis set, and the results are present in Tables 3 and 4. Using TD-DFT/CAM-B3LYP method, in donors, the MSE for LUMO energies is equal to 2.33 eV, and for acceptors, the MSE for LUMO is 1.57 eV. Thus, for this set of molecules, the correlation for TD-DFT/CAM-B3LYP method is much poor than B3LYP.

Table 3. HOMO and LUMO values obtained by DFT/CAM-B3LYP/6-31G(d) method.

Method	**Molecules**						
TD-DFT/CAM-B3LYP/6-31G(d)	PBDB-T	PM6	PTB7-Th	Y6	ITIC	OT6-4F	$PC_{71}BM$
HOMO (eV)	-6.30	-6.43	-6.39	-6.60	-6.54	-6.44	-6.62
LUMO (eV)	-1.19	-1.23	-1.06	-2.51	-2.30	-2.50	-2.11

Source: Elaborated by the author.

Table 4. HOMO and LUMO values obtained by TD-DFT/CAM-B3LYP/6-31G(d) method.

Method	**Molecules**						
TD-DFT/CAM-B3LYP/6-31G(d)	PBDB-T	PM6	PTB7-Th	Y6	ITIC	OT6-4F	$PC_{71}BM$
HOMO (eV)	-6.20	-6.66	-6.40	-6.60	-6.54	-6.44	-6.62
LUMO (eV)	-1.30	-1.39	-1.30	-2.51	-2.30	-2.50	-2.11

Source: Elaborated by the author.

As the CAM-B3LYP functional failed to predict the values of HOMO and LUMO, it was necessary to use another functional. The problem in predict LUMO values may be related to what can be described as the many-electron self-interaction error (MSIE) or the localization/delocalization error, wherein this error directly influences the DFT description of the ground and excited states [163, 164]. Where, one of the major issues of global hybrid functionals with a fixed fraction of HF exchange is to find a good trade-off between semilocal and HF exchange [163, 164]. On the other hand, full HF exchange is needed for a complete correction of self-interaction and, thus, a correct description of the asymptotic region of the xc potential [163, 164]. On the other hand, however, semilocal exchange is known to mimic short-range static correlation effects that are important for chemical bonding [163, 164]. So, global hybrids must choose between semilocal and HF exchange. One way to try to correct this error is using range-separated hybrid functionals that have the correct asymptotic behavior and system-specific range-separation parameters [163, 164]. Therefore, a series of calculations were

carried out using the ωB97-XD functional with 6-31G(d) basis set, in addition to TD-DFT calculations.

The results from HOMO and LUMO values obtained by ωB97-XD and TD-ωB97-XD are presented in Tables 5 and 6. For both donor and acceptor molecules, the MSE values for HOMO and LUMO was the same for independent and time-dependent approaches. In the donor molecules, the MSE for HOMO energies is equal to -1.68 eV and for LUMO is 2.84 eV. For the acceptors, the MSE for HOMO energies is -1.48 eV and for LUMO is 2.05 eV. Even with all corrections presented by ωB97-XD functional, the results of the correlations are poorer than B3LYP and CAM-B3LYP functionals.

Table 5. HOMO and LUMO values obtained by DFT/ωB97-XD/6-31G(d) method.

Method	**Molecules**						
DFT/ωB97-XD /6-31G(d)	PBDB-T	PM6	PTB7-Th	Y6	ITIC	OT6-4F	$PC_{71}BM$
HOMO (eV)	-6.91	-7.025	-7.00	-7.15	-7.12	-7.00	-7.24
LUMO (eV)	-0.64	-0.745	-0.56	-2.012	-1.80	-2.00	-1.68

Source: Elaborated by the author.

Table 6. HOMO and LUMO values obtained by TD-DFT/ωB97-XD/6-31G(d) method.

Method	**Molecules**						
DFT/TD-ωB97-XD /6-31G(d)	PBDB-T	PM6	PTB7-Th	Y6	ITIC	OT6-4F	$PC_{71}BM$
HOMO (eV)	-6.91	-7.025	-7.00	-7.15	-7.12	-7.00	-7.24
LUMO (eV)	-0.64	-0.745	-0.56	-2.012	-1.80	-2.00	-1.68

Source: Elaborated by the author.

After a series of calculations using different functionals and maintaining the 6-31G(d) basis it was possible to set up a diagram energy for independent (Figure 34 and 36) and time-dependent (Figure 35 and 37) values.

Figure 34. Diagram energy obtained by DFT methods for donor molecules.

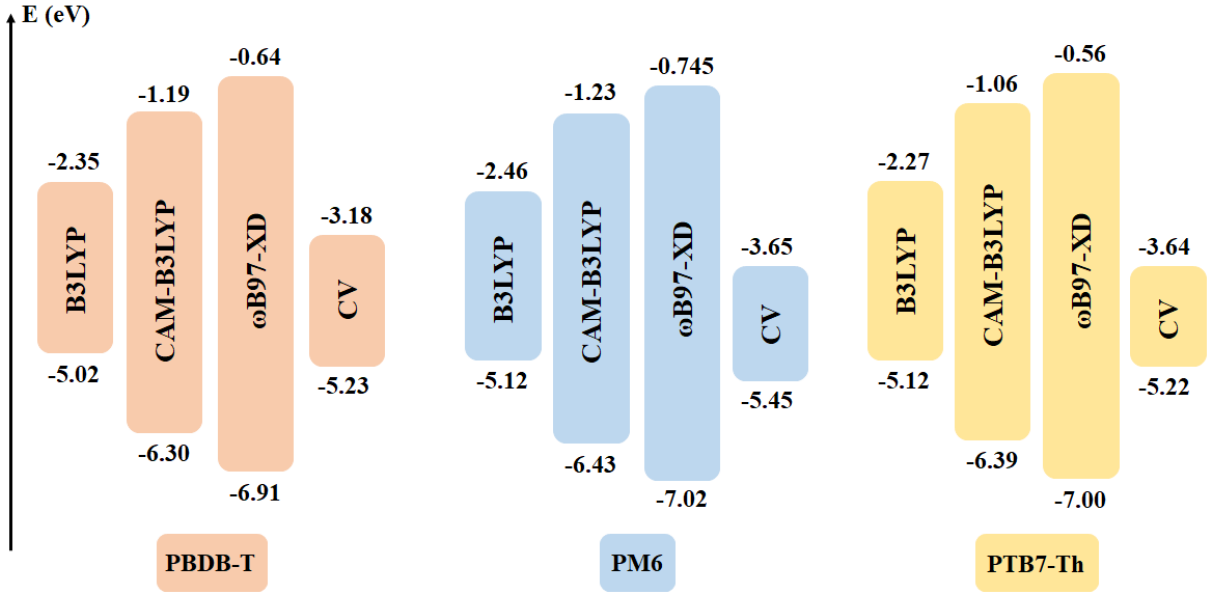

Source: Elaborated by the author.

Figure 35. Diagram energy obtained by TD-DFT methods for donor molecules.

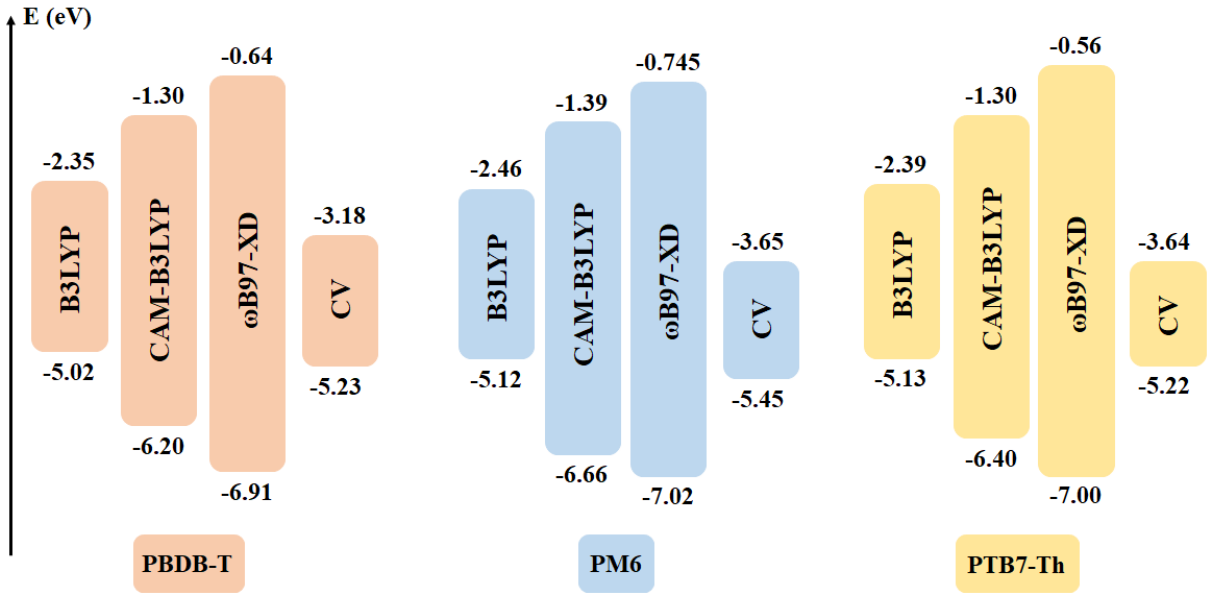

Source: Elaborated by the author.

Figure 36. Diagram energy obtained by DFT methods for acceptor molecules.

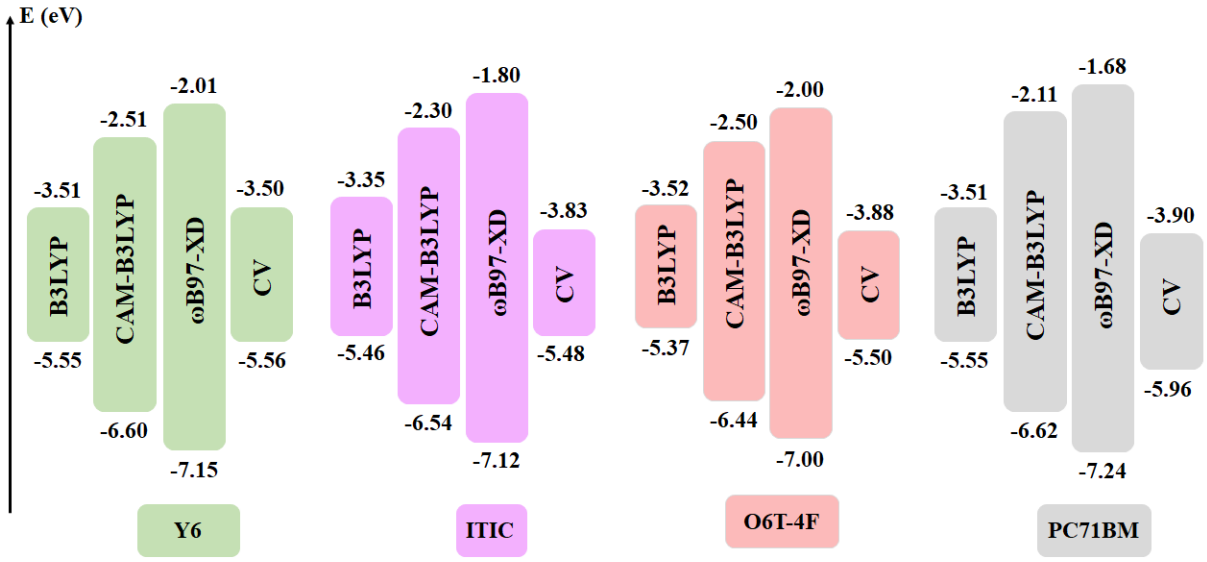

Source: Elaborated by the author.

Figure 37. Diagram energy obtained by TD-DFT methods for acceptor molecules.

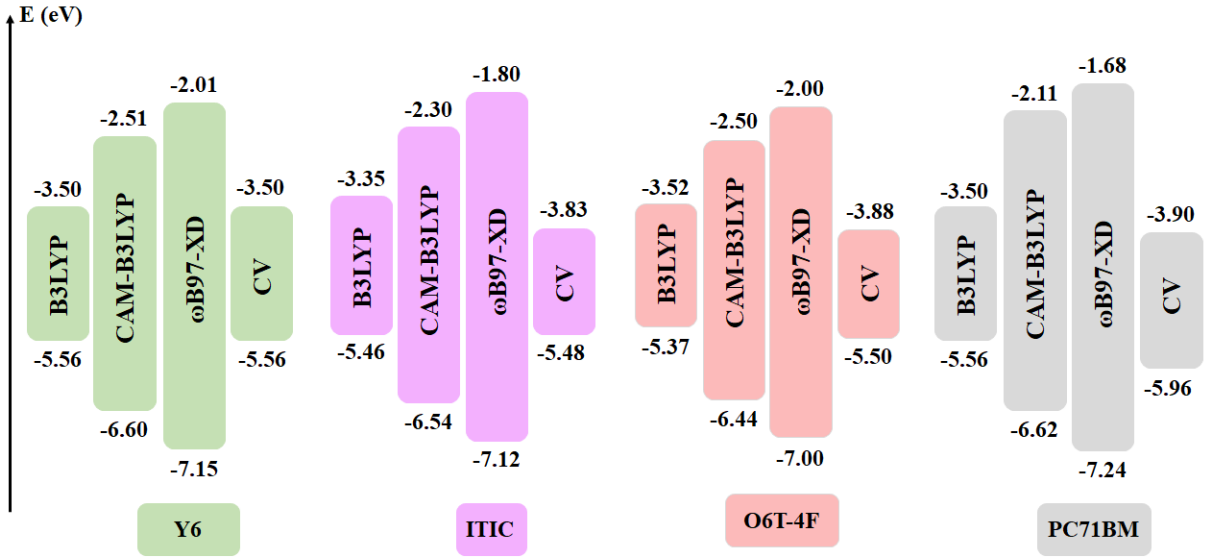

Source: Elaborated by the author.

As 6-31G(d) is a small basis set, it has some limitations to describe the energy of the frontier molecular orbitals. So a new series of calculations were carried out using larger basis set, such as: 6-31G(d,p) and 6-311G(d,p), in B3LYP, CAM-B3LYP and ωB97-XD functionals. Tables 7 - 18 summarize the results coming from all these series of calculations.

Table 7. HOMO and LUMO values from DFT/B3LYP/6-31G(d,p) method.

Method	**Molecules**						
DFT/ B3LYP/6-31G(d,p)	PBDB-T	PM6	PTB7-Th	Y6	ITIC	OT6-4F	$PC_{71}BM$
HOMO (eV)	-5.03	-5.13	-4.41	-5.56	-5.47	-5.37	-5.6
LUMO (eV)	-2.36	-2.47	-2.29	-3.52	-3.36	-3.53	-3.06

Source: Elaborated by the author.

Table 8. HOMO and LUMO values from TD-DFT/B3LYP/6-31G(d,p) method.

Method	**Molecules**						
DFT/ TD-B3LYP/6-31G(d,p)	PBDB-T	PM6	PTB7-Th	Y6	ITIC	OT6-4F	$PC_{71}BM$
HOMO (eV)	-5.03	-5.13	-4.41	-5.56	-5.47	-5.37	-5.6
LUMO (eV)	-2.36	-2.47	-2.29	-3.52	-3.36	-3.53	-3.06

Source: Elaborated by the author.

Table 9. HOMO and LUMO values from DFT/CAM-B3LYP/6-31G(d,p) method.

Method	**Molecules**						
DFT/ CAM-B3LYP/6-31G(d,p)	PBDB-T	PM6	PTB7-Th	Y6	ITIC	OT6-4F	$PC_{71}BM$
HOMO (eV)	-6.30	-6.30	-5.92	-6.61	-6.54	-6.45	-6.62
LUMO (eV)	-1.20	-1.47	-1.29	-2.52	-2.31	-2.70	-2.12

Source: Elaborated by the author.

Table 10. HOMO and LUMO values from TD-DFT/CAM-B3LYP/6-31G(d,p) method.

Method	**Molecules**						
DFT/ TD-CAM-B3LYP/6-31G(d,p)	PBDB-T	PM6	PTB7-Th	Y6	ITIC	OT6-4F	$PC_{71}BM$
HOMO (eV)	-6.30	-6.30	-5.92	-6.61	-6.54	-6.45	-6.62
LUMO (eV)	-1.20	-1.47	-1.29	-2.52	-2.31	-2.70	-2.12

Source: Elaborated by the author.

Table 11. HOMO and LUMO values from DFT/ωB97-XD /6-31G(d,p) method.

Method	**Molecules**						
DFT/ ωB97-XD/6-31G(d,p)	PBDB-T	PM6	PTB7-Th	Y6	ITIC	OT6-4F	$PC_{71}BM$
HOMO (eV)	-6.93	-7.03	-7.00	-7.16	-7.12	-7.00	-7.24
LUMO (eV)	-0.65	-0.757	-0.57	-2.016	-1.81	-2.00	-1.68

Source: Elaborated by the author.

Table 12. HOMO and LUMO values from DFT/TD-ωB97-XD/6-31G(d,p) method.

Method	**Molecules**						
DFT/ TD-ωB97-XD /6-31G(d,p)	PBDB-T	PM6	PTB7-Th	Y6	ITIC	OT6-4F	$PC_{71}BM$
HOMO (eV)	-6.93	-7.03	-7.00	-7.16	-7.12	-7.00	-7.24
LUMO (eV)	-0.65	-0.757	-0.57	-2.016	-1.81	-2.00	-1.68

Source: Elaborated by the author.

Table 13. HOMO and LUMO values from DFT/B3LYP /6-311G(d,p) method.

Method	**Molecules**						
DFT/ B3LYP/6-311G(d,p)	PBDB-T	PM6	PTB7-Th	Y6	ITIC	OT6-4F	$PC_{71}BM$
HOMO (eV)	-5.30	-5.38	-5.36	-5.98	-5.69	-5.61	-5.98
LUMO (eV)	-2.60	-2.67	-2.47	-3.76	-3.58	-3.76	-3.46

Source: Elaborated by the author.

Table 14. HOMO and LUMO values from DFT/TD-B3LYP/6-311G(d,p) method.

Method	**Molecules**						
DFT/ TD-B3LYP/6-311G(d,p)	PBDB-T	PM6	PTB7-Th	Y6	ITIC	OT6-4F	$PC_{71}BM$
HOMO (eV)	-5.30	-5.38	-5.36	-5.98	-5.69	-5.61	-5.98
LUMO (eV)	-2.60	-2.67	-2.47	-3.76	-3.58	-3.76	-3.46

Source: Elaborated by the author.

Table 15. HOMO and LUMO values from DFT/CAM-B3LYP/6-311G(d,p) method.

Method	**Molecules**						
DFT/ CAM-B3LYP/6-311G(d,p)	PBDB-T	PM6	PTB7-Th	Y6	ITIC	OT6-4F	$PC_{71}BM$
HOMO (eV)	-6.47	-6.30	-6.68	-6.83	-6.76	-6.65	-6.62
LUMO (eV)	-1.52	-1.47	-1.36	-2.77	-2.54	-2.90	-2.12

Source: Elaborated by the author.

Table 16. HOMO and LUMO values obtained by DFT/TD-CAM-B3LYP/6-311G(d,p) method.

Method	**Molecules**						
DFT/ TD-CAM-B3LYP/6-311G(d,p)	PBDB-T	PM6	PTB7-Th	Y6	ITIC	OT6-4F	$PC_{71}BM$
HOMO (eV)	-6.47	-6.30	-6.68	-6.83	-6.76	-6.65	-6.62
LUMO (eV)	-1.52	-1.47	-1.50	-2.77	-2.54	-2.90	-2.12

Source: Elaborated by the author.

Table 17. Table 17. HOMO and LUMO values obtained by DFT/ωB97-XD/6-311G(d,p) method.

Method	**Molecules**						
DFT/ωB97-XD/6-311G(d,p)	PBDB-T	PM6	PTB7-Th	Y6	ITIC	OT6-4F	$PC_{71}BM$
HOMO (eV)	-7.071	-7.27	-7.23	-7.35	-7.29	-7.21	-7.24
LUMO (eV)	-0.88	-0.888	-0.74	-2.22	-1.99	-2.18	-1.68

Source: Elaborated by the author.

Table 18. HOMO and LUMO values obtained by DFT/TD-ωB97-XD/6-311G(d,p) method.

Method	**Molecules**						
DFT/TD-ωB97-XD/6-311G(d,p)	PBDB-T	PM6	PTB7-Th	Y6	ITIC	OT6-4F	$PC_{71}BM$
HOMO (eV)	-7.071	-7.27	-7.23	-7.35	-7.29	-7.21	-7.24
LUMO (eV)	-0.88	-0.888	-0.74	-2.22	-1.99	-2.18	-1.68

Source: Elaborated by the author.

For all these series of calculations, the MSE values for HOMO and LUMO of donor and acceptor molecules were the same for time-independent and time-dependent approaches. Table 19 set up all MSE results from HOMO and LUMO from all DFT calculations. It is possible observe that, for all calculations, the calculated LUMO energy, consistently gives values that are less negative (higher lying) than those experimentally determined. From MSE values, the B3LYP functional together with 6-311G(d,p) basis set give the best values for HOMO and LUMO, but the problem of obtaining more accurate values for LUMO remains, even for approaches based on 6-311G(d,p) basis set. So, such results highlight that 6-31G(d) small basis set can provide good values for energy levels from frontier molecular orbitals, in addition to saving computational resources.

Table 19. The MSE results from HOMO and LUMO from all DFT calculations.

	MSE			
	Donors		Acceptors	
Functional/Basis set	HOMO (eV)	LUMO (eV)	HOMO (eV)	LUMO (eV)
B3LYP/6-31G(d)	-0.213	1.13	-0.165	0.46
B3LYP/6-31G(d,p)	-0.443	1.11	-0.147	0.65
B3LYP/6-311G(d,p)	-0.047	0.91	-0.167	0.29
CAM-B3LYP/6-31G(d)	-1.073	2.33	-0.90	1.57
CAM-B3LYP/6-31G(d,p)	-0.873	2.17	-0.91	1.51
CAM-B3LYP/6-311G(d,p)	-1.183	2.04	-1.07	1.345
ωB97-XD/6-31G(d)	-1.68	2.84	-1.48	2.055
ωB97-XD/6-31G(d,p)	-1.40	2.83	-1.48	2.052
ωB97-XD/6-311G(d,p)	-1.89	2.654	-1.63	2.41

Source: Elaborated by the author.

The same problem in estimating LUMO values for conjugated polymers was reported by McCormick. Where they presented a series of DFT/B3LYP computations for 22 different conjugated polymer model compounds, and the MSE for LUMO energies was equal to 0.59 eV. Therefore, an alternative presented was calculate the molecular orbital energy in the triplet state, with the molecules being optimized in the neutral singlet ground state and then the single point energy being calculated in the triplet state, both were calculated with B3LYP/6-311G(d).

The MSE was equal to −0.13 eV for energy of the αHOMO of the triplet state, thereby, giving the best correlation with experiment, and, so, αHOMO energy of the triplet state energy is most accurately approximated from the LUMO.

So, another alternative was carried out calculations in the triplet state for our systems. As in the singlet state, all B3LYP/6-31G(d) computations considered only the isolated monomer in vacuum. Here we add one more step to what was proposed by McCormick et al., before to obtain the energy of the αHOMO, the molecules also were optimized in the neutral triplet state after being optimized in the neutral singlet ground state.

Figures 38 and 39 present the αHOMO energy of the triplet state for donors and acceptors, respectively, compared to energy levels in singlet state. In triplet state, the MSE for the energy of the αHOMO in donors and acceptors is equal to -0.22 and -0.47 eV, respectively. So, for donors, the LUMO energy is most accurately approximated from the αHOMO energy of the triplet state, but, in relation to the donors, the correlation worsens compared to singlet state.

Figure 38. Energy diagram comparing HOMO and LUMO values in singlet and triplet states for donor molecules.

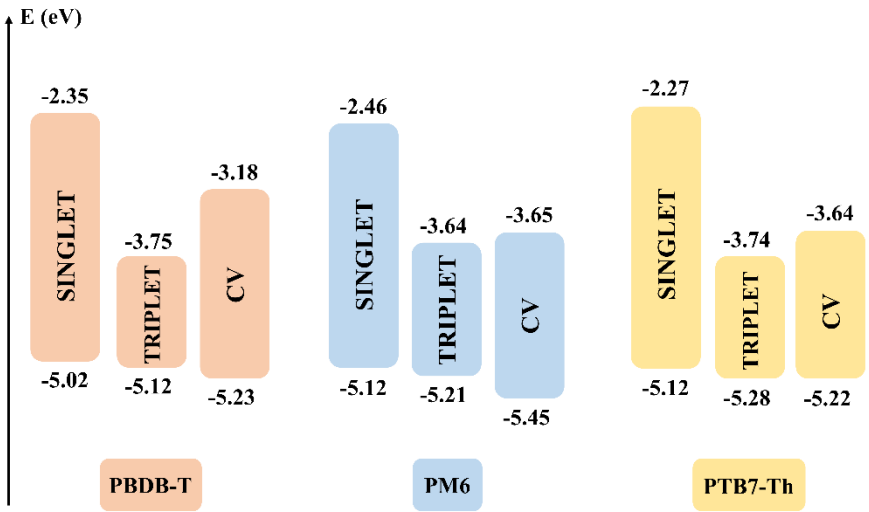

Source: Elaborated by the author.

Figure 39. Energy diagram comparing HOMO and LUMO values in singlet and triplet states for acceptor molecules.

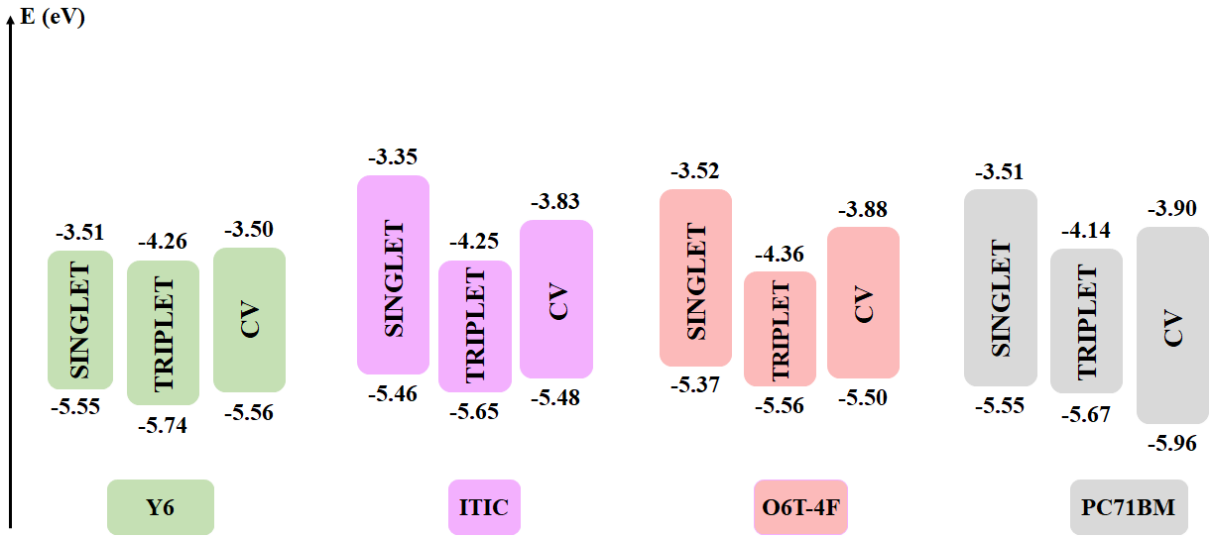

Source: Elaborated by the author.

CHAPTER 6

6. Polyfullerenes

6.1 Langmuir-Schaefer thin films

The study of PCBM and its derivatives using Langmuir techniques aims to characterize the nanostructure of the material which is spread as very thin layers at the water–air interface. Figure 40 shows the surface pressure versus the mean area isotherms (π–A) of HSS8 and HSS16, both of them previously solubilized in either chloroform or xylene (0.2 mg/mL).

Figure 40. π–A isotherms of HSS8 (to the up) and HSS16 (to the down).

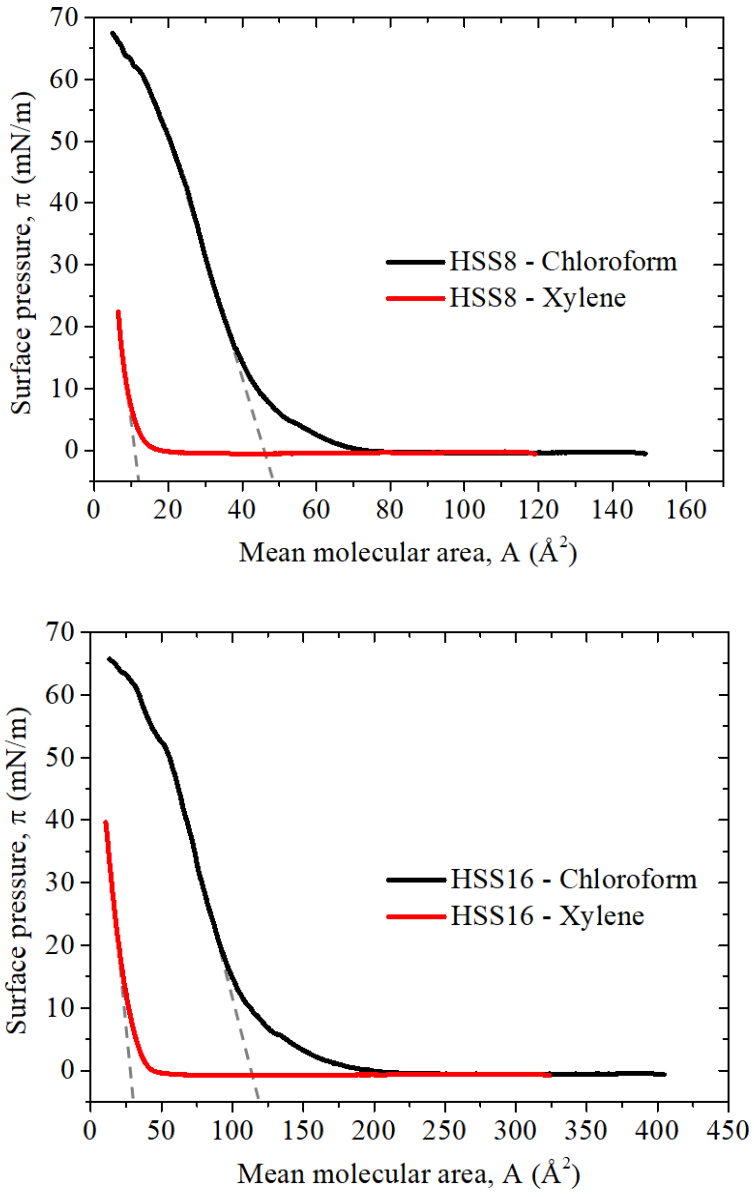

Source: Elaborated by the author.

As the materials are based on PCBM, it is compelling to start with the interpretation of PCBM isotherms because it is possible to find many literature reports regarding fullerene-type monolayers [165, 166]. According to the literature, in PCBM isotherms, it is possible notice the absence of the usual sharp phase transitions of the typical molecule isotherms, and this is a strong indication that this is a liquid-expanded isotherm (according to Harkins' classification), so, the isotherms show a strong indication of the formation disordered aggregates onto the aqueous subphase [165, 166]. The cross-surface area of PCBM is 100 $Å^2$ and the estimated area from the π–A isotherms range from 9.0 to 30 $Å^2$; this means that there is a strong aggregation of PCBM regardless of the solvent used [165, 166].

These results may be due the functional group of the molecule generally is oriented toward the water, a vertical build-up of the molecules in the air–water interface, and this can be a major contribution for the area, and therefore the apparent values are reduced [165, 166]. As reported by Roncaselli et al., the mean area for the PCBM is 23 and 9 $Å^2$ for chloroform and xylene solutions, respectively, suggesting that water surfaces are less appealing to the PCBM when coming from these solutions [166]. Surprisingly, even when in good non-polar solvents such as xylene, one cannot ignore the possibility that PCBM readily forms very small nanoaggregates of several units that arises from the strong fullerene-fullerene interactions, hindering the formation of a true monolayer [166].

In Figure 40, it is possible to see the pristine polyfullerenes with isotherms attained at the Langmuir trough. The area per monomer found for HSS8 was 48 and 12 $Å^2$ for chloroform and xylene solution, respectively, while, for HSS16 was 126 and 33 $Å^2$ for chloroform and xylene solution, respectively. In regard to the isotherms, it can be observed that the polymers, like the PCBM, can be classified as a liquid-expanded type, not achieving the phase related to a condensed phase either [165, 166]. However, the overall isotherm behaviors are quite divergent from one another. The HSS8, both chloroform and xylene solution, presents no distinct phase transitions and has a rather steady upward trend until it reaches the collapse pressure. The collapse pressure for chloroform is 62 mN/m, while, for xylene, the isotherm does not reach the collapse pressure. While the HSS16, the collapse pressure for chloroform is 52 mN/m, and, again, for xylene, the isotherm does not reach the collapse pressure. A possible explanation is that the arrangement and interaction of these materials on the aqueous surface change according to the functional group of each material, which is generally water-oriented, explaining the differences between the areas obtained in the analysis of isotherms, with HSS16 showing the largest area and HSS8 showing the intermediate area in relation to the area of the

PCBM [165, 166]. Through Tables 20 and 21, a relationship can be established between the solvent used and the molecular area obtained in the study of isotherms. The use of different solvents changes the arrangement of molecules because these materials have a low solubility in chloroform, so we found a relatively larger area, while for the xylene solvent, these areas decreased considerably, indicating higher solubility and lower level of aggregation [166].

Table 20. Solubility values for C_{60} in different solvents.

Solvent	**Solubility of C_{60} (mg/ml)**
Chloroform	0.16
Xylene	5.2

Source: Elaborated by the author.

Table 21. Area per molecule for different types of polyfullerene solutions.

Solution	**Area per molecule ($Å^2$)**		
	PCBM	HSS8	HSS16
Chloroform	23	48	126
Xylene	9	12	33

Source: Elaborated by the author.

Since there is no previous literature from these exact polymers, to estimate monomer areas, were carried out the theoretical calculations using DFT/B3LYP/6-31+G(d) method for optimizations of geometries and energies. Calculations were performed using the Gaussian 09 program package. DFT calculations were combined with the Grimme's D3 method to account for longer range dispersion interactions. Using the same parameters, Roncaselli et al. carried out the calculations for C60 and PCBM [166].

According to the DFT/6-31+G(d) results presented in Figure 41, HSS8 and HSS16 have structural differences. HSS16 has an elongation (i) in the ‘X’ direction of about 34% compared to HSS8; (ii) in the ‘Y’ direction, has an elongation direction of about 19% compared to HSS8; and (iii) in the ‘Z’ direction, HSS8 has a strong shortening of about 6%. Table 22 presents the areas of the monomers calculated based on the DFT results. To avoid 'crossing' each other, the arms of the HSS16 molecules (although surrounding mostly the fullerene) start to extend. We found that the calculated molecular areas are all higher than the ones estimated in the π–A isotherms of Figure 40 and Table 21, indicating that both materials aggregate in the Langmuir

trough. In spite of this, the areas obtained by DFT are smaller in 'XY' and 'XZ' planes than that in the 'YZ' plane, which suggests an orientation closer to a 'XY' or 'XZ' configuration against the air–water interface. Another important point is the volume occupied by these materials; HSS8 is 42% smaller than HSS16, which is a significant difference. These results go in the same direction as those obtained for Roncaselli et al. studying PCBM-based oligomers [166].

Figure 41. Theoretical DFT model of the disposition of HSS8 and HSS16 monomers in different orientations.

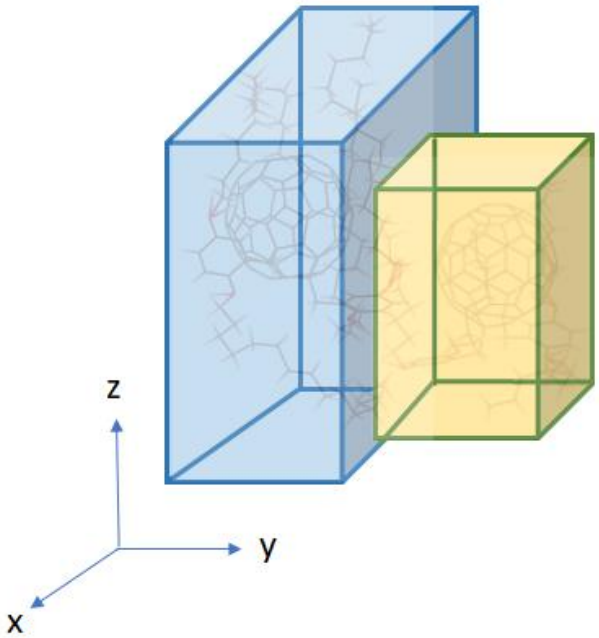

Source: Elaborated by the author.

Table 22. Structural parameters, areas and volumes of C_{60}, PCBM, HSS8 and HSS16 monomers extracted by DFT calculations.

	Structural parameters (Å)			**Area in different orientations ($Å^2$)**			**Volume ($Å^3$)**
Materials	X	Y	Z	XY	YZ	XZ	XYZ
C_{60}	7.02	6.90	6.88	48.4	47.5	48.3	333.2
PCBM	14.79	9.82	6.96	145.2	68.4	102.9	1010.9
HSS8	12.24	15.58	16.62	190.7	258.9	203.4	3169.4
HSS16	18.52	19.18	20.82	355.2	399.3	385.6	7395.5

Source: Elaborated by the author.

Complementary calculations were carried out under an implicit model of the solvent (Polarizable Continuum Model, PCM), making it possible to implicitly average the degrees of freedom of the solvent and to treat the electrostatic interactions (generally dominant in the solvation) for C_{60}, PCBM, HS88 and HSS16 systems. These new calculations show that neither the volumes nor the calculated surfaces are modified whatever the considered the chloroform.

The results from chloroform effects, reveal an important information, i.e., that it is not the electrostatic interactions that govern the behavior of the HSS8 and HSS16 molecules in the solutions in our experiments as xylene and chloroform. The dielectric constant of chloroform and xylene is 4.809 and 2.562, respectively [167]. The origin of the observed differences between the PCM calculations and the experiments is, therefore, to be found elsewhere and in particular in the absence of explicit consideration of the first solvation layer in the PCM model. Because of its smaller size and the presence of chlorine, chloroform is, of the two solvents used in this work, the one that will most likely favor the setting up of these interactions by inserting itself more easily into the structures of the HSS8 and HSS16 molecules, automatically increasing the volume and the surfaces of these systems [166].

6.2 Cyclic Voltammetry

CV is a sophisticated tool to analyze the redox processes of a molecular species, and these processes provide a way to investigate the electronic bandgap diagram of the chosen material [168, 169]. Whereas the HOMO and LUMO of a material are related to the ionization potential (by oxidation potential) and the electron affinity (by reduction potential), respectively [168, 169]. Figures 42 to 45 show the cyclic voltammograms for cast and LS films of the HSS8 and HSS16 materials, solubilized in chloroform and xylene, on an ITO substrate, in a 0.1 mol/L solution of TBAP in acetonitrile, the sweeping was carried out at a scan rate of 50 mV/s.

Figure 42. Cyclic voltammogram for cast films of HSS8 solubilized in chloroform (to the left) and xylene (to the right).

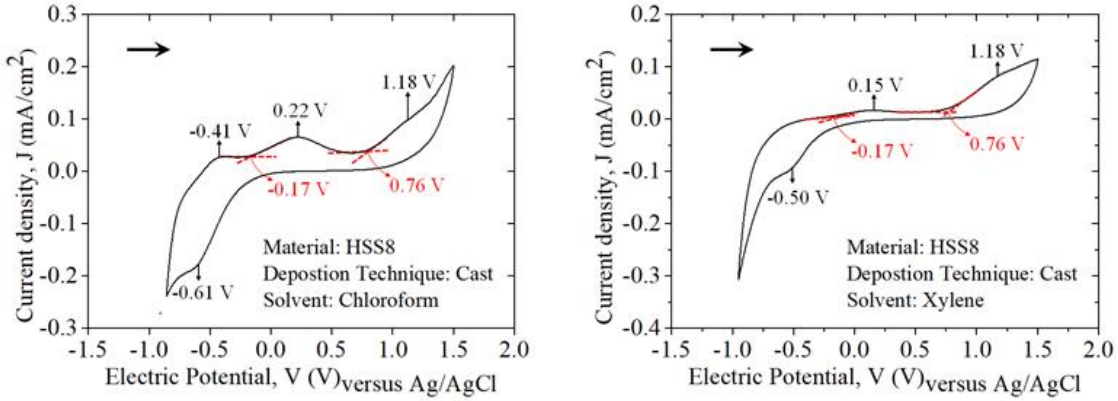

Source: Elaborated by the author.

Figure 43. Cyclic voltammogram for LS films of HSS8 (30 layers) solubilized in chloroform (to the left) and xylene (to the right).

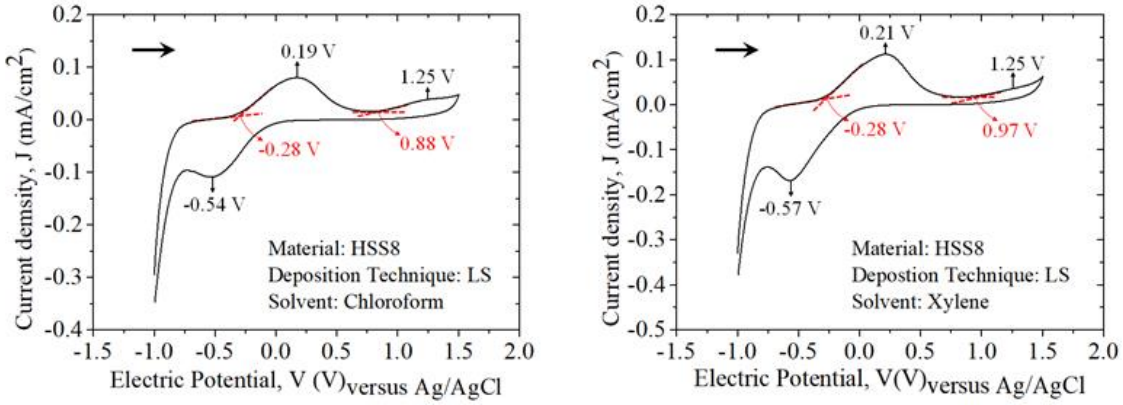

Source: Elaborated by the author.

Figure 44. Cyclic voltammogram for cast films of HSS16 solubilized in chloroform (to the left) and xylene (to the right).

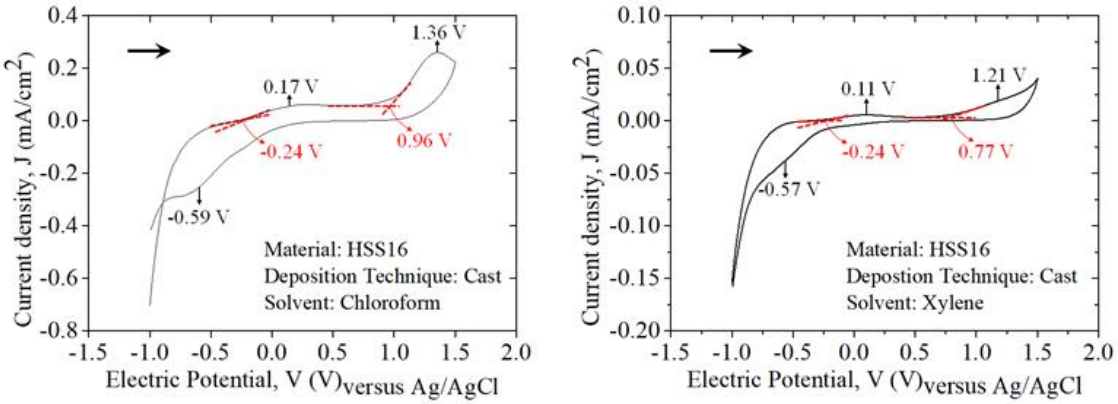

Source: Elaborated by the author.

Figure 45. Cyclic voltammogram for LS films of HSS16 (30 layers) solubilized in chloroform (to the left) and xylene (to the right).

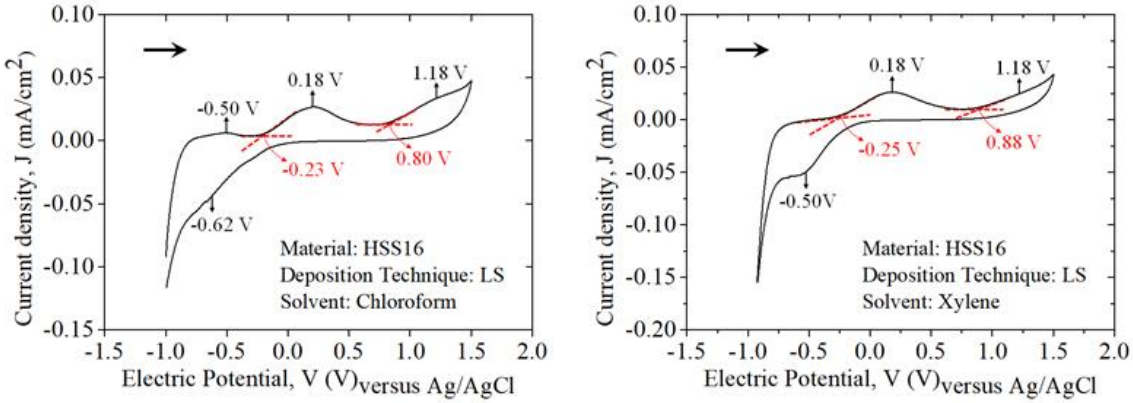

Source: Elaborated by the author.

In the cyclic voltammograms shown in Figure 42, it is possible to observe that the cast film of HSS8 solubilized in chloroform has three oxidation peaks at -0.41, 0.22 and 1.18 V, and a reduction peak at -0.61 V. In the cast film solubilized in xylene, it has two oxidation peaks at 0.15 and 1.18 V, and a reduction peak at -0.50 V. The LS film of HSS8 solubilized in chloroform (Figure 43) has two oxidation peaks at 0.19 V and 1.25 V, and a reduction peak at -0.54 V, while the LS film solubilized in xylene (Figure 43) shows the same pattern, with two reduction peaks at 0.21 and 1.25 V, and a reduction peak at -0.57 V.

For the HSS16 films, from the cyclic voltammograms in Figure 44, it is possible to observe that the cast film solubilized in chloroform has two oxidation peaks at 0.17 and 1.36 V, and a reduction peak at -0.59 V. The cast film solubilized in xylene shows the same pattern, however, with two oxidation peaks at 0.11 and 1.21 V, and a reduction peak at -0.57 V. The LS film solubilized in chloroform (Figure 45) has three oxidation peaks at -0.50, 0.21 and 1.18 V, and a reduction peak at -0.62 V, while the LS film solubilized in xylene (Figure 45) has two reduction peaks at 0.18 and 1.18 V, and a reduction peak at -0.50 V.

Since the measurements were carried out in solution and not under vacuum, the values must be corrected for each type of reference electrode and solution that was employed. The voltammograms show the ionization potential of the thin films at the point where the start of the current increase (onset) occurs before the first oxidation peak. For the HSS8/Cast/Chloroform and HSS16/LS/Chloroform films, the onset before the second oxidation peak was used, due to the difficulty in accurately determine the onset before the first oxidation peak. The energy level for the HOMO can be calculated through the relation $E_{HOMO} =$

$-(E'_{OX} + 4.40)$, and for the Ag/AgCl/KCl electrode, the correction of 4.40 eV was made [170,171].

From the voltammograms, the E_{HOMO} calculated for the cast films of the HSS8, solubilized in chloroform and xylene, for the first oxidation peak is the same for both and equal to -4.23 eV, and for the second oxidation peak also the same for both and equal to -5.16 eV. This same pattern is observed for the first oxidation peak in the LS films of HSS8, where in both chloroform and xylene, the E_{HOMO} calculated for is- 4.12 eV, for the second oxidation peak is -5.28 and -5.37 eV for HSS8 in chloroform and xylene, respectively. The HSS16 films also shows the same pattern as HSS8 films for the first oxidation peak, where for the cast films solubilized in chloroform and xylene, the E_{HOMO} calculated is -4.16 eV, and for the second oxidation peak is -5.36 and -5.17 eV in chloroform and xylene, respectively. For LS films solubilized in chloroform, the E_{HOMO} calculated is -4.17 and -5.20 eV for the first and second oxidation peak, respectively, and in xylene is -4.15 and -5.28 eV for the first and second oxidation peak, respectively.

It was not possible to estimate the electronic affinity in the region of the cathodic potential of the voltammograms (related to the LUMO of the considered material) due to the difficulty to accurately determine the potentials' onset for the second reduction peak. In spite of the electrochemical bandgap being usually higher than the optical bandgap in conjugated polymers, an outcome generally attributed to the formation of free ions in the electrochemical experiment rather than a neutral excited state [172]. So, the optical bandgap can be used in many cases as an approximation for electronic bandgaps, this was already reported for some low-bandgap polymers.

Thence, the optical bandgap energy (E_{gap}^{opt}) was obtained from the UV-Vis absorption measurements, the wavelength related to the optical bandgap is attained by the edge of the absorption spectrum of the film, and allows the calculation of the E_{gap}^{opt} [173]. The E_{gap}^{opt} can be calculated through the relation $E_{gap}^{opt} = \frac{hc}{\lambda} = \frac{1240}{\lambda} eV$, where h represents the Planck's constant in eV·s and c the speed of light in vacuum, in m/s.

In cast films, the absorption spectrum of HSS8 in chloroform (Figure 46) has two peaks at 265 and 355 nm, while in xylene (Figure 46) has three peaks at 227, 277 and 348 nm. Both films have a broad absorption maximum between 420 and 540 nm, which is possibly due to the presence of two or more absorption bands in that region of the spectrum. For HSS16 in chloroform (Figure 48), the absorption spectrum has three peaks at 235, 270 and 350 nm, while in xylene (Figure 48) also has three peaks, but at 233, 275 and 348 nm. For both solvents, the

broad absorption maximum is in the same range as for the HSS8. The absorption spectrum of LS films of HSS8 in chloroform (Figure 47) has three peaks at 200, 270 and 345 nm, while in xylene (Figure 47) also has three absorption peaks, but with values at 200, 270 and 348 nm. Both films have a broad absorption maximum between 400 and 500 nm. For HSS16 in chloroform (Figure 49), has thee peaks at 200, 267 and 340 nm, and in xylene (Figure 49) has thee peaks at 209, 267 and 348 nm. Both films have a broad absorption maximum between 400 and 500 nm.

Figure 46. Absorption spectra for cast films of HSS8 solubilized in chloroform (to the left) and xylene (to the right).

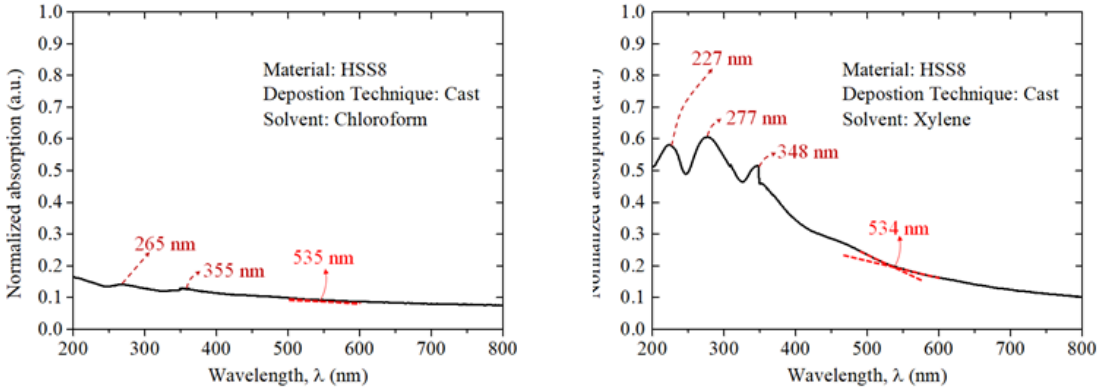

Source: Elaborated by the author.

Figure 47. Absorption spectra for LS films of HSS8 solubilized in chloroform (to the left) and xylene (to the right).

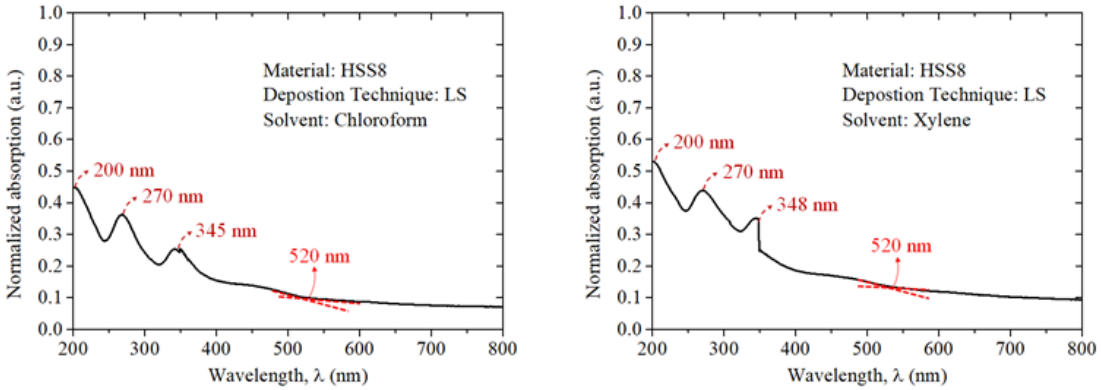

Source: Elaborated by the author.

Figure 48. Absorption spectra for cast films of HSS16 solubilized in chloroform (to the left) and xylene (to the right).

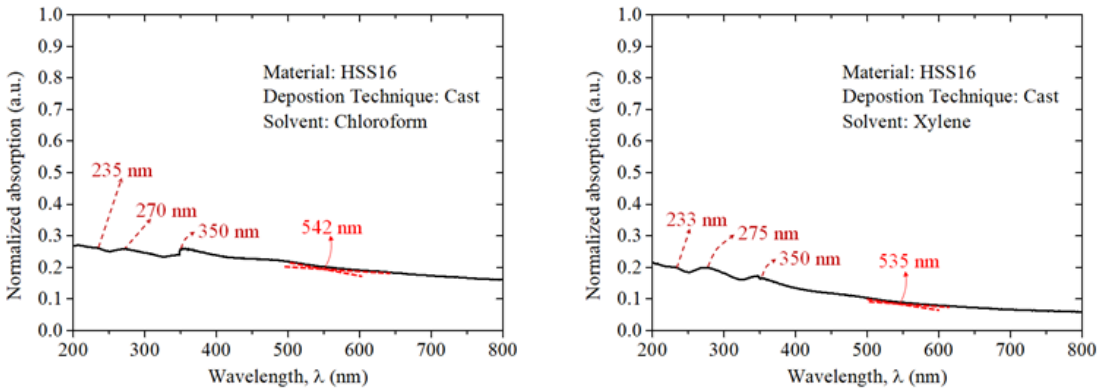

Source: Elaborated by the author.

Figure 49. Absorption spectra for LS films of HSS16 solubilized in chloroform (to the left) and xylene (to the right).

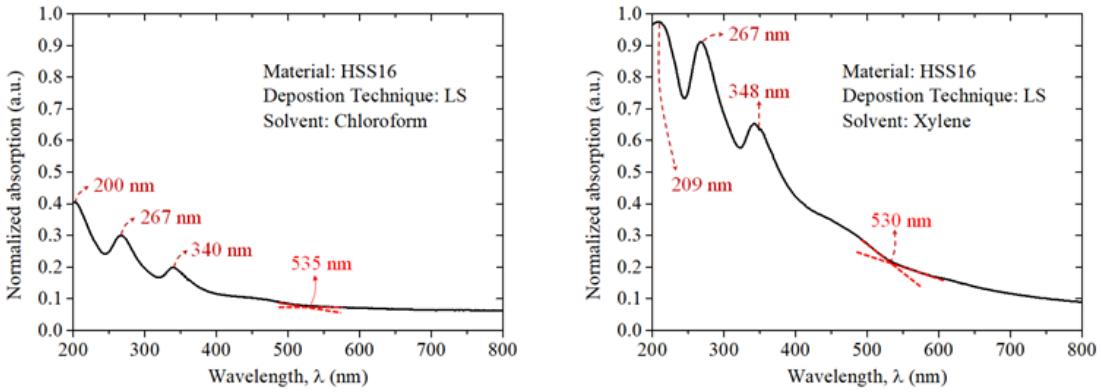

Source: Elaborated by the author.

Comparing with PCBM, in its spectrum has three feature peaks of fullerene derivatives, the [6-6]-addition at 260 nm, 330 nm (C_{60}) and 430 nm ([6,6]-addition in C_{60}) [174, 175]. In LS films, for both solvents, it is possible to observe the peak referring to C_{60}, and the broad absorption is an overlapping between the [6,6]-addition in C60 and 1,4-bis adducts (445 nm), that would result from the ATRAP due to steric effects [143]. The broad absorption is also indicative of the presence of 1,2-adducts (400 nm) [143]. The spectra show more peaks related to PCBM, it is related to the large proportion of PCBM contained in the materials can overlapping many of the electronic properties of oligomers [143, 176].

The use of chloroform and xylene, as solvents, showed a difference in the position of the absorption peaks. This show that the solvent influences not only the aggregation as shown in the study of isotherms, but also the absorption, in which he found that the propensity to form

aggregates depends mainly on solvent polarization and has a direct relationship with the maximum absorption [177, 178]. Due to the organization of the films, these peaks and bands are more evident in the LS films, and not in the cast films [179].

The E_{gap}^{opt} determined for the LS film of HSS8 solubilized in chloroform and xylene (Figure 47) were 2.38 eV (λ_{onset} = 520 nm) for both. For HSS16, the LS film solubilized in chloroform (Figure 49) were 2.32 eV (λ_{onset} = 535 nm), and for film solubilized in xylene (Figure 49) were 2.34 eV (λ_{onset} = 530 nm). For cast films of HSS8 solubilized in chloroform (Figure 47) were 2.38 eV (λ_{onset} = 520 nm), and for the film solubilized in xylene (Figure 47) were 2.32 eV (λ_{onset} = 534 nm). For HSS16, the cast film solubilized in chloroform (Figure 49) were 2.30 eV (λ_{onset} = 542 nm), and for film solubilized in xylene (Figure 49) were 2.32 eV (λ_{onset} = 535 nm). From the E_{HOMO} and E_{gap}^{opt} computed heretofore, it is conceivable to estimate the LUMO energy level, E_{LUMO}, by means of the relation $E_{LUMO} = E_{HOMO} + E_{gap}^{opt}$. Table 23 depicts the values aforementioned attained for the films, that will be used to estimate the energy diagrams.

Table 23. Values of oxidation potential, E_{gap}^{opt}, E_{LUMO} and E_{HOMO} for polyfullerene thin films.

Thin film	Solvent	E_{HOMO}^{OXI} (eV)	E_{LUMO}^{OXI} (eV)	E_{HOMO}^{OXII} (eV)	E_{LUMO}^{OXII} (eV)	E_{gap}^{opt} (eV)
HSS8/Cast	Chloroform	-4.23	-1.85	-5.16	-2.78	2.38
HSS8/Cast	Xylene	-4.23	-1.91	-5.16	-2.84	2.32
HSS8/LS	Chloroform	-4.12	-1.74	-5.28	-2.90	2.38
HSS8/LS	Xylene	-4.12	-1.74	-5.37	-2.99	2.38
HSS16/Cast	Chloroform	-4.16	-1.86	-5.36	-3.06	2.30
HSS16/Cast	Xylene	-4.16	-1.84	-5.17	-2.85	2.32
HSS16/LS	Chloroform	-4.17	-1.85	-5.20	-2.88	2.32
HSS16/LS	Xylene	-4.15	-1.81	-5.28	-2.94	2.34

Source: Elaborated by the author.

Since there is no previous literature from these exact polyfullerenes, to estimate the energy of HOMO and LUMO levels of the monomers, were also carried out the theoretical calculations using DFT/B3LYP/6-31+G(d) method for optimizations of geometries and energies. Calculations were performed using the Gaussian 09 program package. DFT

calculations were combined with the Grimme's D3 method to account for longer range dispersion interactions.

According to the DFT/6-31+G(d) results, for HSS8 monomer in vacuum, the E_{HOMO} is -5.36 eV, and the E_{LUMO} is -3.13 eV. Considering the chloroform effects, the E_{HOMO} and E_{LUMO} is -5.37 and -3.09 eV, respectively. In vacuum, for HSS16 monomer, the E_{HOMO} and E_{LUMO} is -5.36 and -3.18 eV, respectively, and in chloroform, the E_{HOMO} and E_{LUMO} is -5.35 and -3.13 eV, respectively. Comparing with experimental results, it is possible observe that the theoretical results are close to the experimental values calculated from the second oxidation peak, and the discrepancy between experimental values could be related to the CV measurements contains experimental errors and it is noticeable that solid-state packing effects are not included in the DFT calculations, which tend to affect the HOMO and LUMO energy levels in a thin film compared to an isolated monomer as considered in the calculations [180, 181, 182, 183].

CHAPTER 7

7. Conclusion

In this work, in a series of DFT calculations in singlet state, with different functionals and basis set, the B3LYP functional together with 6-311G(d,p) basis set give the best values for HOMO and LUMO, and 6-31G(d) can be used to provide good values for energy levels from frontier molecular orbitals and saving computational resources. For donors, the correlation between the LUMO calculated with experimental results is too poor, while for acceptors, is acceptable. Faced to the problem in DFT calculations predict accurately LUMO values, DFT calculations in triplet states give good correlation for donors, where the LUMO energy is most accurately approximated from the αHOMO energy.

Through the π-A isotherms of polyfullerenes Langmuir films, a strong indication of the formation of disordered aggregates in the aqueous subphase is shown, even when in good non-polar solvents, such as xylene, one cannot ignore the possibility that the PCBM readily form nanoaggregates. Thus, a relationship is established between the solvent used and the molecular area obtained in the study of isotherms. The use of different solvents changes the arrangement of molecules, indicating higher solubility and lower level of aggregation.

The influence of solvent is also evidenced both in UV-Vis and CV measurements. In UV-Vis measurements was found that the propensity to form aggregates depends mainly on the polarization of the solvent and is directly related to the maximum absorption and difference in the position of the absorption peaks. And in CV measurements, the type of solvent influences the oxidation and reduction peaks of the materials, consequently, in the HOMO and LUMO energy levels.

In the junction between DFT calculations and CV and UV-Vis measurements allowed the study of optoelectronic properties. The DFT/B3LYP/6-31+G(d) method provide LUMO values close to experimental values, thus being an important tool for comparing results, since there is no previous literature from these exact polyfullerenes.

REFERENCES

[1] NASROLLAHI, Zahra et al. Environmental pollution, economic growth, population, industrialization, and technology in weak and strong sustainability: using STIRPAT model. **Environment, Development and Sustainability**, v. 22, n. 2, p. 1105-1122, 2020.

[2] VAN TRAN, Nguyen et al. Trade off between environment, energy consumption and human development: Do levels of economic development matter?. **Energy**, v. 173, p. 483-493, 2019.

[3] Available in: <https://www.iea.org/reports/global-energy-co2-status-report-2019>. Access in: February 2022.

[4] GIELEN, Dolf et al. The role of renewable energy in the global energy transformation. **Energy Strategy Reviews**, v. 24, p. 38-50, 2019.

[5] WANG, Hsin-Ping; HE, Jr-Hau. Toward highly efficient nanostructured solar cells using concurrent electrical and optical design. **Advanced Energy Materials**, v. 7, n. 23, p. 1602385, 2017.

[6] RIGHINI, Giancarlo C.; ENRICHI, Francesco. Solar cells' evolution and perspectives: a short review. **In: Solar Cells and Light Management**. Elsevier, 2020. p. 1-32.

[7] BECQUEREL, Alexandre-Edmond. Recherches sur les effets de la radiation chimique de la lumiere solaire au moyen des courants electriques. **Comptes Rendus de L'Academie des Sciences**, v. 9, p. 145-149, 1839.

[8] BECQUEREL, Alexandre-Edmond. Memoire sur les effects electriques produits sous I'influence des rayons solaires. **Comptes Rendus de L'Academie des Sciences**, v. 9, p. 561-567, 1839.

[9] SIEMENS, Werner. On the electromotive action of illuminated selenium, discovered by Mr. Fritts, of New York. **Journal of the Franklin Institute**, v. 6, n. 119, p. 453-456, 1885.

[10] CHAPIN, Daryl Muscott; FULLER, Calvin Souther; PEARSON, Gerald Leondus. A new silicon p-n junction photocell for converting solar radiation into electrical power. **Journal of Applied Physics**, v. 25, n. 5, p. 676-677, 1954.

[11] FAHRENBRUCH, Alan; BUBE, Richard. Fundamentals of solar cells: photovoltaic solar energy conversion. Elsevier, 2012.

[12] GEISZ, John F. et al. Six-junction III–V solar cells with 47.1% conversion efficiency under 143 Suns concentration. **Nature Energy**, v. 5, n. 4, p. 326-335, 2020.

[13] Available in: <https://www.nrel.gov/pv/cell-efficiency.html>. Access in: February 2022.

[14] Available in: <https://www.nrel.gov/about/>. Access in: February 2022.

[15] KIM, Sangmo; VAN QUY, Hoang; BARK, Chung Wung. Photovoltaic technologies for flexible solar cells: beyond silicon. **Materials Today Energy**, v. 19, p. 100583, 2021.

[16] PHILIPPS, Simon P.; DIMROTH, Frank; BETT, Andreas W. High-efficiency III–V multijunction solar cells. In: McEvoy's Handbook of Photovoltaics. Academic Press, 2018. p. 439-472.

[17] BAGHERI, Shadi et al. Design and simulation of a high efficiency InGaP/GaAs multi junction solar cell with AlGaAs tunnel junction. **Optik**, v. 199, p. 163315, 2019.

[18] SU, Peidong et al. Pb-Based Perovskite Solar Cells and the Underlying Pollution behind Clean Energy: Dynamic Leaching of Toxic Substances from Discarded Perovskite Solar Cells. **The Journal of Physical Chemistry Letters**, v. 11, n. 8, p. 2812-2817, 2020.

[19] URBINA, Antonio. The balance between efficiency, stability and environmental impacts in perovskite solar cells: a review. **Journal of Physics: Energy**, v. 2, n. 2, p. 022001, 2020.

[20] RIEDE, Moritz; SPOLTORE, Donato; LEO, Karl. Organic Solar Cells—The Path to Commercial Success. **Advanced Energy Materials**, v. 11, n. 1, p. 2002653, 2021.

[21] KIM, Sangmo; VAN QUY, Hoang; BARK, Chung Wung. Photovoltaic technologies for flexible solar cells: beyond silicon. **Materials Today Energy**, v. 19, p. 100583, 2021.

[22] CUI, Yong et al. Over 16% efficiency organic photovoltaic cells enabled by a chlorinated acceptor with increased open-circuit voltages. **Nature communications**, v. 10, n. 1, p. 1-8, 2019.

[23] SALIM, Muath Bani; NEKOVEI, Reza; JEYAKUMAR, R. Organic tandem solar cells with 18.6% efficiency. **Solar Energy**, v. 198, p. 160-166, 2020.

[24] NAITO, Hiroyoshi (Ed.). **Organic Semiconductors for Optoelectronics**. John Wiley & Sons, 2021.

[25] COROPCEANU, Veaceslav et al. Charge-transfer electronic states in organic solar cells. **Nature Reviews Materials**, v. 4, n. 11, p. 689-707, 2019.

[26] GORENFLOT, Julien et al. From Recombination Dynamics to Device Performance: Quantifying the Efficiency of Exciton Dissociation, Charge Separation, and Extraction in Bulk Heterojunction Solar Cells with Fluorine-Substituted Polymer Donors. **Advanced Energy Materials**, v. 8, n. 4, p. 1701678, 2018.

[27] LIANG, Chunjun et al. Modeling and simulation of bulk heterojunction polymer solar cells. **Solar energy materials and solar cells**, v. 127, p. 67-86, 2014.

[28] RAFIQUE, Saqib et al. Fundamentals of bulk heterojunction organic solar cells: An overview of stability/degradation issues and strategies for improvement. **Renewable and Sustainable Energy Reviews**, v. 84, p. 43-53, 2018.

[29] YANG, Fan; SHTEIN, Max; FORREST, Stephen R. Controlled growth of a molecular bulk heterojunction photovoltaic cell. **Nature materials**, v. 4, n. 1, p. 37-41, 2005.

[30] Available in: <https://www.nrel.gov/news/program/2021/new-design-strategy-increases-organic-pv-efficiency.html>. Access in: July 2022.

[31] Available in: <http://www.cstf.kyushu-u.ac.jp/~adachilab/lab/?page_id=3927>. Access in: July 2022.

[32] AN, Cunbin; ZHENG, Zhong; HOU, Jianhui. Recent progress in wide bandgap conjugated polymer donors for high-performance nonfullerene organic photovoltaics. **Chemical Communications**, v. 56, n. 35, p. 4750-4760, 2020.

[33] COLLAVINI, Silvia; DELGADO, Juan Luis. Fullerenes: the stars of photovoltaics. **Sustainable Energy & Fuels**, v. 2, n. 11, p. 2480-2493, 2018.

[34] SPELLER, Emily M. et al. From fullerene acceptors to non-fullerene acceptors: prospects and challenges in the stability of organic solar cells. **Journal of Materials Chemistry A**, v. 7, n. 41, p. 23361-23377, 2019.

[35] HOU, Jianhui et al. Organic solar cells based on non-fullerene acceptors. **Nature materials**, v. 17, n. 2, p. 119-128, 2018.

[36] ZHANG, Guangye et al. Nonfullerene acceptor molecules for bulk heterojunction organic solar cells. **Chemical reviews**, v. 118, n. 7, p. 3447-3507, 2018.

[37] WANG, Yiwen et al. Recent Progress and Challenges toward Highly Stable Nonfullerene Acceptor-Based Organic Solar Cells. **Advanced Energy Materials**, v. 11, n. 5, p. 2003002, 2021.

[38] BI, Pengqing; HAO, Xiaotao. Versatile ternary approach for novel organic solar cells: a review. **Solar RRL**, v. 3, n. 1, p. 1800263, 2019.

[39] FU, Huiting et al. Efficient ternary organic solar cells enabled by the integration of nonfullerene and fullerene acceptors with a broad composition tolerance. **Advanced Functional Materials**, v. 29, n. 4, p. 1807006, 2019.

[40] MENG, Lingxian et al. Organic and solution-processed tandem solar cells with 17.3% efficiency. **Science**, v. 361, n. 6407, p. 1094-1098, 2018.

[41] CUI, Yongjie et al. Recent advances of computational chemistry in organic solar cell research. **Journal of Materials Chemistry C**, v. 8, n. 45, p. 15920-15939, 2020.

[42] MCARDLE, Sam et al. Quantum computational chemistry. **Reviews of Modern Physics**, v. 92, n. 1, p. 015003, 2020.

[43] RUIPEREZ, Fernando. Application of quantum chemical methods in polymer chemistry. **International Reviews in Physical Chemistry**, v. 38, n. 3-4, p. 343-403, 2019.

[44] ECHENIQUE, Pablo; ALONSO, José Luis. A mathematical and computational review of Hartree–Fock SCF methods in quantum chemistry. Molecular Physics, v. 105, n. 23-24, p. 3057-3098, 2007.

[45] POPLE, J. A.; SEEGER, R.; KRISHNAN, R. Variational configuration interaction methods and comparison with perturbation theory. **International Journal of Quantum Chemistry**, v. 12, n. S11, p. 149-163, 1977.

[46] MIHÁLKA, Zsuzsanna É.; SURJÁN, Péter R. Analytic-continuation approach to the resummation of divergent series in Rayleigh-Schrödinger perturbation theory. **Physical Review A**, v. 96, n. 6, p. 062106, 2017.

[47] PIRIS, Mario. Global method for electron correlation. **Physical review letters**, v. 119, n. 6, p. 063002, 2017.

[48] NEESE, Frank et al. Accurate theoretical chemistry with coupled pair models. **Accounts of chemical research**, v. 42, n. 5, p. 641-648, 2009.

[49] WERNER, Hans-Joachim; KNOWLES, Peter J. A second order multiconfiguration SCF procedure with optimum convergence. **The Journal of chemical physics**, v. 82, n. 11, p. 5053-5063, 1985.

[50] WERNER, Hans-Joachim; MEYER, Wilfried. A quadratically convergent multiconfiguration–self-consistent field method with simultaneous optimization of orbitals and CI coefficients. **The Journal of Chemical Physics**, v. 73, n. 5, p. 2342-2356, 1980.

[51] WERNER, Hans-Joachim; MEYER, Wilfried. MCSCF study of the avoided curve crossing of the two lowest 1Σ+ states of LiF. **The Journal of Chemical Physics**, v. 74, n. 10, p. 5802-5807, 1981.

[52] ANDERSSON, Kerstin et al. Second-order perturbation theory with a CASSCF reference function. **Journal of Physical Chemistry**, v. 94, n. 14, p. 5483-5488, 1990.

[53] DO, Khanh et al. Computational methodologies for developing structure–morphology–performance relationships in organic solar cells: A protocol review. **Chemistry of Materials**, v. 29, n. 1, p. 346-354, 2017.

[54] VAN MEER, R.; GRITSENKO, O. V.; BAERENDS, E. J. Physical meaning of virtual Kohn–Sham orbitals and orbital energies: an ideal basis for the description of molecular excitations. **Journal of chemical theory and computation**, v. 10, n. 10, p. 4432-4441, 2014.

[55] BAERENDS, E. J.; GRITSENKO, O. V.; VAN MEER, R. The Kohn–Sham gap, the fundamental gap and the optical gap: the physical meaning of occupied and virtual

Kohn–Sham orbital energies. **Physical Chemistry Chemical Physics**, v. 15, n. 39, p. 16408-16425, 2013.

[56] STOWASSER, Ralf; HOFFMANN, Roald. What do the Kohn− Sham orbitals and eigenvalues mean?. **Journal of the american chemical society**, v. 121, n. 14, p. 3414-3420, 1999.

[57] GAO, Wei et al. Simultaneously increasing open-circuit voltage and short-circuit current to minimize the energy loss in organic solar cells via designing asymmetrical non-fullerene acceptor. **Journal of Materials Chemistry A**, v. 7, n. 18, p. 11053-11061, 2019.

[58] TSUNEDA, Takao et al. On Koopmans' theorem in density functional theory. **The Journal of chemical physics**, v. 133, n. 17, p. 174101, 2010.

[59] ZHANG, Maojie et al. Synthesis and photovoltaic properties of bithiazole-based donor− acceptor copolymers. **Macromolecules**, v. 43, n. 13, p. 5706-5712, 2010.

[60] MCCORMICK, Theresa M. et al. Conjugated polymers: Evaluating DFT methods for more accurate orbital energy modeling. **Macromolecules**, v. 46, n. 10, p. 3879-3886, 2013.

[61] PERDEW, John P. et al. Some fundamental issues in ground-state density functional theory: A guide for the perplexed. **Journal of chemical theory and computation**, v. 5, n. 4, p. 902-908, 2009.

[62] MOUESCA, Jean-Marie. Density functional theory–broken symmetry (DFT–BS) methodology applied to electronic and magnetic properties of bioinorganic prosthetic groups. In: **Metalloproteins**. Humana Press, Totowa, NJ, 2014. p. 269-296.

[63] OVIEDO, M. Belén; ILAWE, Niranjan V.; WONG, Bryan M. Polarizabilities of π-conjugated chains revisited: improved results from broken-symmetry range-separated DFT and new CCSD (T) benchmarks. **Journal of chemical theory and computation**, v. 12, n. 8, p. 3593-3602, 2016.

[64] FAZZI, Daniele et al. Polarons in π-conjugated ladder-type polymers: a broken symmetry density functional description. **Journal of Materials Chemistry C**, v. 7, n. 41, p. 12876-12885, 2019.

[65] YAMAGUCHI, Kizashi; FUKUI, Hiroaki; FUENO, Takayuki. Molecular orbital (MO) theory for magnetically interacting organic compounds. Ab-initio MO calculations of the effective exchange integrals for cyclophane-type carbene dimers. **Chemistry Letters**, v. 15, n. 4, p. 625-628, 1986.

[66] YAMAGUCHI, K. et al. Extended Hartree-Fock (EHF) theory of chemical reactions. **Theoretica chimica acta**, v. 73, n. 5, p. 337-364, 1988.

[67] YAMAGUCHI, K. et al. A spin correction procedure for unrestricted Hartree-Fock and Møller-Plesset wavefunctions for singlet diradicals and polyradicals. **Chemical physics letters**, v. 149, n. 5-6, p. 537-542, 1988.

[68] KITAGAWA, Yasutaka; SAITO, Toru; YAMAGUCHI, Kizashi. Approximate spin projection for broken-symmetry method and its application. **Symmetry (Group Theory) and Mathematical Treatment in Chemistry**, p. 121-139, 2018.

[69] CASANOVA, David; KRYLOV, Anna I. Spin-flip methods in quantum chemistry. **Physical Chemistry Chemical Physics**, v. 22, n. 8, p. 4326-4342, 2020.

[70] BENDUHN, Johannes et al. Impact of Triplet Excited States on the Open-Circuit Voltage of Organic Solar Cells. **Advanced Energy Materials**, v. 8, n. 21, p. 1800451, 2018.

[71] QIN, Linqing et al. Triplet Acceptors with a D-A Structure and Twisted Conformation for Efficient Organic Solar Cells. **Angewandte Chemie International Edition**, v. 59, n. 35, p. 15043-15049, 2020.

[72] CHEN, Zeng et al. Triplet exciton formation for non-radiative voltage loss in high-efficiency nonfullerene organic solar cells. **Joule**, 2021.

[73] GILLETT, Alexander J. et al. The role of charge recombination to triplet excitons in organic solar cells. **Nature**, v. 597, n. 7878, p. 666-671, 2021.

[74] SCHRÖDINGER, Erwin. An undulatory theory of the mechanics of atoms and molecules. **Physical review**, v. 28, n. 6, p. 1049, 1926.

[75] BORN, Max; HEISENBERG, Werner; JORDAN, Pascual. Zur Quantenmechanik. II. **Zeitschrift für Physik**, v. 35, n. 8, p. 557-615, 1926.

[76] HEISENBERG, Werner. Über quantentheoretische Umdeutung kinematischer und mechanischer Beziehungen. In: **Original Scientific Papers Wissenschaftliche Originalarbeiten**. Springer, Berlin, Heidelberg, 1985. p. 382-396.

[77] GOLDSTEIN, Herbert; POOLE, Charles; SAFKO, John. **Classical mechanics**. Addison-Wesley Longman, 2002.

[78] HELRICH, Carl S. **Quantum Theory - Origins and Ideas**. Springer International Publishing, 2021.

[79] LANDAU, Lev Davidovich; LIFSHITZ, Evgenii Mikhailovich. **Quantum mechanics: non-relativistic theory**. Elsevier, 2013.

[80] GRIFFITHS, David J.; SCHROETER, Darrell F. **Introduction to quantum mechanics**. Cambridge University Press, 2018.

[81] BORN, Max. Quantenmechanik der stoßvorgänge. **Zeitschrift für physik**, v. 38, n. 11, p. 803-827, 1926.

[82] JAMMER, Max. Philosophy of Quantum Mechanics. the interpretations of quantum mechanics in historical perspective. 1974.

[83] SCHRÖDINGER, Erwin. Die gegenwärtige Situation in der Quantenmechanik. **Naturwissenschaften**, v. 23, n. 50, p. 844-849, 1935.

[84] EVERETT III, Hugh. " Relative state" formulation of quantum mechanics. **Reviews of modern physics**, v. 29, n. 3, p. 454, 1957.

[85] ATKINS, Peter W.; FRIEDMAN, Ronald S. **Molecular quantum mechanics**. Oxford university press, 2011.

[86] ALTLAND, Alexander; SIMONS, Ben D. **Condensed matter field theory**. Cambridge University Press, 2010.

[87] PARR, Robert G.; YANG, Weitao. **The fundamentals of density functional theory**. New York: Oxford University Press, 1989.

[88] BORN, Max; OPPENHEIMER, Robert. Zur quantentheorie der molekeln. **Annalen der physik**, v. 389, n. 20, p. 457-484, 1927.

[89] TSUNEDA, Takao. Density functional theory in quantum chemistry. 2014.

[90] HARTREE, Douglas R. The wave mechanics of an atom with a non-Coulomb central field. Part I. Theory and methods. In: **Mathematical Proceedings of the Cambridge Philosophical Society**. Cambridge University Press, 1928. p. 89-110.

[91] PAULI, Wolfgang. Über den Zusammenhang des Abschlusses der Elektronengruppen im Atom mit der Komplexstruktur der Spektren. **Zeitschrift für Physik**, v. 31, n. 1, p. 765-783, 1925.

[92] HEISENBERG, Werner. Mehrkörperproblem und Resonanz in der Quantenmechanik. **Zeitschrift für Physik**, v. 38, n. 6, p. 411-426, 1926.

[93] DIRAC, Paul A. M. On the theory of quantum mechanics. **Proceedings of the Royal Society of London. Series A, Containing Papers of a Mathematical and Physical Character**, v. 112, n. 762, p. 661-677, 1926.

[94] SLATER, John C. The theory of complex spectra. **Physical Review**, v. 34, n. 10, p. 1293, 1929.

[95] FOCK, Vladimir. Näherungsmethode zur Lösung des quantenmechanischen Mehrkörperproblems. **Zeitschrift für Physik**, v. 61, n. 1-2, p. 126-148, 1930.

[96] ROOTHAAN, Clemens C. J. New developments in molecular orbital theory. **Reviews of modern physics**, v. 23, n. 2, p. 69-80, 1951.

[97] LENNARD-JONES, J. E. The electronic structure of some diatomic molecules. **Transactions of the Faraday Society**, v. 25, p. 668-686, 1929.

[98] HALL, G. G. The molecular orbital theory of chemical valency VIII. A method of calculating ionization potentials. **Proceedings of the Royal Society of London. Series A. Mathematical and Physical Sciences**, v. 205, n. 1083, p. 541-552, 1951.

[99] BOYS, S. F. Electronic wave functions-I. A general method of calculation for the stationary states of any molecular system. **Proceedings of the Royal Society of London. Series A. Mathematical and Physical Sciences**, v. 200, n. 1063, p. 542-554, 1950.

[100] LEWARS, Errol. Computational chemistry. **Introduction to the theory and applications of molecular and quantum mechanics**, p. 318, 2011.

[101] CRAMER, Christopher J. **Essentials of computational chemistry: theories and models**. John Wiley & Sons, 2013.

[102] HEHRE, W. J.; STEWART, R. F.; POPLE, J. A. self-consistent molecular-orbital methods. I. use of gaussian expansions of Slater-type atomic orbitals. **The Journal of Chemical Physics**, v. 51, n. 6, p. 2657-2664, 1969.

[103] THOMAS, Llewellyn H. The calculation of atomic fields. In: **Mathematical proceedings of the Cambridge philosophical society**. Cambridge University Press, 1927. p. 542-548.

[104] FERMI, Enrico. Eine statistische Methode zur Bestimmung einiger Eigenschaften des Atoms und ihre Anwendung auf die Theorie des periodischen Systems der Elemente. **Zeitschrift für Physik**, v. 48, n. 1-2, p. 73-79, 1928.

[105] DIRAC, Paul A. M. Note on exchange phenomena in the Thomas atom. In: **Mathematical proceedings of the Cambridge philosophical society**. Cambridge University Press, 1930. p. 376-385.

[106] HOHENBERG, Pierre; KOHN, Walter. Inhomogeneous electron gas. **Physical review**, v. 136, n. 3B, p. B864, 1964.

[107] KOHN, Walter; SHAM, Lu J. Self-consistent equations including exchange and correlation effects. **Physical review**, v. 140, n. 4A, p. A1133-A1138, 1965.

[108] VOSKO, Seymour H.; WILK, Leslie; NUSAIR, Marwan. Accurate spin-dependent electron liquid correlation energies for local spin density calculations: a critical analysis. **Canadian Journal of physics**, v. 58, n. 8, p. 1200-1211, 1980.

[109] BECKE, Axel D. Perspective: Fifty years of density-functional theory in chemical physics. **The Journal of chemical physics**, v. 140, n. 18, p. 18A301, 2014.

[110] GUNNARSSON, Olle; LUNDQVIST, Bengt I. Exchange and correlation in atoms, molecules, and solids by the spin-density-functional formalism. **Physical Review B**, v. 13, n. 10, p. 4274, 1976.

[111] GUNNARSSON, O.; JONSON, M.; LUNDQVIST, B. I. Exchange and correlation in inhomogeneous electron systems. **Solid State Communications**, v. 24, n. 11, p. 765-768, 1977.

[112] BURKE, Kieron; PERDEW, John P.; ERNZERHOF, Matthias. Why semilocal functionals work: Accuracy of the on-top pair density and importance of system averaging. **The Journal of chemical physics**, v. 109, n. 10, p. 3760-3771, 1998.

[113] BECKE, Axel D. Density-functional exchange-energy approximation with correct asymptotic behavior. **Physical review A**, v. 38, n. 6, p. 3098, 1988.

[114] PERDEW, John P. Unified theory of exchange and correlation beyond the local density approximation. **Electronic structure of solids' 91**, v. 11, 1991.

[115] PERDEW, John P.; WANG, Yue. Accurate and simple analytic representation of the electron-gas correlation energy. **Physical review B**, v. 45, n. 23, p. 13244, 1992.

[116] PERDEW, John P.; BURKE, Kieron; ERNZERHOF, Matthias. Generalized gradient approximation made simple. **Physical review letters**, v. 77, n. 18, p. 3865, 1996.

[117] BECK, Axel D. Density-functional thermochemistry. III. The role of exact exchange. **J. Chem. Phys**, v. 98, n. 7, p. 5648-6, 1993.

[118] MARDIROSSIAN, Narbe; HEAD-GORDON, Martin. Thirty years of density functional theory in computational chemistry: an overview and extensive assessment of 200 density functionals. **Molecular Physics**, v. 115, n. 19, p. 2315-2372, 2017.

[119] LEE, Chengteh; YANG, Weitao; PARR, Robert G. Development of the Colle-Salvetti correlation-energy formula into a functional of the electron density. **Physical review B**, v. 37, n. 2, p. 785, 1988.

[120] LEVY, Mel. Universal variational functionals of electron densities, first-order density matrices, and natural spin-orbitals and solution of the v-representability problem. **Proceedings of the National Academy of Sciences**, v. 76, n. 12, p. 6062-6065, 1979.

[121] SEIDL, A. et al. Generalized Kohn-Sham schemes and the band-gap problem. **Physical Review B**, v. 53, n. 7, p. 3764, 1996.

[122] TAWADA, Yoshihiro et al. A long-range-corrected time-dependent density functional theory. **The Journal of chemical physics**, v. 120, n. 18, p. 8425-8433, 2004.

[123] YANAI, Takeshi; TEW, David P.; HANDY, Nicholas C. A new hybrid exchange–correlation functional using the Coulomb-attenuating method (CAM-B3LYP). **Chemical physics letters**, v. 393, n. 1-3, p. 51-57, 2004.

[124] CHAI, Jeng-Da; HEAD-GORDON, Martin. Systematic optimization of long-range corrected hybrid density functionals. **The Journal of chemical physics**, v. 128, n. 8, p. 084106, 2008.

[125] CHAI, Jeng-Da; HEAD-GORDON, Martin. Long-range corrected hybrid density functionals with damped atom–atom dispersion corrections. **Physical Chemistry Chemical Physics**, v. 10, n. 44, p. 6615-6620, 2008.

[126] BECKE, Axel D. Density-functional thermochemistry. V. Systematic optimization of exchange-correlation functionals. **The Journal of chemical physics**, v. 107, n. 20, p. 8554-8560, 1997.

[127] MARQUES, Miguel A. L. et al. (Ed.). **Fundamentals of time-dependent density functional theory**. Springer Science & Business Media, 2012.

[128] RUNGE, Erich; GROSS, Eberhard K. U. Density-functional theory for time-dependent systems. **Physical Review Letters**, v. 52, n. 12, p. 997, 1984.

[129] ULLRICH, Carsten A. **Time-dependent density-functional theory: concepts and applications**. OUP Oxford, 2011.

[130] MARQUES, Miguel et al. **Time-dependent density functional theory**. Springer Science & Business Media, 2006.

[131] SEMINARIO, Jorge M. (Ed.). **Recent developments and applications of modern density functional theory**. Elsevier, 1996.

[132] KOOPMANS, Tjalling. Über die Zuordnung von Wellenfunktionen und Eigenwerten zu den einzelnen Elektronen eines Atoms. **physica**, v. 1, n. 1-6, p. 104-113, 1934.

[133] JANAK, James F. Proof that $\partial E/\partial n_i = \varepsilon$ in density-functional theory. **Physical Review B**, v. 18, n. 12, p. 7165, 1978.

[134] PERDEW, John P. et al. Density-functional theory for fractional particle number: derivative discontinuities of the energy. **Physical Review Letters**, v. 49, n. 23, p. 1691, 1982.

[135] QIAN, Deping et al. Design, application, and morphology study of a new photovoltaic polymer with strong aggregation in solution state. **Macromolecules**, v. 45, n. 24, p. 9611-9617, 2012.

[136] ZHANG, Maojie et al. A large-bandgap conjugated polymer for versatile photovoltaic applications with high performance. **Advanced Materials**, v. 27, n. 31, p. 4655-4660, 2015.

[137] LIAO, Sih-Hao et al. Fullerene derivative-doped zinc oxide nanofilm as the cathode of inverted polymer solar cells with low-bandgap polymer (PTB7-Th) for high performance. **Advanced materials**, v. 25, n. 34, p. 4766-4771, 2013.

[138] KROTO, Harold W. et al. C 60: buckminsterfullerene. **Nature**, v. 318, n. 6042, p. 162-163, 1985.

[139] MEREDITH, Paul; LI, Wei; ARMIN, Ardalan. Nonfullerene acceptors: a renaissance in organic photovoltaics?. **Advanced Energy Materials**, v. 10, n. 33, p. 2001788, 2020.

[140] CUI, Yong et al. Over 16% efficiency organic photovoltaic cells enabled by a chlorinated acceptor with increased open-circuit voltages. **Nature communications**, v. 10, n. 1, p. 1-8, 2019.

[141] LIN, Yuze et al. An electron acceptor challenging fullerenes for efficient polymer solar cells. **Advanced materials**, v. 27, n. 7, p. 1170-1174, 2015.

[142] XIAO, Zuo et al. 26 mA cm− 2 Jsc from organic solar cells with a low-bandgap nonfullerene acceptor. **Science Bulletin**, v. 62, n. 22, p. 1494-1496, 2017.

[143] SANTOS SILVA, Hugo et al. Oligo-and poly (fullerene) s for photovoltaic applications: Modeled electronic behaviors and synthesis. **Journal of Polymer Science Part A: Polymer Chemistry**, v. 55, n. 8, p. 1345-1355, 2017.

[144] GINER-CASARES, Juan J.; BREZESINSKI, Gerald; MÖHWALD, Helmuth. Langmuir monolayers as unique physical models. **Current opinion in colloid & interface science**, v. 19, n. 3, p. 176-182, 2014.

[145] BODIK, Michal et al. Langmuir films of low-dimensional nanomaterials. **Advances in Colloid and Interface Science**, v. 283, p. 102239, 2020.

[146] OLIVEIRA JR, Osvaldo N.; CASELI, Luciano; ARIGA, Katsuhiko. The past and the future of Langmuir and Langmuir–Blodgett films. **Chemical Reviews**, v. 122, n. 6, p. 6459-6513, 2022.

[147] Available in: <https://www.biolinscientific.com/measurements/langmuir-and-langmuir-blodgett>. Access in: February 2022.

[148] PASSOS, Marieta L.C.; SARAIVA, M. L. M. F. S. Detection in UV-visible spectrophotometry: Detectors, detection systems, and detection strategies. **Measurement**, v. 135, p. 896-904, 2019.

[149] SKOOG, Douglas A. et al. **Fundamentals of analytical chemistry**. Cengage learning, 2013.

[150] ELGRISHI, Noémie et al. A practical beginner's guide to cyclic voltammetry. **Journal of chemical education**, v. 95, n. 2, p. 197-206, 2018.

[151] Available in: <https://www.ossila.com/pages/cyclic-voltammetry>. Access in: February 2022.

[152] ELUMALAI, Naveen Kumar; UDDIN, Ashraf. Open circuit voltage of organic solar cells: an in-depth review. **Energy & Environmental Science**, v. 9, n. 2, p. 391-410, 2016.

[153] DOAT, Olivier et al. Materials and modelling for organic photovoltaic devices. **Polymer International**, v. 71, n. 1, p. 6-25, 2022.

[154] COHEN, Aron J.; MORI-SÁNCHEZ, Paula; YANG, Weitao. Challenges for density functional theory. **Chemical reviews**, v. 112, n. 1, p. 289-320, 2012.

[155] BURSCH, Markus et al. Best-Practice DFT Protocols for Basic Molecular Computational Chemistry. **Angewandte Chemie International Edition**, v. 61, n. 42, p. e202205735, 2022.

[156] MARDIROSSIAN, Narbe; HEAD-GORDON, Martin. Thirty years of density functional theory in computational chemistry: an overview and extensive assessment of 200 density functionals. **Molecular Physics**, v. 115, n. 19, p. 2315-2372, 2017.

[157] FRISCH, M. J. E. A. et al. Gaussian 09, revision D. 01. 2009.

[158] LU, Qiuchen et al. Modification of NFA-conjugated Bridges with symmetric structures for High-efficiency Non-fullerene PSCs. **Polymers**, v. 11, n. 6, p. 958, 2019.

[159] YUAN, Jun et al. Single-junction organic solar cell with over 15% efficiency using fused-ring acceptor with electron-deficient core. **Joule**, v. 3, n. 4, p. 1140-1151, 2019.

[160] LV, Ruizhi et al. A terminally tetrafluorinated nonfullerene acceptor for well-performing alloy ternary solar cells. **Advanced Functional Materials**, v. 29, n. 12, p. 1805872, 2019.

[161] PAL, Amrita et al. Comparative density functional theory–density functional tight binding study of fullerene derivatives: effects due to fullerene size, addends, and crystallinity on band structure, charge transport and optical properties. **Physical Chemistry Chemical Physics**, v. 19, n. 41, p. 28330-28343, 2017.

[162] PAN, Ming-Ao et al. 16.7%-efficiency ternary blended organic photovoltaic cells with PCBM as the acceptor additive to increase the open-circuit voltage and phase purity. **Journal of Materials Chemistry A**, v. 7, n. 36, p. 20713-20722, 2019.

[163] KÖRZDÖRFER, Thomas; BREDAS, Jean-Luc. Organic electronic materials: recent advances in the DFT description of the ground and excited states using tuned range-separated hybrid functionals. **Accounts of chemical research**, v. 47, n. 11, p. 3284-3291, 2014.

[164] KRONIK, Leeor et al. Excitation gaps of finite-sized systems from optimally tuned range-separated hybrid functionals. **Journal of Chemical Theory and Computation**, v. 8, n. 5, p. 1515-1531, 2012.

[165] SILVA, Edilene A. et al. Understanding the langmuir and Langmuir-Schaefer film conformation of low-bandgap polymers and their bulk heterojunctions with PCBM. **Nanotechnology**, v. 31, n. 31, p. 315712, 2020.

[166] RONCASELLI, Lucas K. M. et al. Influence of solvents on the morphology of Langmuir and Langmuir–Schaefer films of PCBM and PCBM-based oligomers and polymers. **Physical Chemistry Chemical Physics**, 2022.

[167] LIDE, David R. (Ed.). **CRC handbook of chemistry and physics**. CRC press, 2004.

[168] LEONAT, Lucia; SBARCEA, Gabriela; BRANZOI, Ioan V. Cyclic voltammetry for energy levels estimation of organic materials. **UPB Sci Bull Ser B**, v. 75, n. 3, p. 111-118, 2013.

[169] SWORAKOWSKI, Juliusz. How accurate are energies of HOMO and LUMO levels in small-molecule organic semiconductors determined from cyclic voltammetry or optical spectroscopy?. **Synthetic Metals**, v. 235, p. 125-130, 2018.

[170] MICARONI, L.; NART, F.; HÜMMELGEN, I. Considerations about the electrochemical estimation of the ionization potential of conducting polymers. **Journal of Solid State Electrochemistry**, v. 7, n. 1, p. 55-59, 2002.

[171] Available in: <https://www.edaq.com/wiki/Reference_Electrode_Potentials>. Access in: February 2022.

[172] BARAN, Derya et al. Processable multipurpose conjugated polymer for electrochromic and photovoltaic applications. **Chemistry of Materials**, v. 22, n. 9, p. 2978-2987, 2010.

[173] BRAUNGER, Maria L. et al. Electrical and electrochemical measurements in nanostructured films of polythiophene derivatives. **Electrochimica Acta**, v. 165, p. 1-6, 2015.

[174] SENANAYAK, Satyaprasad P. et al. Room-temperature bandlike transport and Hall effect in a high-mobility ambipolar polymer. **Physical Review B**, v. 91, n. 11, p. 115302, 2015.

[175] IZAWA, Seiichiro; HASHIMOTO, Kazuhito; TAJIMA, Keisuke. Synthesis, characterization, and photovoltaic properties of diketopyrrolopyrrole-oligothiophene/fullerene dyads. **Synthetic Metals**, v. 162, n. 24, p. 2201-2205, 2012.

[176] RAMANITRA, Hasina H. et al. Increased thermal stabilization of polymer photovoltaic cells with oligomeric PCBM. **Journal of Materials Chemistry C**, v. 4, n. 34, p. 8121-8129, 2016.

[177] BENSASSON, Rene V. et al. C60 in model biological systems. A visible-UV absorption study of solvent-dependent parameters and solute aggregation. **The Journal of Physical Chemistry**, v. 98, n. 13, p. 3492-3500, 1994.

[178] STEPHEN, Meera et al. Sterically controlled azomethine ylide cycloaddition polymerization of phenyl-C 61-butyric acid methyl ester. **Chemical Communications**, v. 52, n. 36, p. 6107-6110, 2016.

[179] COOK, Steffan; KATOH, Ruyzi; FURUBE, Akihiro. Ultrafast studies of charge generation in PCBM: P3HT blend films following excitation of the fullerene PCBM. **The Journal of Physical Chemistry C**, v. 113, n. 6, p. 2547-2552, 2009.

[180] BRÉDAS, Jean-Luc et al. Organic semiconductors: A theoretical characterization of the basic parameters governing charge transport. **Proceedings of the National Academy of Sciences**, v. 99, n. 9, p. 5804-5809, 2002.

[181] BRONSTEIN, Hugo et al. The role of chemical design in the performance of organic semiconductors. **Nature Reviews Chemistry**, v. 4, n. 2, p. 66-77, 2020.

[182] YE, Linglong et al. Unraveling the influence of non-fullerene acceptor molecular packing on photovoltaic performance of organic solar cells. **Nature communications**, v. 11, n. 1, p. 1-9, 2020.

[183] PASINI, Mariacecilia et al. Solid-state Effects in the Cyclovoltammetric HOMO-LUMO Determination: The case of Dinitrophenyl-hydrazone α,ω-substituted Oligothiophenes. **Electrochimica Acta**, v. 193, p. 261-267, 2016.